

Development and Application of the Spherical
Harmonic Veto Definer for Gravitational-Wave
Transient Search

DOCTORAL THESIS

By

Elena Massera



Department of Physics and Astronomy

*A thesis submitted in fulfillment of the requirements
for the degree of Doctor of Philosophy
in the*

LIGO Research Group

April 2020

“In the middle of every difficulty lies opportunity”

“Nel mezzo delle difficoltà nascono le opportunità”

A. Einstein

Abstract

The rapid analysis of gravitational-wave data is not trivial for many reasons, such as the non-Gaussian non-stationary nature of LIGO detector noise and the lack of exhaustive waveform models. Non-Gaussian non-stationary noise and instrumental artifacts are known as 'glitches'.

X-Pipeline Spherical Radiometer (X-SphRad) is a software package designed for performing autonomous searches for un-modelled gravitational-wave bursts. X-SphRad has an approach based on spherical radiometry, that transforms time-series data streams into the spherical harmonic domain. Spherical harmonic coefficients show potential in discriminating glitches from signals.

For my Ph.D. thesis, I evaluated and implemented a tool for glitch rejection called Spherical Harmonic Veto Definer (SHaVeD). SHaVeD is a Matlab script that loads spherical harmonic coefficients computed by X-SphRad, and performs statistics that computes a threshold to apply. The threshold is used to identify every glitch's GPS time and create a cut of one second around it. SHaVeD saves this information in a two-column file where the first column is the GPS starting time of the cut and the second is the final time. X-SphRad can include SHaVeD as a data quality to veto glitches.

The tool is tested with X-SphRad and the coherent WaveBurst (cWB) pipeline over the O2 observation run. Results have shown how the inclusion of SHaVeD in the analysis could allow a lowering of some thresholds used in this type of research. Tests show how SHaVeD has reduced the amplitude of the loudest false event by a factor of 3, meaning that it rejected false events in a volume 9 times greater than usual.

Contents

List of Figures	iv
Nomenclature	xviii
1 Gravitational waves: From the theory to the detection	1
1.1 The Theory of General Relativity	2
1.1.1 Linearized Einstein's equations	5
1.1.2 Properties of plane gravitational waves	6
1.1.3 Interaction of Gravitational waves with matter	7
1.1.4 Emission of gravitational waves	8
1.2 Sources of gravitational waves	9
1.2.1 Sources of periodic signals	11
1.2.2 Transient signals sources	14
1.2.3 Stochastic background	21
1.3 Gravitational waves detection	21
1.3.1 Laser interferometers	21
1.3.2 Interferometer operating principle: advanced LIGO	24
1.3.3 Noise sources	26
1.3.4 Detections list	28
2 Long-duration burst signals searches	31
2.1 Introduction and Motivation of Research	31
2.2 Waveform models	33
2.3 The X-Pipeline Spherical Radiometer	36
2.3.1 Formalism in X-Pipeline	37

2.3.2	Overview of the spherical radiometer algorithm	39
2.3.3	Pipeline schema	40
2.3.4	Data management and optimisation	40
2.3.5	Time-Frequency maps and Clustering	41
2.3.6	Background and Simulated signals	42
2.3.7	Vetoos and Tuning	43
2.4	Coherent Wave Burst (cWB) pipeline	45
2.4.1	Data conditioning	46
2.4.2	Time-Frequency clusters	46
2.4.3	Coherent triggers selection	47
2.5	X-SphRad and cWB: a comparison on the O2 data	50
2.5.1	Data Quality	50
2.5.2	Analysis Parameters	50
2.5.3	Results	51
3	SHaVeD: Spherical Harmonic Veto Definer	58
3.1	Description of the method	58
3.2	Application and analysis of O2 data using cWB	65
3.2.1	Threshold choice	66
3.2.2	SHaVeD in pre-production	68
3.2.3	SHaVeD in post-production	71
3.2.4	Tests of SHaVeD using ad-hoc waveform injections	80
3.3	GW170817 event	82
3.3.1	An issue: a glitch in the LIGO-Livingston data	85
3.3.2	A challenge: applying SHaVeD in the pre-whitening stage	85
3.4	Raw Analysis of O3 data	92
3.5	Potential and limits: a SWOT analysis	97
4	Testing phenomenological waveforms with X-SphRad	99
4.1	Scenario	99
4.2	PT12 waveforms: a semi-analytical model	100
4.3	PT12 analysis with X-SPhRad	103

CONTENTS

4.3.1	Analysis Parameters	103
4.3.2	Results and considerations	109
5	Conclusion	117
A	<i>Spherical harmonic coefficients order</i>	120
B	<i>cWB and X-SphRad detection efficiency curves</i>	121
C	<i>Matlab SHaVeD script</i>	129
D	<i>PT12 waveforms detection efficiency curves</i>	131
	Bibliography	135
	Acknowledgements	148

List of Figures

1.1	Schematic representation of the distortion effect due to the polarization states of a gravitational wave, propagating in the z direction [103].	8
1.2	PSR 1913+16 system. Energy losses due to gravitational radiation, predicted by GR, is represented by the parabolic curve [103].	13
1.3	Gravitational wave signal emitted from a coalescing binary system during the inspiral phase. System of two black holes of mass M1 and M2 the coalescence at t=0.1 seconds. (Image:A.Stuver/LIGO)	15
1.4	GW150914 event observed by the LIGO Hanford (H1, left column panels) and Livingston (L1, right column panels) detectors. GW150914 arrived first at L1 and 6.9 ms later at H1; for a comparison, the H1 data are also shown, shifted in time and inverted to include the detectors relative orientations. Red and blue lines, in the bottom rows, show a numerical relativity waveform for a system with parameters consistent with those recovered from GW150914 [84].	16
1.5	Example of Type-I and Type-II supernovae light curves. Type-II curves have a characteristic bump in the declining phase [102].	17
1.6	Canonical light curve of the X-ray afterglow [101].	20

1.7	World network of GWs detectors [96]. 4 km-long arms interferometers are located in Hanford (USA) and in Livingston (USA) and they are active nowadays. Alongside these american detectors, you find GEO600, VIRGO and KAGRA, all active. INDIGO is under construction. Once it will be operational, a dramatic improvement in GW sources localization is expected.	23
1.8	A schematic showing Advanced LIGO's interferometer [98]. The detection is based on the phase difference between the light returning from each arm. Fabry- Perot arm cavities are used for the interferometer arms to increase the time of exposure of the laser light to the gravitational wave, and there is a power recycling mirror between the laser and beam-splitter to increase effective laser power.	24
1.9	Sensitivity of the aLIGO detectors [16]. The daily operation of the interferometer is strongly influenced by different sources of noise that affect the detection of the gravitational signal. Schematically, you can group the noises into two categories: real movements of test masses and instrumental limits. The first group includes all those disturbances that cause the displacement of the test masses, the mirrors, and of all the optical elements crossed by the laser beam (seismic noise, thermal noise, etc.). On the other hand, all those disturbances belong to the second group which, while not producing any movement of the optical components, give rise to a spurious fluctuation of the phase between the interfering beams, thus simulating the passage of a gravitational signal (laser frequency noise, fluctuations of the refractive index of the residual gas inside the vacuum tubes, etc.).	27
1.10	First detections of gravitational-waves made by the LIGO-VIRGO detectors. Detections information taken from [100]. . .	28

2.1	Gravitational-wave strain versus frequency for some waveform models for burst signals. From [79].	34
2.2	Graphic illustration of Ad-hoc waveforms to show how their signal reconstruction looks like on the time-frequency plane. From [104].	36
2.3	X-SphRad flowchart.	40
2.4	Detection efficiency curve of LINE B waveform test. Fraction of injections recovered with significance greater than loudest event in (dummy) on-source. Black dots are sampled values, red and yellow dots are respectively the 90 % and 50 % efficiency obtained from interpolation. Green dots mark sampled valued with $0 < \text{efficiency} < 5$ %. The blue curve shows the efficiency when DQ flags are not applied to injections. Image and caption are taken from our webpage to provide results from the analysis made using X-SphRad.	44
2.5	Main steps of cWB pipeline.	46
2.6	The black line is the Hanford detector's power spectra of noise. The red line is the same spectra of noise after the application of a filter [48].	47
2.7	Example of different time-frequency resolution signal reconstructions with cWB using a simulated signal [48].	48
2.8	Example of cWB TF cluster : the core (black pixels) and the halo (grey pixels) [48].	49
2.9	LIGO observing time for the O2 scientific run. The yellow box highlights the coincident time analysed in this work [53]. . . .	51
2.10	Duration and frequency range for each analysed waveform. Waveforms are selected among astrophysical and ad-hoc families.	52

2.11	Detection efficiency curve of an ADI A waveform test. Fraction of injections recovered with significance greater than loudest event in (dummy) on-source. Black dots are sampled values, red and yellow dots are respectively the 90 % and 50 % efficiency obtained from interpolation. Green dots mark sampled valued with $0 < \text{efficiency} < 5$ %. The blue curve shows the efficiency when DQ flags are not applied to injections. Image and caption are taken from our webpage to provide results from the analysis made using X-SphRad.	53
2.12	Example of a detection efficiency plot of an ADI A waveform injected into cWB. The caption reports the value of the hrss value for a detection probability of the 50 %. $3.71e^{-22}$ value displayed in the capture corresponds to the hrss value.	54
2.13	Hrss values, corresponding to the 50 % detection probability, produced by X-SphRad and cWB for eight waveforms. The smaller hrss value the better the detection efficiency will be.	55
2.14	Hrss values, corresponding to the 90 % detection probability, produced by X-SphRad and cWB for eight injected waveforms. The smaller hrss value the better the detection efficiency will be.	55
2.15	Effective distance reached by X-SphRad and cWB for each analysed waveform, with the 50 % detection probability.	56
3.1	A dual-representation of the same data-frame. Frequency-time (TF) map top: A glitch can be clearly seen at about 700s. Spherical-harmonic-time (TSH) bottom: A glitch can be seen at about 700s just in the C_{00} component (light yellow line).	60
3.2	A dual-representation of the same data-frame. Frequency-time (TF) map top: A glitch can be seen at about 210s alongside an injection at about 380s. Spherical-harmonic-time (TSH) bottom: A glitch can be seen at about 210s just in the C_{00} component, while the injection can be seen spread on all coefficients.	61

3.3	Top: A time-frequency map of whitened data; to the upper left we see a short-duration white noise burst (WNB) signal, to the lower middle a glitch. Bottom Left: Time-harmonic map for a segment containing a glitch and an injection. Only the injection is visible (the vertical line at 10s). Bottom Right: Skymap of the coefficients corresponding to the time bin containing the injection, see Figure 3 at 10s.[32]	62
3.4	Example of the ratios between Clm and $C00$ of a data frame with a threshold fixed at 1 %. The dashed red line is the threshold obtained by using the standard deviation distribution of ratios values.	63
3.5	Distribution and Gaussian fit of ratios values.	63
3.6	Blue boxes highlight where glitches in the TF domain (top plot) match minimum peaks of the ratio function (bottom plot).	64
3.7	File of rejected time segments generated by SHaVeD. The two columns denote the GPS seconds between the start and end of the segment to be excluded from the analysis.	65
3.8	Cumulative curve of rate vs ρ of three analysis made with threshold on the $Clm/C00$ ratio of 5 %, 2.5 %, and 1 %. . . .	67
3.9	Cumulative curve of rate vs ρ obtained using the Gating and SHaVeD. Both curves have the same trend and for various ρ values they are comparable within the error bars.	69
3.10	Cumulative curve of rate vs ρ obtained using the Gating alone and SHaVeD added to the Gating. SHaVeD can improve the analysis up to ρ of about 5.5, while it has a trend comparable to the Gating up to ρ of about 6.8.	70
3.11	Cumulative curve of rate vs ρ with (red dots) and without (black dots) the application of SHaVeD. The comparison shows how SHaVeD improves the pipeline analysis in terms of glitches identification and rejection. This test analysed 130 years of background. Here no cWB long-duration cuts have been applied.	72

3.12 The cWB loudest event list:ID is the identification number. "cat3" column shows that SHaVeD removes three events among the top ten. This test analysed 130 years of background. Here no cWB long-duration cuts have been applied. 73

3.13 Cumulative curve of rate vs ρ with (red dots) and without (black dots) the application of SHaVeD. The comparison shows no substantial difference using SHaVeD (red dots) in addition to the cWB Long-duration veto (black dots). This test analysed 130 years of background. Here both cWB Gating and cWB long-duration cuts have been applied. 74

3.14 The cWB loudest event list:ID is the identification number. "cat3" column shows that SHaVeD removes one event among the top ten, so no significant effect beyond what the cWB cuts have already achieved. This test analysed 130 years of background. Here both cWB Gating and cWB long-duration cuts have been applied. 75

3.15 Cumulative curve of rate vs ρ with (red dots) and without (black dots) the application of SHaVeD. Here no cWB Gating and no cWB long-duration cuts have been applied in the pre-production stage. The comparison shows how SHaVeD significantly improves the pipeline performance. This test analysed 485 years of background. Here no cWB Gating and no cWB long-duration cuts have been applied. 76

3.16 The cWB loudest event list:ID is the identification number. "cat3" column shows that SHaVeD removes seven events among the top ten. This test analysed 485 years of background. Here no cWB Gating and no cWB long-duration cuts have been applied. 77

3.17 Cumulative curve of rate vs ρ with (red dots) and without (black dots) the application of SHaVeD. Here no cWB Gating is applied in the pre-production stage. The comparison shows how SHaVeD significantly improves the pipeline performance. This test analysed 130 years of background. Here no cWB Gating and no cWB long-duration cuts have been applied. 78

3.18 The cWB loudest event list:ID is the identification number. "cat3" refers to SHaVeD and it shows that SHaVeD removes four events among the top ten. This test analysed 130 years of background. Here no cWB Gating and no cWB long-duration cuts have been applied. 79

3.19 Detection efficiency of cWB as a function of the injection amplitude of the ADI A signal. The value of the signal amplitude where the efficiency is 50 % is $3.7e^{-22}$. The threshold is set such that the false alarm rate is 1 event every 10 years, as determined by parallel analysis of timeshifted data. 80

3.20 Detection efficiency of cWB as a function of the injection amplitude of the ADI A signal, with SHaVeD applied in the pre-production stage. The value of the signal amplitude where the efficiency is 50 % is $3.72e^{-22}$. The threshold is set such that the false alarm rate is 1 event every 10 years, as determined by parallel analysis of timeshifted data. 81

3.21 Sky location reconstructed for GW170817 by a rapid localization algorithm from a Hanford-Livingston ($190deg^2$, light blue contours) and Hanford-Livingston-Virgo ($31deg^2$, dark blue contours) analysis. A higher latency Hanford-Livingston-Virgo analysis improved the localization ($28deg^2$, green contours)(90 % probability)[58]. 83

3.22 Time-frequency representations of GW170817 event, before the merging time at GPS 1187008882.4, observed by the LIGO-Hanford (top), LIGO-Livingston (middle), and Virgo (bottom) detectors [58]. 84

3.23	Top panel: A time-frequency representation of the raw LIGO-Livingston data used in the initial identification of GW170817 [76]. The coalescence time reported by the search is at time 0.4 s in this figure and the glitch occurs 1.1 s before this time. Bottom panel: The raw LIGO-Livingston strain data (orange curve) showing the glitch in the time domain [58].	86
3.24	Time-frequency map of the whitened zoom data around the glitch, provided by LIGO-Livingston detector for the data segment from 1187008687.000 to 1187009927.000 GPS time [43]. .	87
3.25	Likelihood time-frequency map of the whitened zoom data around the glitch, provided by the LIGO-Livingston detector for the data segment from 1187008687.000 to 1187009927.000 GPS time [43]. Pixels due to GW are not visible due to the glitch.	88
3.26	Example of the inverse Tukey Window function used to apply SHaVeD in the pre-production and pre-whitening analysis with cWB. Yellow circles highlight the GPS time when glitch and merger occurred respectively.	89
3.27	Example of how the inverse Tukey Window function works with SHaVeD to cut off the glitch: the black line is the original signal; the red line is the signal after the windowing, which leads glitch contribution to zero. Orange dashed boxes indicates where the glitch and the GW signal occurred respectively.	90
3.28	Time-frequency map of the whitened data around the glitch, provided by the LIGO-Livingston detector for the data segment from 1187008780.000 to 1187010020.000 GPS time [43]. .	90
3.29	Likelihood time-frequency map of the whitened data around the glitch, provided by the LIGO-Livingston detector for the data segment from 1187008780.000 to 1187010020.000 GPS time [43].	91
3.30	LIGO observing time for the O3 scientific run. Black dashed lines highlight the coincident time analysed in this work [63]. .	93

3.31	Multi-interferometer observing segments for the O3 scientific run. The red box highlights the coincident time analysed in this work [63].	93
3.32	Cumulative curve of rate vs ρ with (red dots) and without (black dots) the application of SHaVeD. The comparison shows how SHaVeD significantly improves the pipeline analysis. This test analysed 130 years of background. Here no cWB Gating and no cWB long-duration cuts have been applied.	95
3.33	Loudest event list: "cat3" column shows that SHaVeD removes almost all events among the top twenty. This test analysed 130 years of background. Here no cWB Gating and no cWB long-duration cuts have been applied.	96
4.1	A representation of the PT-A and the PT-B waveforms in the time-frequency domain.	105
4.2	A representation of the PT-C and the PT-D waveforms in the time-frequency domain.	106
4.3	A representation of the PT-E and the PT-F waveforms in the time-frequency domain.	107
4.4	Duration and frequency range for each PT12 waveform.	108
4.5	Detection efficiency curves of the PT12 waveforms given by the X-SphRad analysis. Fraction of injections recovered with significance greater than loudest event in (dummy) on-source. Black dots are sampled values, red and yellow dot is respectively the 90 % and 50 % efficiency obtained from interpolation. Green dots mark sampled valued with $0 < \text{efficiency} < 5$ %. The blue curve shows the efficiency when DQ flags are not applied to injections. We obtain the 90 % upper limit from fit. Image and caption are taken from our webpage provides results from the analysis made using X-SphRad.	109

4.6 Detection efficiency curves of the PT12 waveforms given by the X-SphRad analysis. Fraction of injections recovered with significance greater than loudest event in (dummy) on-source. Black dots are sampled values, red and yellow dot is respectively the 90 % and 50 % efficiency obtained from interpolation. Green dots mark sampled valued with $0 < \text{efficiency} < 5$ %. The blue curve shows the efficiency when DQ flags are not applied to injections. We obtain the 90 % upper limit from fit. Image and caption are taken from our webpage provides results from the analysis made using X-SphRad. 110

4.7 Detection efficiency curves of the PT12 waveforms given by the X-SphRad analysis. Fraction of injections recovered with significance greater than loudest event in (dummy) on-source. Black dots are sampled values, red and yellow dot is respectively the 90 % and 50 % efficiency obtained from interpolation. Green dots mark sampled valued with $0 < \text{efficiency} < 5$ %. The blue curve shows the efficiency when DQ flags are not applied to injections. We obtain the 90 % upper limit from fit. Image and caption are taken from our webpage provides results from the analysis made using X-SphRad. 111

4.8 Detection efficiency curves of the Line B waveform given by the X-SphRad analysis. Fraction of injections recovered with significance greater than loudest event in (dummy) on-source. Black dots are sampled values, red and yellow dot is respectively the 90 % and 50 % efficiency obtained from interpolation. Green dots mark sampled valued with $0 < \text{efficiency} < 5$ %. The blue curve shows the efficiency when DQ flags are not applied to injections. We obtain the 90 % upper limit from fit. Image and caption are taken from our webpage provides results from the analysis made using X-SphRad. 112

4.9	Detection efficiency curves of the G19LS220 waveform given by X-SphRad analysis. Fraction of injections recovered with significance greater than loudest event in (dummy) on-source. Black dots are sampled values, red and yellow dot is respectively the 90 % and 50 % efficiency obtained from interpolation. Green dots mark sampled valued with $0 < \text{efficiency} < 5$ %. The blue curve shows the efficiency when DQ flags are not applied to injections. We obtain the 90 % upper limit from fit. Image and caption are taken from our webpage provides results from the analysis made using X-SphRad.	114
4.10	Effective distance reached by the X-SphRad for PT12 waveforms, with the 50 % of detection probability.	115
4.11	The noise amplitude spectra curves for both Hanford and Livingston are shown alongside with gravitational-wave strain versus frequency for PT12 waveforms detected with 50 % efficiency and a false alarm rate of 1 event in 10 years.	116
A.1	Spherical harmonic coefficients order, expressed as (l, m) pairs, read left to right and top to bottom[32].	120
B.1	Example of a detection efficiency plot of a waveform injected into cWB. The caption reports the waveform type, the value of the hrss value for a detection probability of the 10, 50 and 90 %.	122
B.2	Example of a detection efficiency plot of a waveform injected into cWB. The caption reports the waveform type, the value of the hrss value for a detection probability of the 10, 50 and 90 %.	123
B.3	Example of a detection efficiency plot of a waveform injected into cWB. The caption reports the waveform type, the value of the hrss value for a detection probability of the 10, 50 and 90 %.	124

B.4 Example of a detection efficiency plot of a waveform injected into cWB. The caption reports the waveform type, the value of the hrss value for a detection probability of the 10, 50 and 90 %. 125

B.5 Example of a detection efficiency plot of a waveform injected into cWB. The caption reports the waveform type, the value of the hrss value for a detection probability of the 10, 50 and 90 %. 126

B.6 Example of a detection efficiency plot of a waveform injected into X-SphRad. Fraction of injections recovered with significance greater than loudest event in (dummy) on-source. Black dots are sampled values, red and yellow dots are respectively the 90 % and 50 % efficiency obtained from interpolation. Green dots mark sampled valued with $0 < \text{efficiency} < 5$ %. The blue curve shows the efficiency when DQ flags are not applied to injections. Image and caption are taken from our webpage to provide results from the analysis made using X-SphRad. . . . 127

B.7 Example of a detection efficiency plot of a waveform injected into X-SphRad. Fraction of injections recovered with significance greater than loudest event in (dummy) on-source. Black dots are sampled values, red and yellow dots are respectively the 90 % and 50 % efficiency obtained from interpolation. Green dots mark sampled valued with $0 < \text{efficiency} < 5$ %. The blue curve shows the efficiency when DQ flags are not applied to injections. Image and caption are taken from our webpage to provide results from the analysis made using X-SphRad. . . . 128

D.1 Detection efficiency curves of ad-hoc waveforms included in the PT12 waveforms X-SphRad analysis. Fraction of injections recovered with significance greater than loudest event in (dummy) on-source. Black dots are sampled values, red and yellow dots are respectively the 90 % and 50 % efficiency obtained from interpolation. Green dots mark sampled valued with $0 < \text{efficiency} < 5$ %. The blue curve shows the efficiency when DQ flags are not applied to injections. Image and caption are taken from our webpage to provide results from the analysis made using X-SphRad. 131

D.2 Detection efficiency curves of ad-hoc waveforms included in the PT12 waveforms X-SphRad analysis. Fraction of injections recovered with significance greater than loudest event in (dummy) on-source. Black dots are sampled values, red and yellow dots are respectively the 90 % and 50 % efficiency obtained from interpolation. Green dots mark sampled valued with $0 < \text{efficiency} < 5$ %. The blue curve shows the efficiency when DQ flags are not applied to injections. Image and caption are taken from our webpage to provide results from the analysis made using X-SphRad. 132

D.3 Detection efficiency curves of ad-hoc waveforms included in the PT12 waveforms X-SphRad analysis. Fraction of injections recovered with significance greater than loudest event in (dummy) on-source. Black dots are sampled values, red and yellow dots are respectively the 90 % and 50 % efficiency obtained from interpolation. Green dots mark sampled valued with $0 < \text{efficiency} < 5$ %. The blue curve shows the efficiency when DQ flags are not applied to injections. Image and caption are taken from our webpage to provide results from the analysis made using X-SphRad. 133

D.4 Detection efficiency curves of ad-hoc waveforms included in the PT12 waveforms X-SphRad analysis. Fraction of injections recovered with significance greater than loudest event in (dummy) on-source. Black dots are sampled values, red and yellow dots are respectively the 90 % and 50 % efficiency obtained from interpolation. Green dots mark sampled valued with $0 < \text{efficiency} < 5$ %. The blue curve shows the efficiency when DQ flags are not applied to injections. Image and caption are taken from our webpage to provide results from the analysis made using X-SphRad. 133

D.5 Detection efficiency curves of ad-hoc waveforms included in the PT12 waveforms X-SphRad analysis. Fraction of injections recovered with significance greater than loudest event in (dummy) on-source. Black dots are sampled values, red and yellow dots are respectively the 90 % and 50 % efficiency obtained from interpolation. Green dots mark sampled valued with $0 < \text{efficiency} < 5$ %. The blue curve shows the efficiency when DQ flags are not applied to injections. Image and caption are taken from our webpage to provide results from the analysis made using X-SphRad. 134

D.6 Detection efficiency curves of ad-hoc waveforms included in the PT12 waveforms X-SphRad analysis. Fraction of injections recovered with significance greater than loudest event in (dummy) on-source. Black dots are sampled values, red and yellow dots are respectively the 90 % and 50 % efficiency obtained from interpolation. Green dots mark sampled valued with $0 < \text{efficiency} < 5$ %. The blue curve shows the efficiency when DQ flags are not applied to injections. Image and caption are taken from our webpage to provide results from the analysis made using X-SphRad. 134

Nomenclature

ADI	Accretion Disk Instabilities
BBH	Binary Black Holes
BNS	Binary Neutron Stars
cWB	coherent WaveBursts
G	Universal gravitational constant
GR	General Relativity
GRB	Gamma-Ray Burst
GWs	Gravitational Waves
hrss	gravitational amplitude root-sum-square
LIGO	Laser Interferometer Gravitational Observer
PT	Piro and Thrane
SH	Spherical Harmonic
SHaVeD	Spherical Harmonic Veto Definer
TF	Time Frequency
TT	Transverse-Traceless
X-SphRad	X-Pipeline Spherical Radiometer

Chapter 1

Gravitational waves: From the theory to the detection

In 1916 Albert Einstein published “Die Grundlage der allgemeinen Relativitätstheorie” (Foundations of the General Relativity)[1], where he laid out the theory of the General Relativity. This theory asserts that massive objects deform the space-time. Therefore, changes to the metric are caused by changes in the distribution of matter and energy. Gravitational waves (GWs) have their origin from these perturbations. Gravity assumes a completely different role in General Relativity (GR). Gravity is not a force, as it is in Newton’s Universal law of gravitation, it is a manifestation of space-time geometry. GWs, predicted by GR, are quite different from electromagnetic waves. Accelerated charges emit electromagnetic waves, while accelerated mass distributions having a time-varying mass quadrupole moment generate gravitational waves. Furthermore, unlike electromagnetic waves, GWs are weak so they had until 2015 evaded detection entirely.

The first detections were of waves from binary systems of black holes - some of the more compact and dense objects in the Universe. By contrast, electromagnetic waves emitted by accelerating charges are visible to the naked eye. Yet the signals in GWs from black holes carry information from the hearts of these fascinating engines. Detection of gravitational waves allows the verification of GR and it has a wide impact on the astrophysics re-

search because it gives the opportunity to investigate the nature of compact objects such as neutron stars and black holes. In this chapter we introduce the basic concepts of the theory, showing how to obtain linearized solutions of Einstein's equations in the weak-field approximation. We present an overview of the possible astronomical sources of gravitational waves. We introduce the basic elements of interferometric GW detectors and their operating principles and describe the most significant noise sources. Finally, we discuss the detections made so far.

1.1 The Theory of General Relativity

Gravity in GR is a geometric property of space-time. GR is based on the Principle of Equivalence [2]. This principle can be expressed as follow: Every physics law must be invariant under general transformations of coordinates. The strong Principle of Equivalence derives from the general invariance and it states that *“In an arbitrary gravitational field, at any given spacetime point, we can choose a locally inertial reference frame such that, in a sufficiently small region surrounding that point, all physical laws take the same form they would take in absence of gravity, namely the form prescribed by Special Relativity”*[2]. Note that trajectories of a free fall bodies tend to bend, following a geometry depending on the distribution of matter and energy. From here, mathematical steps follow the treatment carried out in [2] and [4]. In Special Relativity the distance between two neighbouring spacetime points is

$$ds^2 = -c^2 dt^2 + dx^2 + dy^2 + dz^2 = \eta_{\mu\nu} d\xi^\mu d\xi^\nu \quad (1.1)$$

where $\eta_{\mu\nu} = \text{diag}(-1, 1, 1, 1)$ is the metric signature of the flat Minkowski spacetime, and ξ^μ are the locally Euclidean coordinates. The equations of motion of a free falling particle are

$$\frac{d^2 \xi^\alpha}{d\tau^2} = 0 \quad (1.2)$$

where τ is the particle proper time defined by

$$d\tau^2 = -\eta_{\alpha\beta}d\xi^\alpha d\xi^\beta. \quad (1.3)$$

We now change to a frame where the coordinates are labelled $x^\alpha = x^\alpha(\xi^\alpha)$, so we assign a transformation law which allows us to express the new coordinates as functions of the old ones. In the new frame the distance is

$$ds^2 = \eta_{\alpha\beta} \frac{\partial \xi^\alpha}{\partial x^\mu} dx^\mu \frac{\partial \xi^\beta}{\partial x^\nu} dx^\nu = g_{\mu\nu} dx^\mu dx^\nu, \quad (1.4)$$

where we have defined the metric tensor $g_{\mu\nu}$ as

$$g_{\mu\nu} = \frac{\partial \xi^\alpha}{\partial x^\mu} \frac{\partial \xi^\beta}{\partial x^\nu} \eta_{\alpha\beta}. \quad (1.5)$$

In this new reference frame, the equation of motion of the particle (1.2) becomes:

$$\frac{d^2 x^\alpha}{d\tau^2} + \left[\frac{\partial x^\alpha}{\partial \xi^\lambda} \frac{\partial^2 \xi^\lambda}{\partial x^\mu \partial x^\nu} \right] \left[\frac{dx^\mu}{d\tau} \frac{dx^\nu}{d\tau} \right] = 0. \quad (1.6)$$

If we now define the following quantities, called affine connections, or Christoffel's symbols

$$\Gamma_{\mu\nu}^\alpha = \frac{\partial x^\alpha}{\partial \xi^\lambda} \frac{\partial^2 \xi^\lambda}{\partial x^\mu \partial x^\nu}, \quad (1.7)$$

the equation of motion 1.6 becomes:

$$\frac{d^2 x^\alpha}{d\tau^2} + \Gamma_{\mu\nu}^\alpha \left[\frac{dx^\mu}{d\tau} \frac{dx^\nu}{d\tau} \right] = 0. \quad (1.8)$$

Equation 1.8 is the *geodesic equation*. The additional term $\Gamma_{\mu\nu}^\alpha \left[\frac{dx^\mu}{d\tau} \frac{dx^\nu}{d\tau} \right]$ expresses the gravitational force per unit mass that acts on the particle. Christoffel's symbols can be calculated from the metric coefficients and their derivatives as follows:

$$\Gamma_{\lambda\mu}^\sigma = \frac{1}{2} g^{\nu\sigma} \left(\frac{\partial g_{\mu\nu}}{\partial x^\lambda} + \frac{\partial g_{\lambda\nu}}{\partial x^\mu} - \frac{\partial g_{\lambda\mu}}{\partial x^\nu} \right). \quad (1.9)$$

We here introduce the term $R_{\nu\alpha\beta}^{\mu}$, known as the Riemann tensor of curvature. It can be written in terms of the connection coefficients and their derivatives as [4]:

$$R_{\nu\alpha\beta}^{\mu} = -\Gamma_{\nu\alpha,\beta}^{\mu} + \Gamma_{\nu\beta,\alpha}^{\mu} + \Gamma_{\sigma\alpha}^{\mu}\Gamma_{\nu\beta}^{\sigma} - \Gamma_{\sigma\beta}^{\mu}\Gamma_{\nu\alpha}^{\sigma}. \quad (1.10)$$

The curvature tensor satisfies the following symmetry properties, valid in any reference frame:

$$R_{\alpha\beta\mu\nu} = -R_{\beta\alpha\mu\nu} = -R_{\alpha\beta\nu\mu} = R_{\mu\nu\alpha\beta} \quad (1.11)$$

$$R_{\alpha\beta\mu\nu} + R_{\alpha\nu\beta\mu} + R_{\alpha\mu\nu\beta} = 0. \quad (1.12)$$

By contraction, some other useful quantities can be obtained from the Riemann tensor, such as the Ricci tensor and the scalar curvature, respectively given by:

$$R_{\nu\beta\alpha}^{\beta} = R_{\nu\alpha} \quad (1.13)$$

$$R = R_{\beta}^{\beta}. \quad (1.14)$$

All other contractions of $R_{\nu\alpha\beta}^{\mu}$ are zero, or equal to this one, due to the symmetry properties given in Equations 1.11 and 1.12. To obtain Einstein's field equations, whose solution is the metric tensor $g_{\mu\nu}$, we must define the Stress-Energy tensor $T^{\mu\nu}$ which contains all the information about the distribution of matter, energy, momentum and stress in spacetime, and includes terms due to the presence of other non-gravitational fields. If we consider a system of N non interacting particles, $T^{\mu\nu}$ assumes the form:

$$T^{\mu\nu} = c^2 \sum_{n=1}^N \frac{p_n^{\mu} p_n^{\nu}}{E_n} \delta^3(\vec{\xi} - \vec{\xi}_n(t)), \quad (1.15)$$

where p_n is the energy-momentum four-vector of the n-particle, $\vec{\xi}_n(t)$ its position vector and E_n is the energy of the n-particle. Notice that:

- T^{00} represents the energy density of the system,
- $T^{\mu\nu}$ is a symmetric tensor.

We now introduce the tensor $G_{\mu\nu}$, known as the Einstein tensor [2]:

$$G_{\mu\nu} = \frac{8\pi G}{c^4} T_{\mu\nu}. \quad (1.16)$$

$G_{\mu\nu}$ is then proportional to $T_{\mu\nu}$.

The Einstein's tensor is also constructed from a linear combination of the Ricci tensor 1.13 and the scalar curvature 1.14:

$$G_{\mu\nu} = c_1 R_{\mu\nu} + c_2 g_{\mu\nu} R. \quad (1.17)$$

"Bianchi identities"[4] say that $\frac{c_1}{c_2} = -\frac{1}{2}$ and, if we require that the relativistic field equations reduce to the newtonian equations in the weak field limit it must be $c_1 = 1$. Consequently, $c_2 = \frac{1}{2}$. Equation 1.17 becomes:

$$G_{\mu\nu} = R_{\mu\nu} + \frac{1}{2} g_{\mu\nu} R. \quad (1.18)$$

Therefore the *Einstein's field equations* are:

$$G_{\mu\nu} = \frac{8\pi G}{c^4} T_{\mu\nu}, \quad (1.19)$$

$$G_{\mu\nu} = R_{\mu\nu} + \frac{1}{2} g_{\mu\nu} R. \quad (1.20)$$

1.1.1 Linearized Einstein's equations

Gravitational waves are solutions of the Einstein field Equations (Equations 1.19 and 1.20) in which the components of the metric can be shown to obey the wave equation. It is not always possible to obtain exact solutions of Einstein's equation because they are non-linear. However, a perturbative approach (small perturbation $|h_{\mu\nu}| \ll 1$) can be applied to obtain the metric tensor far from the source. That approach is based on the assumption of a weak gravitational field. In that case, the Einstein equations can be

linearized. We write the metric tensor as a sum of two contributions:

$$g_{\mu\nu} = \eta_{\mu\nu} + h_{\mu\nu}, \quad (1.21)$$

with $|h_{\mu\nu}| \ll 1$.

In the weak-field approximation, very far from the source where $T_{\mu\nu} = 0$, the wave equation is:

$$\square \bar{h}_{\mu\nu} = 0. \quad (1.22)$$

Where $\square = \eta^{\lambda k} \frac{\partial^2}{\partial x^\lambda \partial x^k}$ is the D'Alembert operator and $\bar{h}_{\mu\nu} \equiv h_{\mu\nu} - \frac{1}{2}\eta_{\mu\nu}h$.

The Equation 1.22 is a particular case of the following generalised Equation 1.23

$$\square \bar{h}_{\mu\nu} = -\frac{16\pi G}{c^4} T_{\mu\nu}. \quad (1.23)$$

The simplest solution of Equation 1.22 is a monochromatic plane wave:

$$\bar{h}_{\mu\nu} = \mathbb{R} \{ A_{\mu\nu} e^{ik_\gamma x^\gamma} \} \quad (1.24)$$

where $A_{\mu\nu}$ is the polarization tensor (see Equation 1.26), connected to the wave amplitude. While $k_\gamma x^\gamma = \vec{k} \cdot \vec{r} - \omega t$ where \vec{k} is the wave vector.

1.1.2 Properties of plane gravitational waves

Let us summarize the plane gravitational waves of Equation 1.24:

- the wave propagates at the speed of light in vacuum c ;
- the wave is transverse:

$$A_{\alpha}^{\mu} k_{\mu} = 0 \quad (1.25)$$

i.e. the wave vector and the polarization tensor are orthogonal;

- there are only two polarization states, since the polarization tensor $A_{\mu\nu}$ is symmetric in the *transverse-traceless* (TT) gauge [4]; for a gravita-

tional wave propagating along the z -axis, its polarization vector is:

$$A_{\mu\nu} = \begin{pmatrix} 0 & 0 & 0 & 0 \\ 0 & A_{xx} & A_{xy} & 0 \\ 0 & A_{xy} & -A_{xx} & 0 \\ 0 & 0 & 0 & 0 \end{pmatrix}, \quad (1.26)$$

where $A_{xx} = A_+$ and $A_{xy} = A_\times$ are respectively the amplitude of the *plus* polarization and the *cross* polarization components of the plane gravitational wave.

1.1.3 Interaction of Gravitational waves with matter

Let us now study how a system of free-falling particles interact with gravitational waves. The propagation of gravitational waves is a metric perturbation, but in the TT gauge it does not change the position of a test mass. To see the effect of the gravitational wave passage, we need at least two test masses and to consider their relative motion [2][4]. For example, let us consider two particles A and B , initially at rest, located along the x -axis of a frame: the A test mass is in the origin of the frame and the B test mass at the distance $x = l_{AB}$. The proper distance Δl_{AB} is obtained by computing:

$$\begin{aligned} \Delta l_{AB} &= \int \sqrt{|ds^2|} \\ &= \int \sqrt{|g_{\mu\nu} dx^\mu dx^\nu|} \\ &= \int_0^{l_{AB}} \sqrt{|g_{xx}|} dx \\ &\approx \sqrt{|g_{xx}(x=0)|} l_{AB} \approx \left[1 + \frac{1}{2} h_{xx}(x=0) \right] l_{AB}, \end{aligned} \quad (1.27)$$

where we expanded $g_{xx} = \eta_{xx} + h_{xx}$ via the first order Taylor series at $x = 0$. Thus, the travel time of light propagation between the test masses oscillates. The effect is directly proportional to the initial distance between the particles and to the amplitude of the wave (i.e. perturbation).

This effect, known as 'strain', can be defined with the Equation:

$$\frac{\delta l}{l} = \frac{1}{2}h_{xx}. \quad (1.28)$$

It gives a measure of how a gravitational wave can warp a mass distribution. Indeed, this effect can stretch and squeeze. Figure 1.1 shows how a circular-

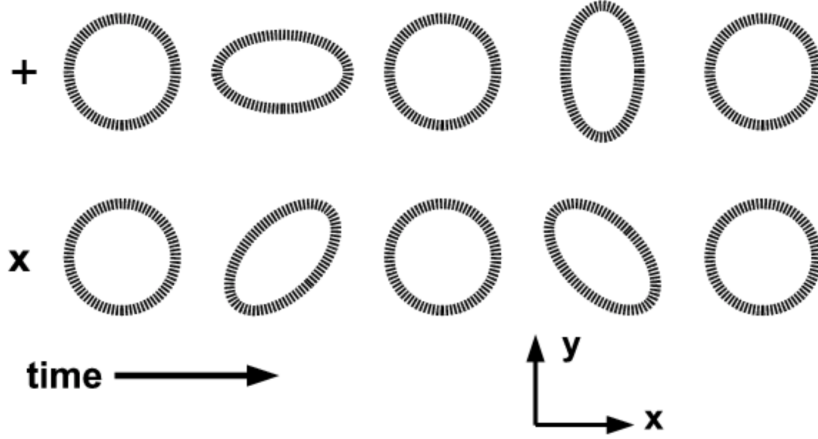


Figure 1.1: Schematic representation of the distortion effect due to the polarization states of a gravitational wave, propagating in the z direction [103].

shape mass distribution can be altered by the 'stretching and squeezing' effect due to its interaction with a gravitational wave.

1.1.4 Emission of gravitational waves

In the far field and slow-motion approximation we can use the solution derived from the retarded potential, and the gravitational wave amplitude generated by a given source can be written as [4]:

$$\bar{h}_{\mu\nu}(t, \vec{x}) \approx \frac{8\pi G}{3c^4 r} \ddot{Q}_{\mu\nu}, \quad (1.29)$$

where r is the distance between the source and the observer and $\ddot{Q}_{\mu\nu}$ is the second derivative of the quadrupole moment associated with the energy density of the source.

To estimate the order of magnitude of the intensity, we approximate the

quadrupole moment as:

$$Q \sim \epsilon MR^2 \longrightarrow \ddot{Q} \sim \frac{\epsilon MR^2}{T^2}, \quad (1.30)$$

where M is the total mass of the source, R is its typical dimension, T is the typical variation time of the system and ϵ is the factor measuring the asymmetry of the mass distribution. Since the speed of the masses inside the system is $v = \frac{R}{T}$, we can rewrite the expression 1.29 as follows:

$$h \sim \frac{1}{r} \frac{GM}{c^2} \epsilon^2 \left(\frac{v}{c}\right)^2. \quad (1.31)$$

Let us consider the constant factor $G/c^2 \sim 10^{-29} \text{ m}^3/\text{s}^4\text{kg}$: it is so small that only for astronomical sources (with a mass of the order of 10^{30} kg and/or relativistic speed $v \sim c$) we are able to detect gravitational waves. Similarly, it is possible to establish a superior limit for the frequency expected for a gravitational wave using today's laser interferometers. Considering a source with the Schwarzschild radius $\frac{2GM}{c^2}$ [4], the minimum period at which a source would emit gravitational waves would be:

$$P_{min} = \frac{4\pi GM}{c^3}. \quad (1.32)$$

Hence, we can estimate the maximum frequency for a gravitational wave:

$$f_{max} = \frac{c^3}{4\pi GM} \sim 10^4 \frac{M_\odot}{M} \text{ Hz}. \quad (1.33)$$

Then, among gravitational waves sources, those that emit at the highest frequencies would have masses close to the Solar mass (M_\odot), such as neutron stars.

1.2 Sources of gravitational waves

Gravitational wave detection strongly depends on the model of the emitted signal. Indeed, data analysis techniques rely on prior assumptions about features of the expected signal to be efficient. Theoretical investigations of

astrophysical sources made these analyses possible. GWs are classified into the following categories:

- **Periodic signals** [6][7];

Periodic signals sources emit at a nearly constant frequency. Neutron stars, pulsars, and binary systems belong to this category.

- **Transient signals** [9][92];

Those signals have short duration compared to the observational time. Among sources of transient signals, we have supernovae, gamma-ray burst sources and the coalescence of two massive compact bodies forming a binary system.

- **Stochastic signals** [89];

It is a matter of the sum of several contributions given by independent sources without a correlation. The stochastic background is one of the primary signals for a cosmological research: Superposition of signals from distant SNe and CBCs, or density fluctuations in the Big Bang, for instance.

Another useful method of classification is based on frequency dependence:

- extremely low frequency ($10^{-18} - 10^{-13}$ Hz):
 - stochastic sources, i.e. primordial gravitational fluctuations amplified by the cosmic inflation;
- very low frequency ($10^{-9} - 10^{-7}$ Hz):
 - stochastic sources, i.e. gravitational fluctuations due to fundamental interaction symmetry breaking;
- low frequency ($10^{-5} - 1$ Hz):
 - compact binary systems;
 - stochastic background, i.e. astrophysical and cosmological sources;

- high frequency ($1 - 10^4$ Hz):
 - compact binary coalescences,
 - spinning neutron stars;
 - transient sources such as stellar collapse, gamma-ray burst and supernovae;
 - stochastic background, expected from string theory or inflation model.

What follows is an overview of the abovementioned high-frequency sources.

1.2.1 Sources of periodic signals

- Neutron stars and pulsars

Neutron stars (NSs) [45] have a mass similar to the Solar mass but with a density 10^{14} times higher. In general, NSs have a low luminosity which makes them undetectable on Earth in visible light. Pulsars are a subgroup of NSs. They emit electromagnetic radiation in the radio frequency band, in a sequence of impulses with a frequency equivalent to the rotation frequency. The majority of neutron stars are known as pulsars, and their impulses have the duration of a one-millisecond order. Ordinary pulsars have a periodicity between 0.1 s and 4 s, while ultra-fast pulsars have a millisecond-long periodicity. Pulsars, since their rapid pulse of radio emission is so expected, must have an asymmetric mass distribution to emit gravitational waves. This situation can occur in the case of a lack of homogeneity on the surface during the star formation stage, or also in the presence of a superfluid core that generates a variation of the mass distribution at a surface level. It is possible to evaluate the gravitational signal coming from a known pulsar [6]. The emitted gravitational wave amplitude is given by [7]:

$$h_0 = \frac{16\pi^2 G}{c^4} \frac{\epsilon I_{zz} f^2}{r}, \quad (1.34)$$

where I_{zz} is the moment of inertia with respect to the rotation axis and its value strongly depend on the Equation of State of the neutron star. Studies show that, for a $1.338 M_{\odot}$ neutron star, the moment of inertia lies in the range $1.04 \times 10^{45} \text{gcm}^2 < I < 1.51 \times 10^{45} \text{gcm}^2$ at the 95% credibility level [110]. f is the sum of the star rotation frequency and the precession frequency, r is the distance from the star and ϵ is the equatorial ellipticity, defined in terms of the principal axis of inertia:

$$\epsilon = \frac{I_{xx} - I_{yy}}{I_{zz}}. \quad (1.35)$$

Pulsar	ν_{GW} (Hz)	d (kpc)	$\dot{\nu}$ (Hz/s)	h_0
Vela	22.38	0.28	-3.14×10^{-11}	3.38×10^{-24}
Crab	59.46	2	-7.42×10^{-10}	1.4×10^{-24}
J0205+6449	30.43	3.2	-8.96×10^{-11}	4.29×10^{-25}

Table 1.1: The most favourable pulsar sources within our Galaxy for current interferometric detectors.

A study provides an estimation for the equatorial ellipticity at 10^{-4} [111]. The amplitude for these signals is thought to be between $(10^{-27} - 10^{-24})$ [78]. Although this amplitude is low compared to that from compact binary coalescences, their stationarity in frequency and long time duration enables long integration times, increasing the signal-to-noise ratio. Additional information on LIGO searches for pulsars can be found in [103].

- **Binary systems**

Binary systems emit GWs in the presence of asymmetry of the mass distribution. Generally, their orbital periods last more than 1 hour, which correspond to a frequency emission $< 10^{-3}$ Hz. In 1973, Hulse and Taylor [8] discovered the PSR1913+16 binary system that represents the first indirect proof of a gravitational wave emission (see Figure 1.2) [8]. This binary system includes

a pulsar that rotates around a neutron star with a period of 7h 45min. Hulse and Taylor measured a decreasing period. This result was in contrast with Kepler's laws, under which the orbital period, in a classical system, is a constant of motion. It was a clear signal of the relativistic nature of that system. GW emission was a hypothesis to explain that energy loss: the speed increases and the orbital distances decrease when we are in the presence of two bodies that rotate around each other, like a dancer who brings his arms close to the body for a pirouette. This increases the frequency of gravitational waves until the moment of coalescence. Note that non-coalescing binaries are not detectable by ground-based detectors such as LIGO, due to their low frequency. These binaries are Laser Interferometer Space Antenna (LISA) targets.

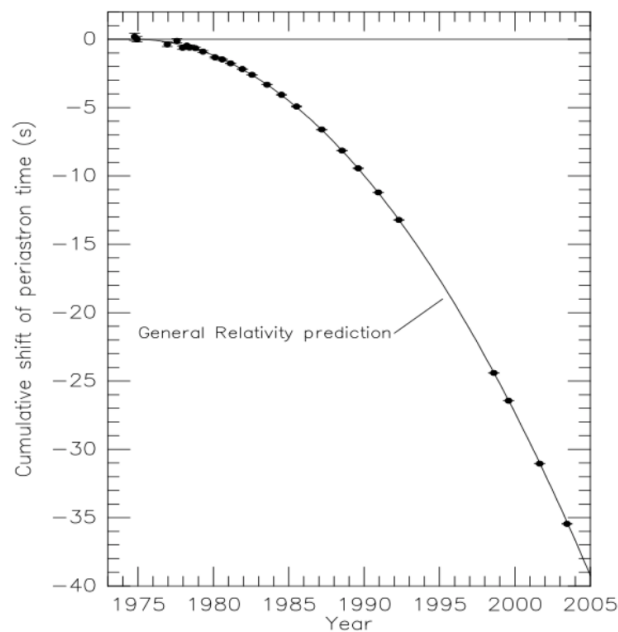


Figure 1.2: PSR 1913+16 system. Energy losses due to gravitational radiation, predicted by GR, is represented by the parabolic curve [103].

1.2.2 Transient signals sources

- **Coalescing binary system**

Binary systems consist of two companion stars subjected to a mutual gravitational attraction dominant over the gravitational attraction due to all the other stars that surround them [5]. The coalescence of two bodies constituting a binary system can be divided into three phases, each of which corresponds to a different type of gravitational signal emitted, periodic or semiperiodic:

1. the inspiral phase, in which the star orbits contract adiabatically over hundreds of millions of years; the angular velocity increases and the separation among stars decreases;
2. the merger, in which the two stars are moving at a third of the speed of light, until the collision;
3. the ring-down, when the two stars have merged to form a super-massive object, settling down to a quiescent state.

Restricting ourselves to sources detectable by LIGO in the merger phase, the binary system can be formed by two black holes (BBH), by one black hole and a neutron star or by two neutron stars (BNS). The difference among these configurations is the duration of the signal in which those objects emitted gravitational waves. When the inspiral phase begins, wavefront becomes a chirp signal (Figure 1.3 and [9]). That signal increases its amplitude and frequency with time until the two compact objects are merged. The signal is described in terms of orbital frequency (f), and chirp mass (\mathcal{M}) defined as a combination of the two masses (M_1 and M_2) that are merging.

The frequency of the emitted gravitational wave is:

$$f = \frac{1}{\pi} \left(\frac{G(m_1 + m_2)}{a^3} \right)^{1/2}. \quad (1.36)$$

Where a is the orbit semi-major axis. The *chirp mass* is:

$$\mathcal{M} = \frac{(m_1 m_2)^{3/5}}{(m_1 + m_2)^{1/5}} = \frac{c^3}{G} \left[\frac{5}{96} \pi^{-8/3} f^{-11/3} \dot{f} \right]^{3/5}. \quad (1.37)$$

During this phase, the signal amplitude is:

$$h \sim \frac{1}{r} \mathcal{M}^{5/3} f^{2/3} \quad (1.38)$$

The merger phase corresponds to a violent settling motion of the two objects which, due to its complexity, has not been yet described by an analytical model [79, 80].

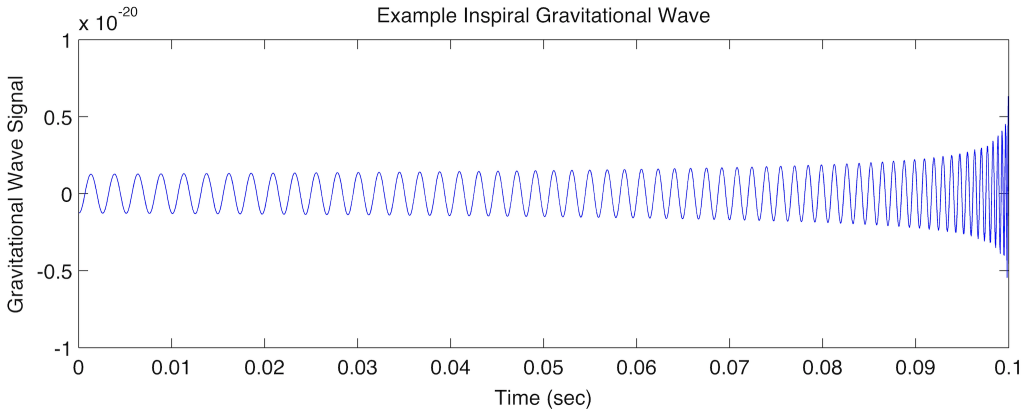


Figure 1.3: Gravitational wave signal emitted from a coalescing binary system during the inspiral phase. System of two black holes of mass M_1 and M_2 the coalescence at $t=0.1$ seconds. (Image:A.Stuver/LIGO)

The first direct detection ever made of a gravitational wave transient signal matches the features presented below (Figure 1.4). This event [5], named GW150914, was observed on September 14 2015, at 09:50:45 UTC by the two detectors of the Laser Interferometer Gravitational-Wave Observatory (LIGO). The signal was observed with a false alarm rate estimated to be less than 1 event per 203 000 years, equivalent to a significance greater than 5.1σ . The source lies at a luminosity distance of about 410 Mpc. The signal increases in amplitude and frequency from 35 to 150 Hz, where the amplitude reaches its maximum value. The chirp mass can also be calculated knowing

the frequency, as shown in Equation 1.37. Additional information can be found in [5].

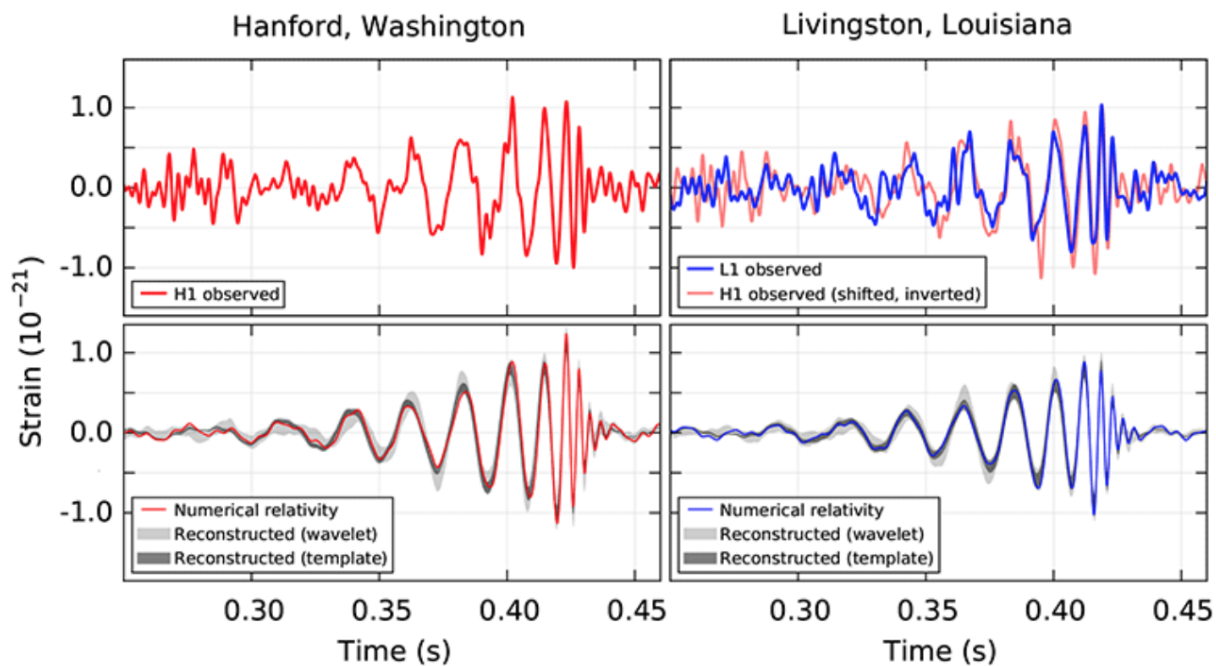


Figure 1.4: GW150914 event observed by the LIGO Hanford (H1, left column panels) and Livingston (L1, right column panels) detectors. GW150914 arrived first at L1 and 6.9 ms later at H1; for a comparison, the H1 data are also shown, shifted in time and inverted to include the detectors relative orientations. Red and blue lines, in the bottom rows, show a numerical relativity waveform for a system with parameters consistent with those recovered from GW150914 [84].

- **Supernovae**

Supernovae (SN) [92], according to the process responsible for their formation, are stellar explosions representing the end points of some main sequence stars. They are divided into type I supernovae and type II supernovae (Figure 1.5).

- the collapse of oxygen-magnesium-neon and carbon oxygen white dwarfs due to the Chandrasekhar limit (Type I supernovae);
- the collapse of iron or oxygen-magnesium-neon stellar cores of massive stars (Type II supernovae).

Gravitational waves, additional to neutrinos, are a complementary method to look at heart of supernova: They decouple from matter directly after generation (i.e. synchronicity with core collapse) and their amplitude decays linearly with distance. SN rates have been measured with respect to various galaxy properties: Studies report that to detect core-collapse supernovae with an event rate of one per year, the gravitational-wave detectors need a strain sensitivity of $3 \times 10^{-27} \text{ Hz}^{-1/2}$ in a frequency range from 100 Hz to 1500 Hz [104].

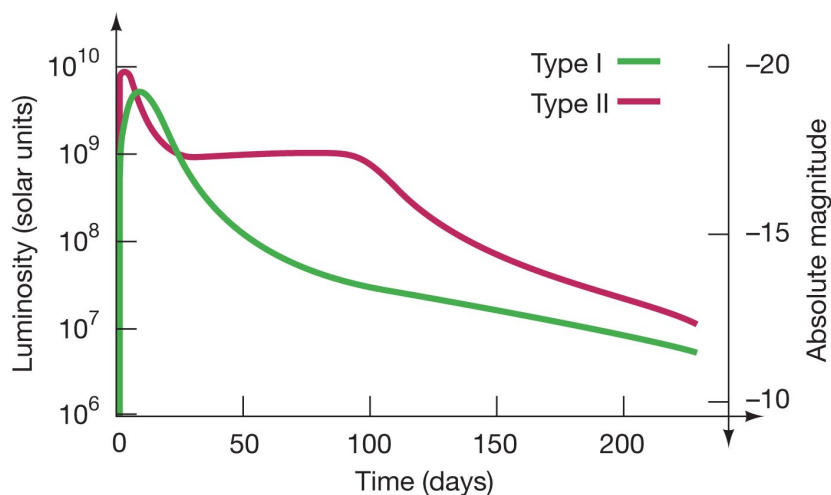


Figure 1.5: Example of Type-I and Type-II supernovae light curves. Type-II curves have a characteristic bump in the declining phase [102].

It can be found that the typical amplitude of emitted gravitational waves is given by [105]:

$$h \approx 2.7 \times 10^{-20} \left(\frac{\Delta E}{M_{\odot} c^2} \right)^{1/2} \left(\frac{1 \text{ kHz}}{f_c} \right) \left(\frac{10 \text{ Mpc}}{r} \right) \quad (1.39)$$

where ΔE is the energy loss by GW emission, r is the distance from the observer and f_c is the emitting frequency in the range $(10^2 - 10^3)$ Hz. Since the duration of the supernova pulses is very short, about 1 ms, it is possible to detect only the peak of the produced signal and not its entire structure. Predicted total emitted GW energies are in the range $10^{-12} - 10^{-8} M_{\odot} c^2$ [106]. Additional information on GW emission in core-collapse supernovae can be found in [106].

- **Gamma-ray bursts**

Gamma-ray bursts (GRB) [82] are the most luminous explosions in the universe: they are short and intense bursts of about $(10^{51} - 10^{54})$ erg/s which last from 10 ms to 1000 s. They were accidentally discovered in 1967 [107] and at first it was thought they were originated by galactic neutron stars. Then, through follow-up observations [85] of the X-ray, optical and radio emission of GRB and thanks to determination of their sky location, redshift and host galaxy, their extra-galactic origin at cosmological distances became evident. Their principal characteristics are:

1. the isotropy on the sky;
2. the lack of bright persistent counterparts;
3. their non-thermal spectrum.

GRB are divided into short gamma-ray bursts (duration < 2 s) and long gamma-ray bursts (duration > 2 s) [86]. Progenitor bodies [84] of the GRBs are assumed to be different for the long and short ones. For long GRBs, progenitor bodies are thought to be rotating and very massive stars which undergo gravitational collapse.

On the other hand, the GW170817 event [55] has established that short GRBs [87] are due to NS binary coalescence and BH-NS coalescence. Occurring on August 17th 2017 (GW170817) [58], it was the detection of the first event generated by the merger of two neutron stars and, it represents the beginning of the new “multi-messenger era”[59], since electromagnetic radiation was detected in association with the production of a gravitational wave.

The consequence of the two different scenarios is the same and coincides with the formation of a black hole surrounded by its accretion disk. Short GRBs [83] are the most frequent GRBs. Studies suggest a maximum detectable SGRB all-sky rate of $< 4y^{-1}$ in the local universe ($d \lesssim 200Mpc$) [108]. There is less data on long GRBs. An alternative scenario is that of a magnetar. These are neutron stars with high rotational speeds and a magnetic field 10^3 times that of a ‘standard’ neutron star, of order 10^8 T. The

afterglow [10] follows the explosion of a GRB and starts when the external interstellar medium collides with the blast wave, and this collision produces an external shock. Afterglow represents the light curve of the pulse and is characterized by a steep-flat-steep pattern as shown in Figure 1.6.

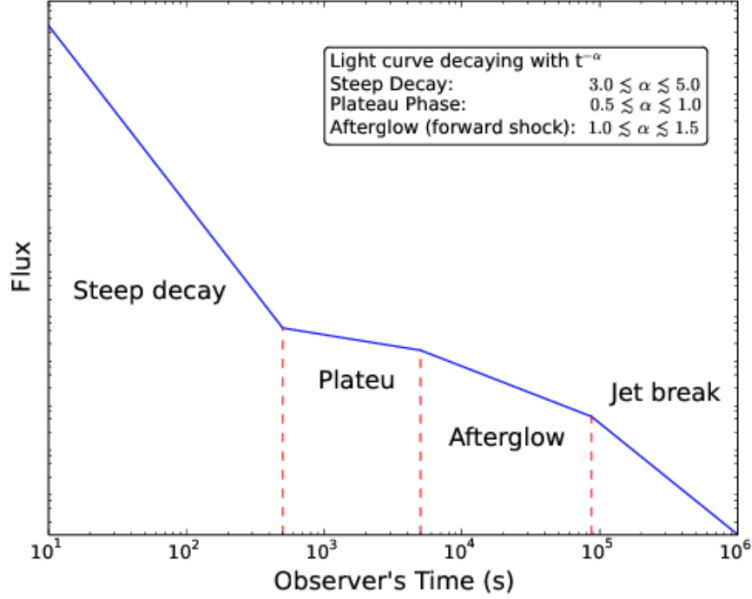


Figure 1.6: Canonical light curve of the X-ray afterglow [101].

A gravitational wave emission occurs in the flat phase (plateau) of the afterglow; in the particular case of the magnetar, considering an ellipsoidal model to describe its shape, the expected amplitude of the GWs emitted, likewise **neutron stars and pulsars** (see Equation 1.34), is [9]:

$$h = \frac{4G\Omega^2}{c^4 d} I \epsilon, \quad (1.40)$$

where I is the moment of inertia of the star with respect to the axis of rotation, Ω is the angular frequency, ϵ is ellipticity and d is the distance from the source. A paper on gamma-ray bursts and magnetars reports that “A magnetar born with a rotation rate of ~ 1 ms contains a large amount of energy $\dot{E} = 0.5I\Omega^2 \sim 3 \times 10^{52} \text{erg}$ for a moment of inertia $I = 80 \text{Km}^2 M_{\odot}$ ”. The possible emission frequency is between ($10^2 - 10^3$) Hz. Studies report

that the spin-down luminosity of an ultra-magnetized millisecond neutron star and fallback onto a newly formed black hole can fuel the X-ray afterglow plateau emission observed in many Gamma-ray Bursts (GRBs) [109].

1.2.3 Stochastic background

The stochastic background [89] is the gravitational equivalent of the cosmological microwave background (CMB) [91]. The stochastic background radiation, if detected, would provide critical information both for high energy physics and for the truthfulness of the cosmological theories elaborated so far. It is assumed that the stochastic radiation is isotropic (similar to CMB), non-polarized (polarization equivalence $+$ and \times) and stationary (statistical quantities do not depend on the choice of the initial time).

The mechanisms underlying the stochastic background have been the subject of numerous studies; they all agree that it was formed in the moments immediately following the decoupling of the gravitons from the primordial plasma. Currently, the most accredited hypothesis to explain its formation is that of the Inflationary Model [11]. A review on stochastic gravitational waves reports that: “The gravitational waves produced in the early universe will have frequencies today that extend to at least 10^{14} Hz, if not higher. However, for LIGO and Virgo, their observational band (from 10 Hz to a few kHz) is likely to be dominated by a stochastic background produced by the merger of binary black holes and binary neutron stars over the history of the universe.”[113].

1.3 Gravitational waves detection

1.3.1 Laser interferometers

The theoretical bases of the detection of gravitational waves reside in the equation of the geodetic deviation that describes the variation of the distance between two free masses in conjunction with the passage of a GW. Detection of distance variation can be done with a detector based on the Michelson

interferometer. The principle of detection of an interferometer is to observe the delay of a laser accumulated in one arm with respect to the other by the variation of the phase measured at the output of the same.

Various interferometers dedicated to the search for gravitational waves are currently active or under development (Figure 1.7). The Laser Interferometer Gravitational-Wave Observatory (LIGO) was built between 1994 and 2002 and, collected data from 2002 to 2010 but no detection of gravitational wave has been made. The Advanced LIGO Project to enhance the original LIGO detectors began in 2008. The LIGO project consists of two interferometers located at two different sites. The 4 km interferometers are active in Hanford (USA) and in Livingston (USA) [12]. Observations are made in "runs". As of December 2019, LIGO has made 3 runs, and made 50 detections of gravitational waves.

The VIRGO project, located in Cascina (Italy), consists of an interferometer with 3 km arms and is characterized by a higher sensitivity bandwidth than the other interferometers. In particular, the band is extended in the low-frequency zones. The considerable improvement is obtained employing a seismic damping system[13], known as superattenuator. It is a chain of mechanical filters, designed to filter the vibrations in all degrees of freedom. An overview on the superattenuator seismic isolation used by Virgo interferometer can be found in [115].

GEO600 is a smaller interferometer (the length of its arms reaches 600 m) and therefore also the least sensitive [14].

Except for GEO600, located in the South of Hanover (Germany), other projects such as KAGRA (Hida-city in Japan), INDIGO (Maharashtra in India) and Fermilab Holometer (USA) involve the creation of instruments with the same basic optical scheme: a Michelson interferometer with the arms formed by Fabry-Pérot cavities and equipped with recirculating power mirrors.

In March 2020, with 3km-long arms, KAGRA has begun making real-time observations. It is one km smaller than LIGO, but has some newer technology, such as cryogenically cooled mirrors, which will improve the capability in detecting gravitational waves. INDIGO, once it becomes operational, will

be an additional detector to the existing network. The radical improvement from INDIGO would come in the ability of localizing GW sources in the sky. Further information on ground-based detectors can be found in [114].

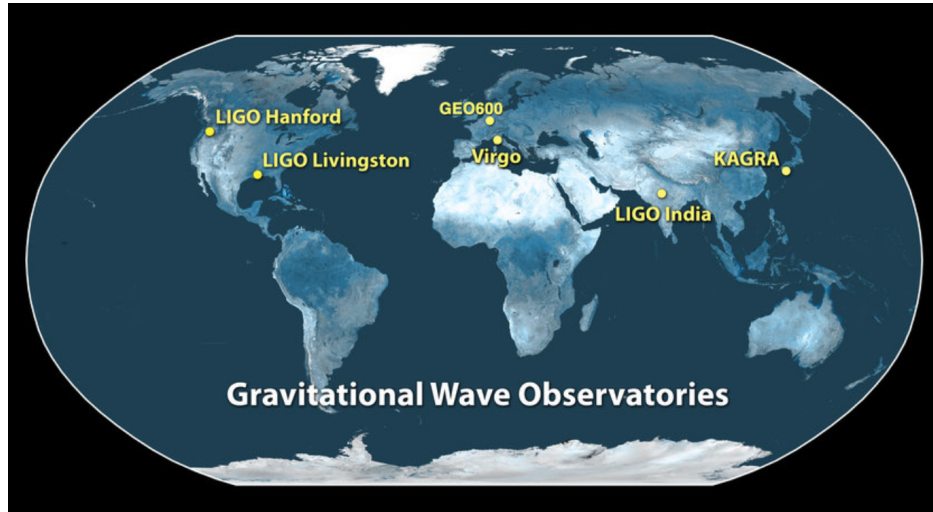


Figure 1.7: World network of GWs detectors [96]. 4 km-long arms interferometers are located in Hanford (USA) and in Livingston (USA) and they are active nowadays. Alongside these American detectors, you find GEO600, VIRGO and KAGRA, all active. INDIGO is under construction. Once it will be operational, a dramatic improvement in GW sources localization is expected.

1.3.2 Interferometer operating principle: advanced LIGO

The direct measurement of gravitational waves [9] consists of the detection of an intensity variation in interference patterns. GWs are expected to produce oscillatory tidal distortions to modify the optical path length of the two laser beams, thereby inducing a shift of the interference fringes observed at the interferometer output and thus giving the possibility to detect the effects of a gravitational wave directly. A schematic description of advanced LIGO (aLIGO) can be found in Figure 1.8 [95]. The aLIGO consists of a Michelson

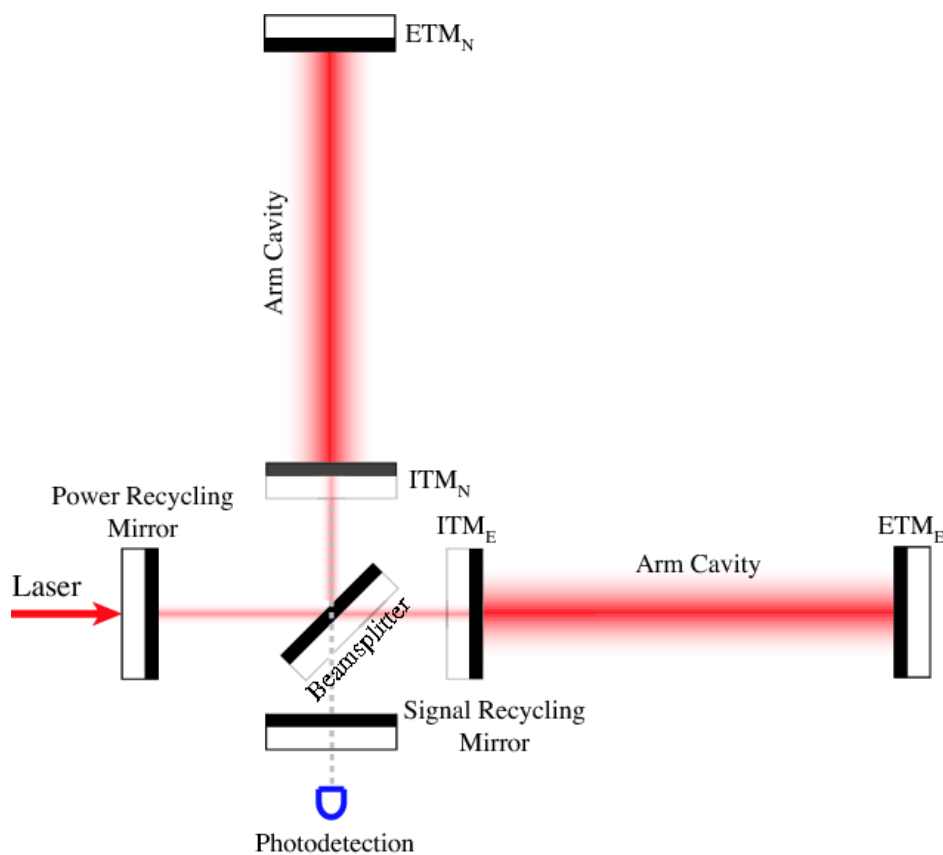


Figure 1.8: A schematic showing Advanced LIGO's interferometer [98]. The detection is based on the phase difference between the light returning from each arm. Fabry-Perot arm cavities are used for the interferometer arms to increase the time of exposure of the laser light to the gravitational wave, and there is a power recycling mirror between the laser and beam-splitter to increase effective laser power.

interferometer pumped by 1064 nm near infrared laser light [98].

Compared to the initial LIGO that operated between 2002 and 2010, in the Advanced LIGO [94], through a particular amplification, the power has been increased from $\sim 10\text{W}$ to $\sim 50\text{W}$. This upgrade significantly reduces high-frequency quantum noise. A Power Recycling mirror is introduced to increase the optical power of the beam by sending back to the beam splitter that part which had been rejected at first.

A beam splitter is placed in line with the laser. This beam splitter is a mirror, inclined 45° to the direction of laser propagation, which divides the laser into two perpendicular beams. The two split beams are injected into the Fabry-Perot arm cavities, formed by two suspended mirrors placed at a distance of $\sim 4\text{ km}$ from each other.

There are Test Masses mirrors (input TMs and end TMs in Figure 1.8) used to test the passage of gravitational waves. In the arm cavities, the optical power of the laser is amplified by a factor of around 100. Increasing the optical power of the laser implies an increase in the sensitivity of the interferometers. A higher number of photons inside the beam makes interference patterns clearer, giving the possibility to notice smaller variations of the same patterns. Once the two beams enter the Fabry-Perot cavity, the mirror system allows the lengthening of the laser optical path within these cavities. The beam rebounds about 100 times between the incoming mirrors and those anchored on the final Test Masses.

Increasing the effective length increases the sensitivity of the interferometer to the vibrations caused by a gravitational perturbation. Once the two beams exit the Fabry-Perot cavities, they are recombined by the beam splitter and directed towards the detection system that analyses their interference patterns. There is a Signal Recycling Cavity, formed by the 'Signal Recycling' mirror and the two input test masses. It is used, as the Power Recycling mirror, to increase the signal at the output. An apparatus of this type, equipped with power and signal recycling, is called "Dual-Recycled Michelson Interferometer" (Figure 1.8).

1.3.3 Noise sources

A reliable detection requires a careful evaluation of noise sources. Several types of noise can contaminate measurements, and LIGO detectors are not immune [16]. These contaminations depend on the nature of sources. Detectors can be affected by real movements of test masses or by instrumental limits. Last-generation detectors deal with more tricky noise contaminations, such as seismic, thermal and quantum noise [16]. Concerning LIGO detectors (Figure 1.9), seismic noise has an impact below 10 Hz. The ground moves $\sim 10^{-9}\text{m}/\sqrt{\text{Hz}}$ to 10 Hz. The thermal noise of the suspensions causes the movement of the Test Masses tests due to the thermal vibrations of the suspension fibers. Quantum noise is governed by the limit imposed by shot noise: One of the most relevant intrinsic noises in interferometric type measurements is due to the use of lasers. In the ideal case of a perfectly stable laser beam in frequency and power, phase fluctuations are limited by the Heisenberg uncertainty principle. Due to the corpuscular nature of the light the photon count undergoes fluctuations from which the shot noise originates. The fluctuations are of the Poissonian type, the standard deviation is therefore $\sigma_N = \sqrt{N}$, where N is the number of photons incident on the detector. It limits the detector's sensitivity above 100 Hz.

Residual gas molecules present in the instrumentation generate a diffusion phenomenon, which causes a refractive index fluctuation that results in a phase noise of the laser beam [96]. Figure 1.9 [16] shows the limiting noises as functions of frequency.

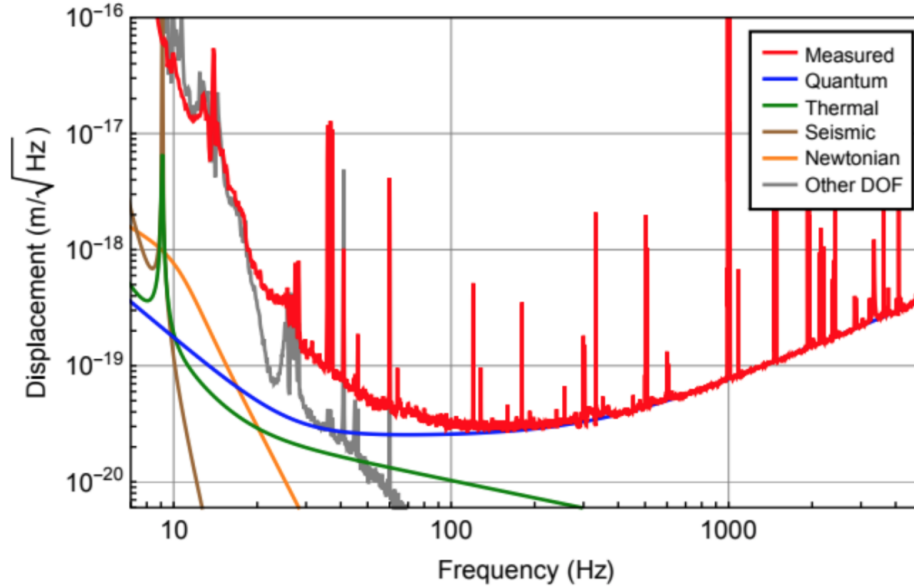


Figure 1.9: Sensitivity of the aLIGO detectors [16]. The daily operation of the interferometer is strongly influenced by different sources of noise that affect the detection of the gravitational signal. Schematically, you can group the noises into two categories: real movements of test masses and instrumental limits. The first group includes all those disturbances that cause the displacement of the test masses, the mirrors, and of all the optical elements crossed by the laser beam (seismic noise, thermal noise, etc.). On the other hand, all those disturbances belong to the second group which, while not producing any movement of the optical components, give rise to a spurious fluctuation of the phase between the interfering beams, thus simulating the passage of a gravitational signal (laser frequency noise, fluctuations of the refractive index of the residual gas inside the vacuum tubes, etc.).

1.3.4 Detections list

Observations are made in "runs". As of March 2020, LIGO has made 3 "runs", and made more than 50 detections of gravitational waves. The observing run 'O1' consisted of 130 days of data collection using the two-detector network at Hanford, WA (H1) and Livingston, LA (L1). In September 2015, Advanced LIGO welcomed the era of gravitational wave astronomy with its first observation session. This session culminated with the first direct detection of gravitational waves, called GW150914, coming from the coalescence of a binary system of black holes, which merged at about 400 Mpc away from the Earth. Observing Run 'O2' started in November 2016, with both LIGO and Virgo detectors operated together since August 1, 2017. The LIGO-Virgo collaboration began the observing run O3 on April 1, 2019; it ended early on March 27, 2020 due to the COVID-19 health emergency.

Figure 1.10 reports some of the first detections made by the LIGO-VIRGO detectors. A full overview, up-dated to April 2020 can be found in [97][116, 117].

DETECTION	DESCRIPTION
GW150914	The first direct detection of gravitational waves(GWs). The gravitational wave signals were observed by the LIGO's twin observatories on September 14, 2015. The signals came from two merging black holes (BHs), each about 30 times the mass of our sun, lying 1.3 billion light-years away.
GW151226	The GW signals were observed by the LIGO's twin observatories on December 26, 2015. The two BHs weighed in at 14 and 8 solar masses.
GW170104	The GW signals were observed by the LIGO's twin observatories on January 4, 2017. The two BHs weighed in at 31 and 19 solar masses.
GW170608	The GW signals were observed by the LIGO's twin observatories on June 8, 2017. The two BHs weighed in at 12 and 7 solar masses.
GW170814	The detected gravitational wave was observed on August 14, 2017 and was produced by a pair of merging black holes with 31 and 25 solar masses.
GW170817	The first observation of gravitational-waves from a binary neutron star (NS) inspiral. . The two NSs weighed in at 1.5 and 1.2 solar masses.

Figure 1.10: First detections of gravitational-waves made by the LIGO-VIRGO detectors. Detections information taken from [100].

The results obtained from the LIGO-Virgo collaboration, starting from

the first signal revealed in the 2015 represent a real direct verification of the existence of gravitational waves, and therefore provide a new and important experimental proof of the theory of general relativity, which it is added to the previous and well-known experimental tests (the deflection of light, the precession of the perihelion, the delay of radio signals, etc.). In addition, the revelation of these waves gives us evidence of the existence of black holes. In fact, the gravitational interaction of two black holes leading to their merger, and the formation of a final black hole, represents the most accredited theoretical model capable of acting as source to the signals that the gravitational antennas have detected. The direct detection of gravitational waves, in particular the study of their properties (carried out by analyzing the data provided by the antennas), has important implications not only for gravitational theory but also for a unified theory of all fundamental interactions: for example , for string theory. The experimental results on waves, in fact, give us positive - albeit indirect - indications on the possible existence of this theory, because they confirm that gravity behaves like all other forces regarding the processes that regulate the emission and propagation of radiation. In particular, they confirm that we can also correctly associate an appropriate energy-impulse tensor to gravitational radiation, which describes its flow, energy density, and which, above all, obeys the fundamental law of energy conservation. These results, which are not obvious, in principle, given the "geometric" nature of gravitational energy, and given the fact that the geometric description varies depending on the observer and the coordinate system used, encourages us, not to think that gravity can also be included in a theoretical model that describes all the fundamental forces of Nature. The waves recently revealed by LIGO-Virgo have no direct implication for cosmology because they were emitted in a too "recent" era (compared to the cosmic time scale). The famous cosmic microwave background radiation, that is studied in cosmology, was instead produced in much more remote times. In any case, it is the gravitational waves, and not the electromagnetic ones, that can give us direct information on the most remote history of our Universe, and in particular on the epochs immediately following (or preceding) the Big Bang. It therefore becomes very important to study the properties of this

background and to ask, in particular, if its intensity can produce detectable signals in the frequency band to which the current antennas are sensitive.

Chapter 2

Long-duration burst signals searches

2.1 Introduction and Motivation of Research

In the context of gravitational wave data analysis, the word 'burst' has come to mean a waveform having a limited time duration for which no detailed theoretical model exists. The lack of theoretical predictions make this research both ambitious and complicated. We must proceed using more general techniques where only the most general constraints are imposed on the target signals. For example, we may constrain our search to waveforms having a particular range of time durations, or a particular range of frequency bandwidths. Astrophysical models provide some known sources which would result in bursts. These include supernovae [73], long duration gamma ray bursts [86], and high eccentricity binary mergers. The latter could generate, in the moments before the merger, bursts signal, emitting portions of the binding energy [118].

The work described in this thesis is connected to the work of the 'Burst' group of the LIGO Scientific Collaboration (LSC), covering searches for burst signals of durations in the range from 10 seconds to a few minutes. Again, astrophysical models of sources hypothesised to cause long duration bursts exist. Asymmetric magnetars [17,18] may be the progenitors of the observed

short and long classes of gamma ray burst [19,20] [119, 120]. Simulation studies of newly formed neutron stars indicate a phase where chaotic fluid motion, a few seconds after the core collapse, may also result in such signals [22]. In these cases, multi-messenger searches, using both electromagnetic and gravitational wave observations, should result in improved performance: Since electromagnetic radiation, gravitational waves, neutrinos and cosmic rays are generated by different astrophysical processes, they can reveal different information about their sources and provide newly acquired knowledge. The detection of one of these signals and the failure to detect another by the dedicated detector can also be a great tap of information on the source event. The GW170817 event represented the first time that a gravitational wave signal could be observed together with its electromagnetic counterpart, marking a truly epochal event in the history of multi-message astronomy.

Gravitational-wave searches need fast analysis algorithms and robust noise rejection methods due to the non-Gaussian non-stationary nature of detector noise [102]. Two pipelines devoted to the long-duration burst searches are involved in this work: The X-Pipeline Spherical Radiometer (X-SphRad) [30, 35, 41] and the coherent WaveBursts (cWB) [40, 41]. cWB performs a time-frequency analysis and identifies excess power pixels while X-SphRad uses coherent sky energy as defined in Section 2.3. X-SphRad aims to perform a fast all-sky search working in the spherical harmonic domain. One benefit of this automated algorithm is having the spherical harmonic coefficients stored during the analysis. Edwards et al. [38] have shown how spherical harmonic coefficients can be used to identify and reject non-Gaussian non-stationary noise and instrumental artifacts, called from now 'glitches'.

Indeed, we use spherical harmonics as a glitch [53] rejection statistic already, but glitches are hindering the search at the selection step of potential candidate events. This implies that glitches can appear as candidates with very high statistics. This seriously limits the pipeline ability to follow up on non-glitch potential GW candidates around the time of a loud glitch.

Therefore, applying a method which rejects glitches before creating the candidate events list will mean a potential improvement in the search sensitivity. In Chapter 3, we provide a full discussion of a new noise rejection

method and results obtained by its application.

Before testing the new rejection method, we have also performed with both X-SphRad and cWB, a comparative analysis on 20 days of data collected during the observing run O2.

O2 run took place from 2016 Nov 30th 16:00 UTC (GPS 1164556817) to 2017 Aug 25th 22:00 UTC (GPS 1187733618). Data are available from three detectors, H1, L1 and V1 (Virgo joined on the 1st of August 2017). The O2 data set is available at the original 16 KHz and the downsampled 4KHz sample rates. This is the first observing run that includes both Advanced LIGO and Advanced Virgo data.

Efficiency studies have been performed among waveform models described in section 2.2. Results show that X-SphRad and cWB have different performances depending on the family of the injected waveforms.

2.2 Waveform models

Currently, there are several sources of long-duration bursts signals but there is a shortage of detailed waveform models. At present, the pipelines involved in the search for these signals use astrophysical waveform models such as:

- Van Putten Accretion Disk Instabilities and fragmentation (ADI) and Instabilities in central magnetars [16];
 - In these models, the quadrupole components of the disk turbulence lead to GW emission that spin down the BH. The ADI family covers a frequency range of 110-260 Hz with minute long signals, while the magnetar family covers the middle and higher end with longer duration. To estimate the detectability of the waveforms, we can construct an optimal SNR as the SNR needed to recover 50% of the waveforms: tests show that the optimal SNR grows with duration and bandwidth, because the waveform energy is spread over a longer period in the time-frequency space. Detectability can be calculated as $D_{detectability} = \frac{SNR}{V^{1/4}}$, where V is the volume in the time-frequency plane [30].

- Rotational instabilities in Proto-Neutron Star (PNS) remnants [18];
 - In this model, nonaxisymmetric distortions did not grow to particularly large nonlinear amplitudes, they produced maximum GW amplitudes comparable to the “burst” signal produced by the preceding, axisymmetric core collapse: The peak amplitude of the axisymmetric bounce signal reported in [61] was at a frequency $f \approx 400$ Hz.
- Fallback accretion on neutron stars [22];
 - The model’s scenario refers to core-collapse supernovae that release itself of its stellar mantle with a weak collapse [62]. This condition means that a young NS will be subject to a fallback accretion, a process that will increase the mass up to its limit leading to BHs. This model is described in Chapter 4.

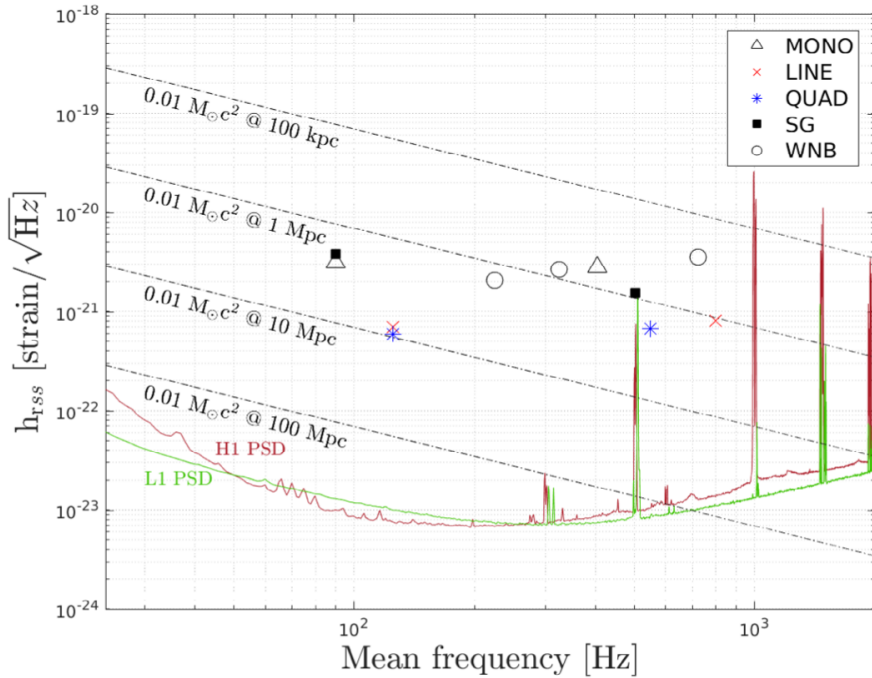


Figure 2.1: Gravitational-wave strain versus frequency for some waveform models for burst signals. From [79].

Moreover, to try to cover all possible scenarios, “ad-hoc” waveforms ((Figure 2.1 [76]) are used to widen the space of signal morphologies in our studies of pipeline properties. The “ad-hoc” waveforms employed are:

- Sine gaussian;
 - these waveforms are simple unipolar monochromatic signals described by $h = \exp^{-t^2/\tau^2}$ multiplied by a Gaussian envelope.
- White Noise Burst;
 - these waveforms are white noise band-passed signals with a Gaussian time envelope.
- Linear and Quadratic;
 - these waveforms are described by $x = A\sin(2\pi f(t)t)$.
- Monochromatic:
 - these waveforms are described by the equation $x = A\sin(2\pi f(t)t)$; they are signals oscillating at a single frequency that does not change over time.

Figure 2.2 shows an empirical representation of these ad-hoc waveform classes. Those names correspond to the frequency evolution in time of the ‘ad-hoc’ waveforms. More details on “ad-hoc” waveforms can be found in Section 3.7.2 of [30]. Because long duration burst searches are intended both for detection of signals from the predicted sources listed in Section 2.1 and for serendipitous discovery of unanticipated signals, there is a danger that analysis tweaks shown to improve efficiency for some waveform classes may in fact limit sensitivity to other burst signals.

It is crucial, then, to look for techniques to discriminate signal from noise, which influences the reconstruction of the signal itself. To limit this risk, various statistical methods are applied in order to increase the probability of survival of only potential real candidates. These techniques will be described in Chapter 3.

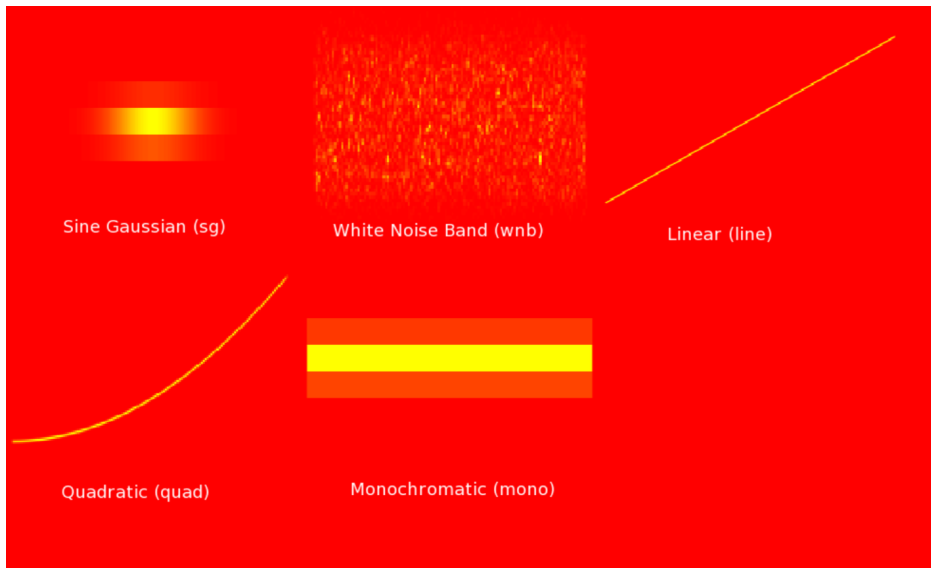


Figure 2.2: Graphic illustration of Ad-hoc waveforms to show how their signal reconstruction looks like on the time-frequency plane. From [104].

2.3 The X-Pipeline Spherical Radiometer

X-SphRad [26][34, 30] is a tool in gravitational wave analysis, for long-duration burst-like signal searches. Specifically, it is a pipeline used to perform an all-sky search for long-duration signals, and analyse the data produced by LIGO detectors during the Observational runs O1 and O2 [76, 77]. It is based on X-Pipeline, a Matlab-based software for burst searches, developed by Sutton et al [26]. A spherical radiometer approach is applied in X-Pipeline to decrease the computational cost of the analysis [25].

The radiometer pipeline consists of a set of fast cross-correlator codes written in C, and it computes data streams correlations into a spherical harmonic domain. The spherical radiometer approach forms the lowest order multipoles on the sky using the sum of the squares of the spherical harmonics Y_{lm} . The spherical radiometer algorithm is explained in the Subsection 2.3.2.

2.3.1 Formalism in X-Pipeline

In this section, we give an overview of the formalism used in X-Pipeline. We start formally with Equation 2.1 [28] that shows how a time-series data can be expressed as a linear combination of the antenna response function, $F(\Omega)$, (dependent on the sky position and on the position and orientation of the gravitational wave detectors), the gravitational wave (dependent on the source polarisation) and the noise contribution:

$$d_\alpha(t + \Delta t_\alpha(\hat{\Omega})) = F_\alpha^+(\hat{\Omega})h_+(t) + F_\alpha^\times(\hat{\Omega})h_\times(t) + n_\alpha(t + \Delta t_\alpha(\hat{\Omega})) \quad (2.1)$$

Where:

- α indicates the specific detector [1,...,D];
- $+$ and \times , plus and cross respectively, correspond to the two polarizations of a gravitational wave;
- $\hat{\Omega}$ is a unit vector pointing to the source position on the sky;
- $\Delta t(\hat{\Omega})$ is the time-delay generated by the different arrival time of the GW on the detectors in earth-centric coordinates and, it can be expressed by Equation 2.2 [28]:

$$\Delta t(\hat{\Omega}) = \frac{1}{c}(\vec{r}_0 - \vec{r}) \cdot \hat{\Omega}. \quad (2.2)$$

Where \vec{r}_0 is an arbitrary reference position and \vec{r} is the detector position.

The basic premise of X-pipeline [26] is that for any given sky position, for each detector in a network, a signal can be decomposed into components in two orthogonal polarisations. The response of n detectors to this signal is therefore an n -dimensional vector. Then, a set of physical signals, from that sky position, forms a subspace of all the possible vectors [28].

Noise, by contrast, will populate the full vector space of interferometer outputs. Following the reasoning, by comparing the energy (total or referred to a specific polarization) in the vector subspace corresponding to signals with

the energy in the whole vector space, we can build efficient discriminators between astrophysical signals and instrumental noise background.

The total energy in a data-stream for each detector in the network is defined as follow (Equation 2.3) [26]:

$$E_{tot} = \sum_k \left| \tilde{d} \right|^2 \quad (2.3)$$

Where \tilde{d} is given by Equation 2.1, k $[1, \dots, N]$ and N is the number of data points in the time domain. This quantity is an auto-correlation information because it is computed for each detector independently.

The decomposition of the data-stream into the two orthogonal polarisations provides (Equations 2.4 and 2.5):

$$E_+ = \sum_k \left| e^+ \cdot \tilde{d} \right|^2 \quad (2.4)$$

$$E_\times = \sum_k \left| e^\times \cdot \tilde{d} \right|^2 \quad (2.5)$$

Where e_+ and e_\times are the unit vectors which represent the directions of F_+ and F_\times [4].

The energy in the whole vector space, instead, is composed of elements of cross-correlation and auto-correlation. This auto-correlation energy is called Incoherent energy (I_\times) and is attributable to the presence of a detected glitch. In X-Pipeline, this Incoherent energy and its plus and cross components are used to discriminate a signal from a false alarm, comparing E_+ and E_\times with the I_+ and I_\times respectively. In the case of a gravitational wave signal where h_+ polarization predominates, we have:

$$E_+ > I_+ \quad (2.6)$$

In the case of a gravitational wave signal where h_\times polarization predominates, we have:

$$E_\times > I_\times \quad (2.7)$$

As explained in Section 2.5, X-Pipeline [26] identifies energetic pixels through the application of thresholds, for which the incoherent energy, the total energy and, their plus and cross components, are calculated. A detailed explanation of this method and its derivation can be found in [26][28].

2.3.2 Overview of the spherical radiometer algorithm

X-SphRad is based on a particular algorithm, the spherical radiometer, which distinguishes it from the other pipelines used for the long-burst search. The peculiarity lies in the use of spherical harmonics to calculate the correlation among the data provided by a network of detectors.

The key points of the spherical harmonics approach are here described [27]. The cross-correlation of two data streams is shown in the following equation [15]:

$$\xi_{12}(\hat{s}) = \frac{1}{N} \sum_{j=0}^{N-1} g_1[j; \hat{s}] g_2[j; \hat{s}] = \frac{1}{N} \sum_{q=0}^{N-1} \tilde{g}_1[q; \hat{s}] \tilde{g}_2^*[q; \hat{s}] \quad (2.8)$$

Where g_1 and g_2 are the data streams provided by a pair of detectors, \hat{s} is the signal incident direction and N is the number of samples. Notice that, the notation $[; s]$ means that a time delay has been referred to a reference position. Parseval's theorem has been applied to rewrite the cross-correlation formula in the frequency domain (q).

In [15], ξ has been calculated by a sum over spherical harmonics Y_{lm} up to order l_{max} since cross-correlation is a function of position on a sphere. Equation 2.8 is then written as follows [27]:

$$\xi_{12}(\hat{s}) = \frac{1}{N} \sum_{l=0}^{l_{max}} \sum_{m=-l}^l \sum_q \left[\tilde{g}_1[q] \left(\frac{1}{N} \tilde{T}_q(\vec{r}_1 \cdot \hat{s}) \tilde{T}_q^*(\vec{r}_2 \cdot \hat{s}) \right)^{(lm)} \tilde{g}_2^*[q] \right] Y_{lm}(\hat{s}) \quad (2.9)$$

Here, \vec{r}_1 and \vec{r}_2 are the detectors positions and the notation $Y_{lm}(\hat{s})$ indicates decomposition into the spherical harmonic domain. T and T^* are operators representing the time delay for sky and detector positions. To reduce com-

computational cost we can cut-off the analysis at an arbitrary order l . Edwards [16] points out what we can estimate as:

$$l_{max} \simeq \frac{\pi b f_s}{c} \quad (2.10)$$

where, b is the inter-detector baseline and f_s is the data sampling rate.

2.3.3 Pipeline schema

Figure 2.3 [30] shows the diagram on the pipeline structure. We illustrate key steps carried out by X-SphRad.

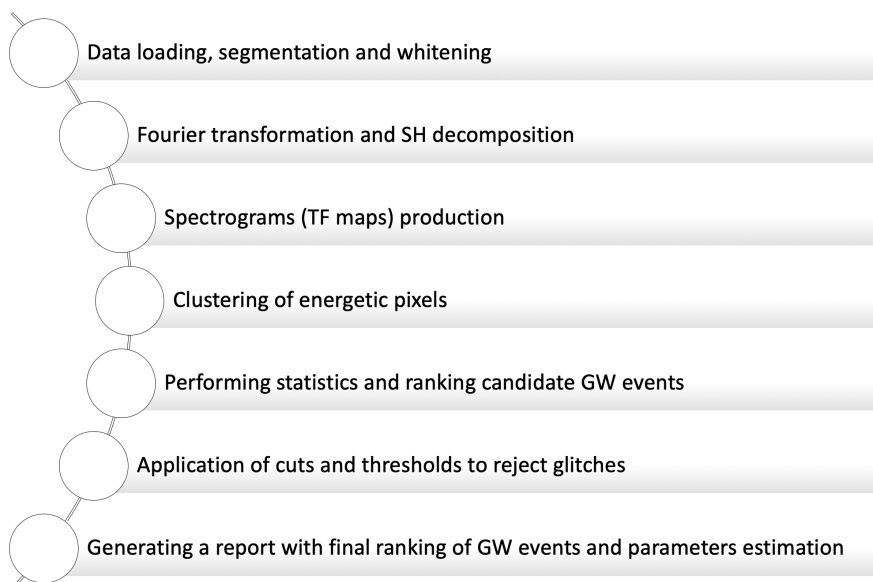


Figure 2.3: X-SphRad flowchart.

2.3.4 Data management and optimisation

Currently, data are divided into blocks of 512 seconds; the duration of the data frame must be enough to contain the duration of the signals while avoiding to reach dimensions that could lead to an increase in glitches. Previous studies show that data analysed in blocks greater than a minute there will have at least one loud glitch [30]. While increasing the block length from

256s (block time used in previous pipeline version) to 512s, reduces signals' tendency to be split between blocks. For each block, a filter is applied to remove persistent line features in the frequency domain. Data are whitened [31, 32] and Fourier transformed to switch from the time domain to the time-frequency domain. To this end, the choice of the TF map resolution is crucial as it can optimize or compromise the SNR (Signal to Noise Ratio). Following the uncertainty principle, the pixel size must be chosen in a balanced way: If it were too small, there would be an increase in noise, if it were too large, image precision and loss of information would be lost. It should be noted that TF maps generated and analysed in this work have a pixel size of 0.5 seconds x 1 Hz.

2.3.5 Time-Frequency maps and Clustering

As for signal duration, the transition from the time domain to the time-frequency domain must be done with due consideration. X-SphRad produces TF maps using the following basis decomposition [30]:

$$\tilde{x}[k] = \sum_{j=0}^{N-1} x[j] \exp \frac{-i2\pi jk}{N} \quad (2.11)$$

where $\tilde{x}[k]$ is the Fourier transform of the time series $x[j]$ for N data points. Note that, at this point of the analysis, we are inside the spherical radiometer engine. Spectrograms (i.e. TF maps) are produced using the expansion of spherical harmonics. Fundamental for time-frequency maps is the correlated power, defined as follows [34]:

$$\zeta = \sum_{pairs, ij} \sum_{l=0}^{lmax} \left| (\xi_{ij})^{l,m=0} \right|^2 \quad (2.12)$$

Considering a ring in the sky of constant delay, the cross-correlation (Equation 2.9) is approximately constant, because it varies with the time-delay between detectors due to their sky position. Thus, in the spherical harmonic domain, we are able to consider just the m=0 only mode for each detector pair, while ignoring the $m > 0$ modes, because m=0 corresponds to the ring

in the sky of constant delay since we have chosen to align the inter-detector baseline with the z-axis. The following equation [34] specifies the energy's value of pixels constituting the TF map:

$$P_{t,f} = \sum_{i,j=0}^d \xi_{ij}^{(lm)} = \sum_{l=0}^{lmax} \sum_{m=-l}^l (c_{lm})^2 \quad (2.13)$$

Where, c_{lm} are the spherical harmonic coefficients. Spherical harmonic coefficients order is explained in Appendix A. Additional details on the production of time-frequency maps can be found in [30]. Once the TF maps are generated, the spherical radiometer engine performs the so-called "next-nearest-neighbors-clustering" [35, 36].

This process, firstly divides a TF map into regions of an equal surface area, identifying the excess power [121] of the constituent pixels. The statistic used for the excess power sums the power of the data in a defined frequency band and time interval. Subsequently, under the hypothesis of stationary and Gaussian noise, the distribution is studied as a χ^2 (non-central χ^2) deviate in the absence (presence) of a signal [121]. The fraction of pixels kept is of 5%. For each region of the map, the necessary condition for clustering is that selected pixels must share at least one edge or corner. Nearby pixels will be grouped to form a cluster. Finally, the pipeline will compile a list of all clusters identified in the entire map, by their total energy.

Glitches, non-Gaussian non-stationary noise anomaly, are a limitation for this clustering method; they can be identified as a candidate events and can be ranked in the clusters list.

2.3.6 Background and Simulated signals

Background estimation is necessary to assess the reliability of our results and even more to know the sensitivity of X-SphRad. The chosen approach is to shift by a non-physical time, called in the jargon "set of lags", the data coming from the singular detectors. In other words, a set of lags means a set of analysis runs performed on data where there is an artificially inserted time shift of one interferometer output with respect to the other, such that any

coincident events cannot physically correspond to gravitational waves. And also, the larger the set of lags, the longer the duration of the background. This type of analysis is known as Off-source.

Note that X-SphRad analyses Off-source segments and On-source segments (actual and unaltered data frames) in the same way. Off-source segments are also necessary for the calculation of the False Alarm Rate (FAR), which determines the significance of the analysis [27][37]. Then, waveforms of various types and different scales are used to establish the detection efficiency of the pipeline, as mentioned in Section 2.1.

A fundamental parameter for each waveform is the injection scale h_{rss} (gravitational amplitude root-sum-square), defined as [30]:

$$h_{rss} = \sqrt{\int_{-\infty}^{+\infty} [h_+^2(t) + h_\times^2(t)] dt} \quad (2.14)$$

h_{rss} is proportional to the inverse of the distance between the source of the simulated signal and the detector. It provides an evaluation of the X-SphRad detection efficiency function of the source distance. X-SphRad produces a detection efficiency curve for each injected waveform selected for the analysis; an example of an injection efficiency curve plot is shown in Figure 2.4. This information provides an upper limit for the detector sensitivity as function of source distance. For an injection to be 'recovered', it needs to have a higher detection statistic than the loudest surviving background event; Which means that the detection efficiency is defined by the fraction of signals, at a fixed distance, that survive all the background rejection cuts and with a ranking statistic dependent on the False Alarm Rate estimated from the background noise. This statistic must be equal to or greater than a value corresponding to the given rate [30].

2.3.7 Vetoes and Tuning

Following the method mentioned in Section 2.3.1, we can now illustrate how X-SphRad applies cuts in the post-processing [38]. This happens once the

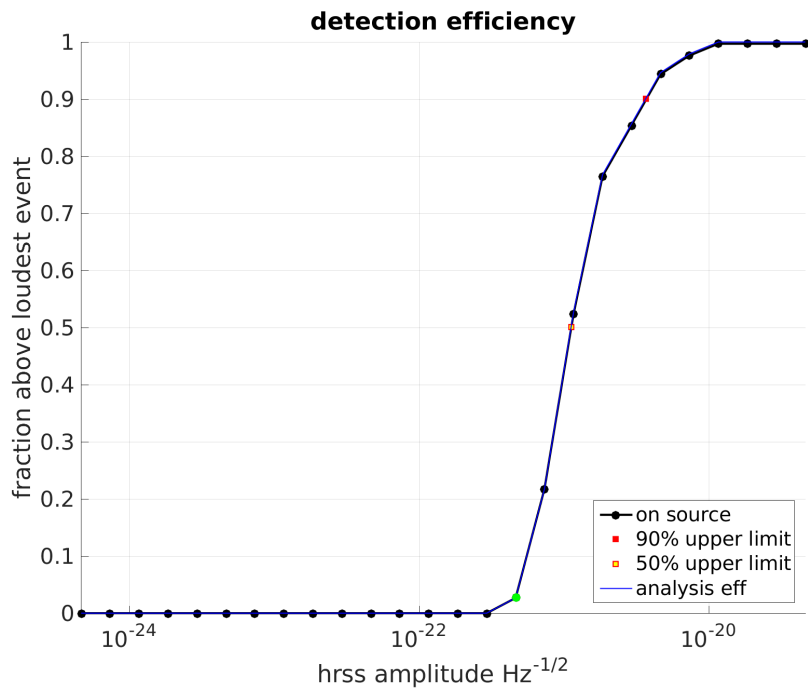


Figure 2.4: Detection efficiency curve of LINE B waveform test. Fraction of injections recovered with significance greater than loudest event in (dummy) on-source. Black dots are sampled values, red and yellow dots are respectively the 90 % and 50 % efficiency obtained from interpolation. Green dots mark sampled values with $0 < \text{efficiency} < 5\%$. The blue curve shows the efficiency when DQ flags are not applied to injections. Image and caption are taken from our webpage to provide results from the analysis made using X-SphRad.

list of candidate events is generated. Formally, the event will pass the cut if:

$$E_{SH} > kI_{SH} \quad (2.15)$$

Where k depends on the automated background tuning¹ [38] and SH subscript stands for Spherical Harmonic decomposition.

This approach is not effective in the presence of low energy events. For this purpose, the so-called "alpha cut" [39][122] is applied. It discriminates the events that survived the first cut through the following condition:

$$\frac{2|E_{SH} - I_{SH}|}{(E_{SH} + I_{SH})^{0.8}} + 1 \geq \alpha \quad (2.16)$$

where α depends on the background tuning.

2.4 Coherent Wave Burst (cWB) pipeline

cWB pipeline [40, 41] is a C++/ROOT [42] based pipeline for long and short transient gravitational-wave signal searches. Exactly like X-SphRad, cWB makes minimal priori assumptions about the expected signal. Its algorithm identifies coincident events within the data from the detectors in the network and then reconstructs the associated gravitational wave signal.

There are three fundamental steps of the analysis carried out by cWB: "data conditioning", thanks to which predictable noise components are removed, "Construction of Time-Frequency clusters", a crucial step for the identification of the most energetic clusters, and "Generation of coherent triggers", during which cWB applies the "maximum-likelihood" approach. Details about the formalism of this approach can be found in [48]. A schematic representation of the multi-stage analysis is shown in Figure 2.5. We describe the main features of each stage mentioned above.

¹The software tests many values for the threshold, and optimises the amount of simulation recovered versus the amount of background noise.

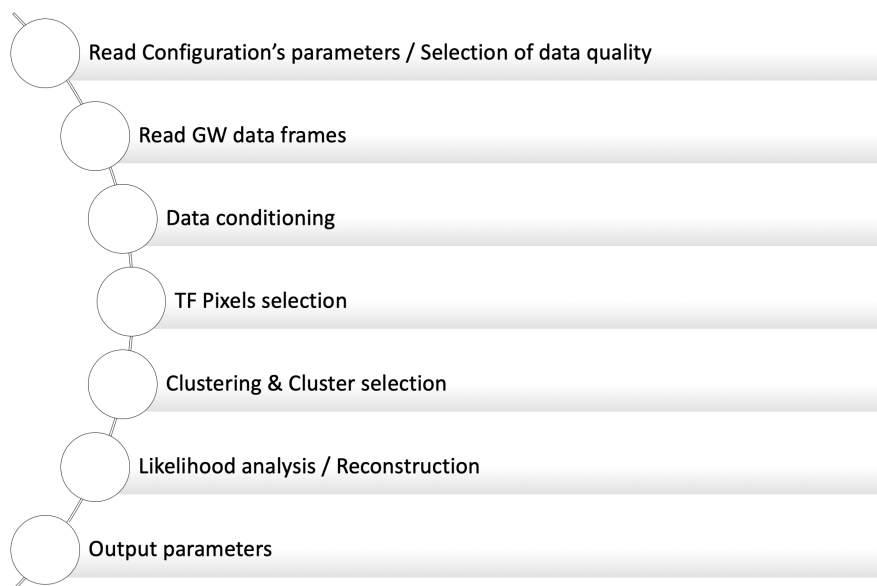


Figure 2.5: Main steps of cWB pipeline.

2.4.1 Data conditioning

The basis of the cWB data conditioning is the “Regression” algorithm [43], which identifies and removes predictable noise sources. These predictable components correspond to spectral lines of the power spectrum density (PSD) of the detector (Figure 2.6). Filters are applied in the wavelet domain at various wavelet layers² [44].

2.4.2 Time-Frequency clusters

cWB pipeline decomposes data streams coming from each detector in the network at different resolution levels (dt , df) to generate clusters of pixels on the time-frequency (TF) map. This decomposition is possible using a linear combination of wavelet functions [46]. Figure 2.7 shows how different resolutions in time and frequency allow different representations and characterizations of a signal.

The cWB pipeline performs the multi-resolution analysis (MRA) once the time-frequency maps are generated. For each selected level, cWB classifies

²The layers are different signal decomposition levels given by the wavelet

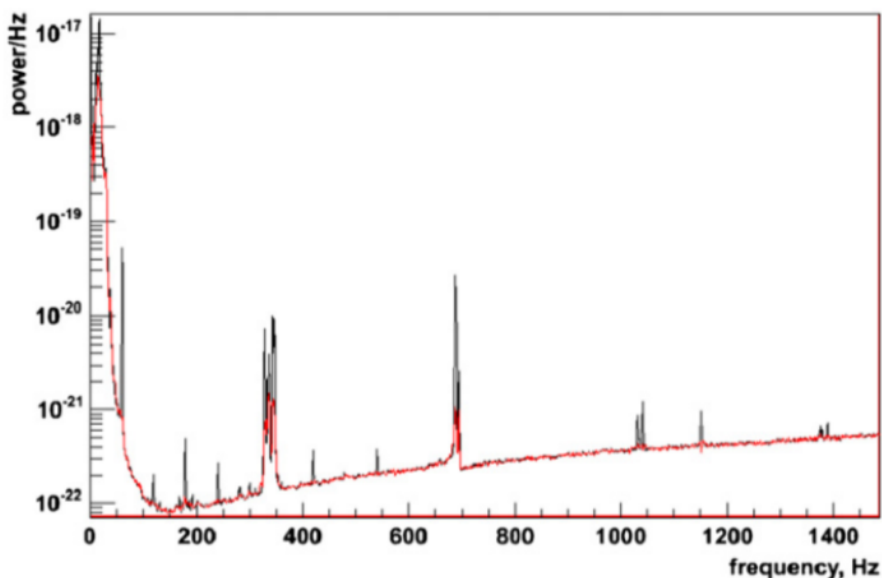


Figure 2.6: The black line is the Hanford detector’s power spectra of noise. The red line is the same spectra of noise after the application of a filter [48].

TF pixels in two categories: the black, and the white pixels. The determining factor for this first selection is the energy corresponding to each pixel. Black pixels are those with corresponding energy above a threshold, which depends on the noise level. White pixels have energy below that threshold. Selected pixels constitute the core (black pixels) and halo (white pixels) of a cluster, and together they are considered a trigger at a specific time-frequency resolution (Figure 2.8). Notice that, ‘White pixels’ in Figure 2.8 have a grey colour just to mark ‘white pixels’ close to core edge.

2.4.3 Coherent triggers selection

At this stage of the analysis, there is the selection of coherent triggers. In this regard, the cWB pipeline applies the likelihood calculation to the super-clusters³[47]. Once triggers have been selected, cWB reconstructs GW event parameters related to each trigger. Among these are source coordinates, detector responses, and maximum-likelihood statistics [48]. The latter is alone

³Combined-clusters belonging to different decomposition levels

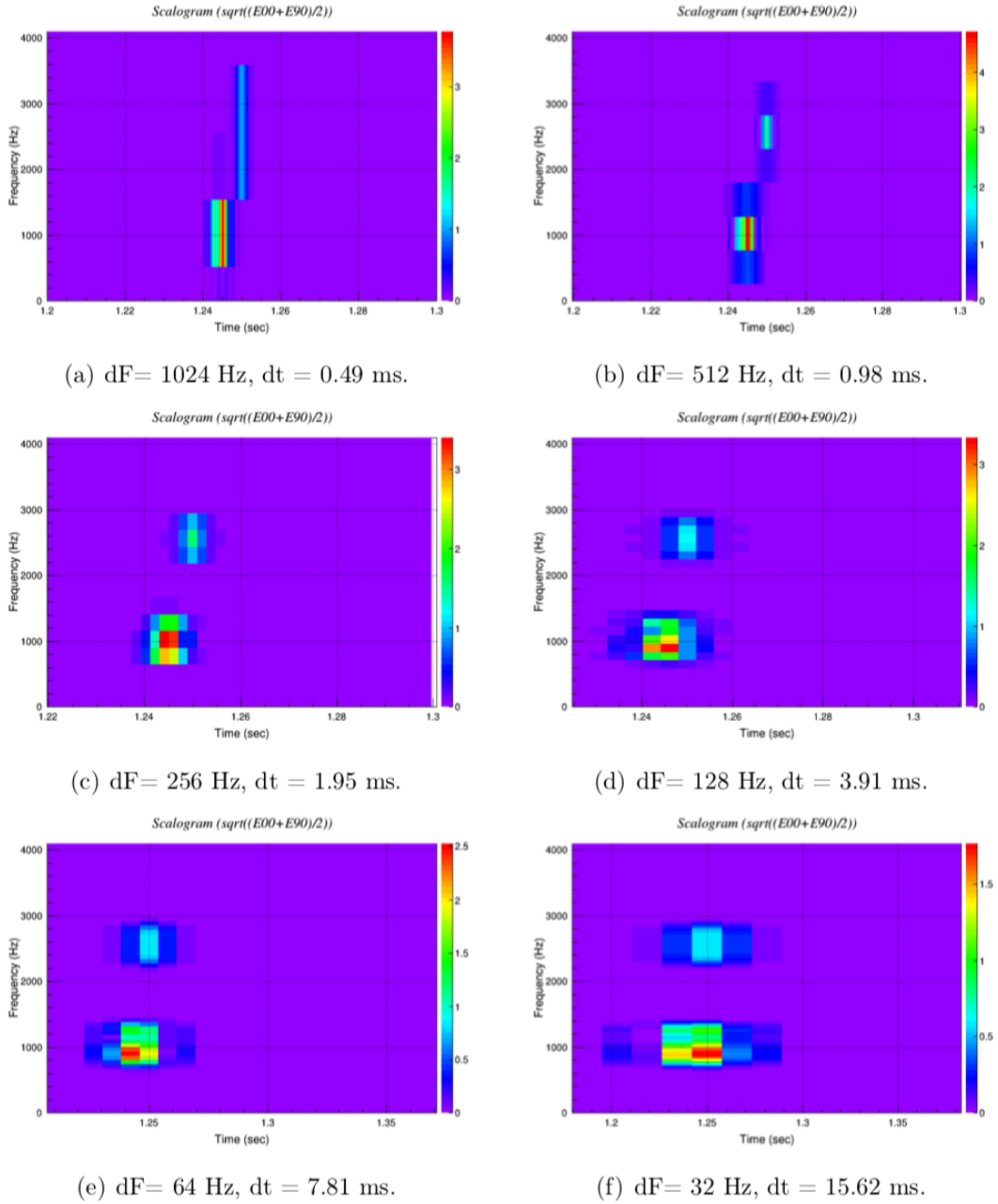


Figure 2.7: Example of different time-frequency resolution signal reconstructions with cWB using a simulated signal [48].

sufficient to control the false alarm probability in the ideal case of Gaussian and stationary detector noise. In reality, we need to apply additional cuts to

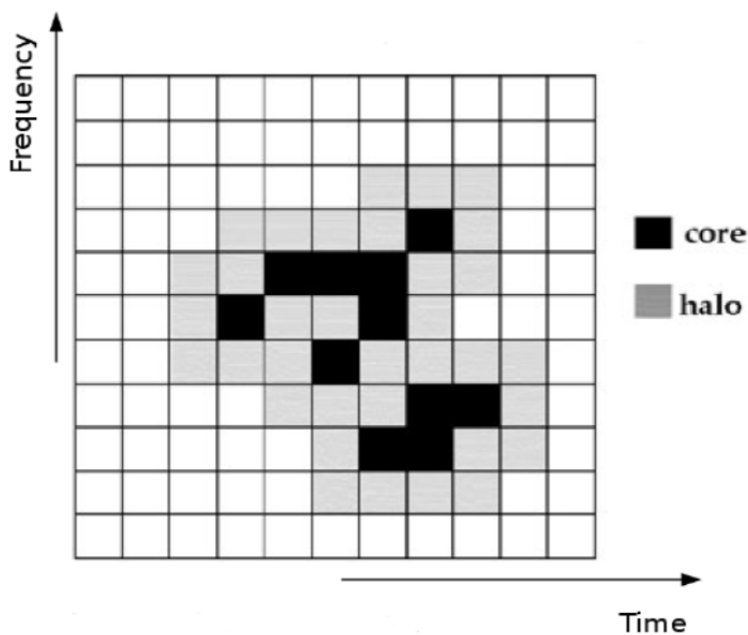


Figure 2.8: Example of cWB TF cluster : the core (black pixels) and the halo (grey pixels) [48].

minimize environmental and instrumental noise that can easily mimic a GW event. It is, in fact, the threshold on maximum-likelihood statistics (L_{max}) that controls the pipeline false alarm and false dismissal probabilities. L_{max} is then related with the 'Network correlation coefficient' net_{CC} , with which cWB discriminates GW signal from noise. $net_{CC} = \frac{E_c}{|E_c| + E_n}$, where E_c is the coherent energy detected by the network and E_n is the energy of residual noise after subtraction of signal energy from the total one.

A full description of the cWB pipeline approach to discard false alarms can be found in [45, 47].

2.5 X-SphRad and cWB: a comparison on the O2 data

If we detect a GW signal, the results of one pipeline will be used to validate the results of the other. Understanding differences and similarities among pipelines is an essential effort at a LIGO collaboration level. In this section, we present a comparative analysis of X-SphRad and cWB. The last month of the O2 run has been analysed using a two-detector network (LH), and eight simulated waveforms (astrophysical and ad-hoc) to perform simulations have been reconstructed by both pipelines, i.e. software injections. Results are presented in subsection 2.5.3.

2.5.1 Data Quality

All pipelines must minimize the impact of including poor quality data within their analysis. CATs are different categories of poor quality data, divided into CAT0, needed to select periods in science mode (i.e. when detectors are operating). CAT1 includes discarded segments in which noise can contaminate the whitening procedure. CAT2 takes into account the excesses of noise between auxiliary channels and the output detector. CAT3 considers times where there is a statistical correlation, but the relation with auxiliary channels is not clear. Also, it takes into account settings of a specific search, such as the long-duration burst searches. Finally, CAT4 needs to discard periods in which hardware injections, simulated gravitational-wave signals added to the Laser Interferometer Gravitational-wave Observatory, have been performed. More information on O2 Data Quality can be found in [51][40].

2.5.2 Analysis Parameters

We analysed data given by LIGO detectors from the Hanford and Livingston sites, from Jul 25, 2017, 00:00:00 UTC to Aug 25, 2017, 00:00:00 UTC,

corresponding to 20 days of coincident data⁴. Figure 2.9 shows the LIGO observing time for the O2 run [50]. It is a two-detector network analysis, with a background of ten years for X-SphRad and twenty-five years for cWB. The frequency range is [24,2000]Hz, with a sampling frequency of 4096 Hz. The segment length is 512s for X-SphRad and 1200s for cWB. We injected into both pipelines eight waveforms among astrophysical and ad-hoc types: ADI, LINE, MAGNETAR, QUAD and WNB. Figure 2.10 provides the duration and frequency range of the analysed waveforms. Details about waveform morphology can be found at [49].

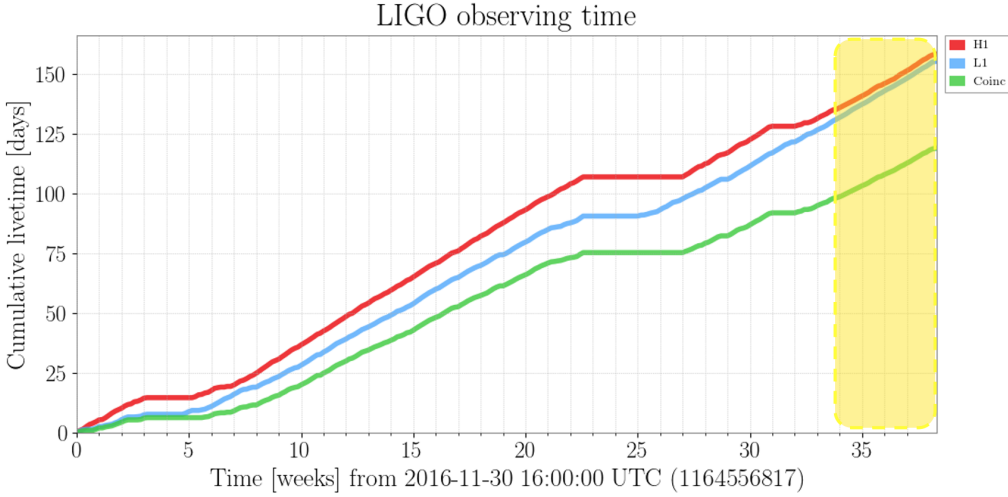


Figure 2.9: LIGO observing time for the O2 scientific run. The yellow box highlights the coincident time analysed in this work [53].

2.5.3 Results

We present the results obtained from the comparative analysis between X-SphRad and cWB. Eight simulated waveforms are reconstructed by both pipelines to compare their detection efficiency (see Section 2.3.6). Both X-SphRad and cWB injected the same waveforms at different scales and, the FAR used for the comparison was of 1/10 years for both pipelines. It is

⁴A condition for which detectors are locked and recording in science mode simultaneously.

Waveform	Duration (s)	Frequency Range (Hz)
ADI B	9	110-209
WNB A	20	50-400
QUAD A	30	50-200
ADI A	39	135-166
WNB B	60	300-350
ADI E	76	111-260
LINE B	100	700-900
MAGNETAR G	400	400-490

Figure 2.10: Duration and frequency range for each analysed waveform. Waveforms are selected among astrophysical and ad-hoc families.

done to assess the probability of detection as a function of the energy of gravitational waves. At the end of each analysis, both pipelines provided the values of the signal amplitude, $hrss$, (see Equation 2.14) corresponding to the signal detection probability of 50% and 90% respectively.

Figure 2.11 and 2.12 show an example of the detection efficiency plots produced by X-SphRad and cWB, respectively. All X-SphRad and cWB detection efficiency curves, obtained by performing this analysis, can be found in Appendix B. We compare the $hrss$ values with a detection efficiency of 50% in Figure 2.13, and the $hrss$ values with a detection efficiency of 90% in Figure 2.14. We stress again that $hrss$ is the signal amplitude. It means that, the smaller its value the better the detection efficiency will be.

We focus on the 50% results to evaluate which pipeline has a better detection efficiency for each injected waveform. For the period analysed in this work, it is clear that X-SphRad has better detection efficiency for waveforms of type ADI_E, QUAD_A and MAGNETAR_G. In contrast to other waveforms, where cWB is more sensitive. X-SphRad and cWB have similar detection efficiency for the ADI_A waveform.

Through appropriate conversions [40], we extrapolate the effective detec-

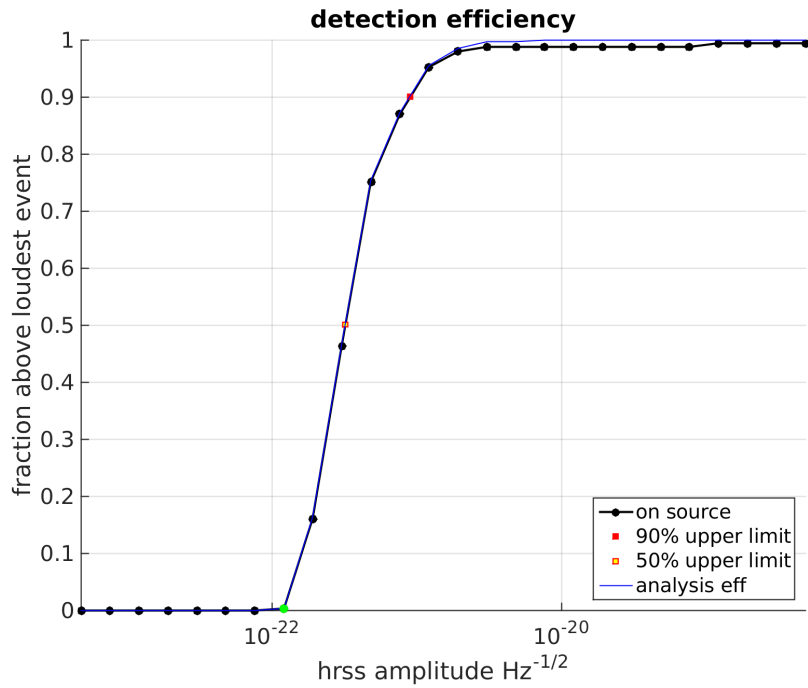


Figure 2.11: Detection efficiency curve of an ADI A waveform test. Fraction of injections recovered with significance greater than loudest event in (dummy) on-source. Black dots are sampled values, red and yellow dots are respectively the 90 % and 50 % efficiency obtained from interpolation. Green dots mark sampled values with $0 < \text{efficiency} < 5\%$. The blue curve shows the efficiency when DQ flags are not applied to injections. Image and caption are taken from our webpage to provide results from the analysis made using X-SphRad.

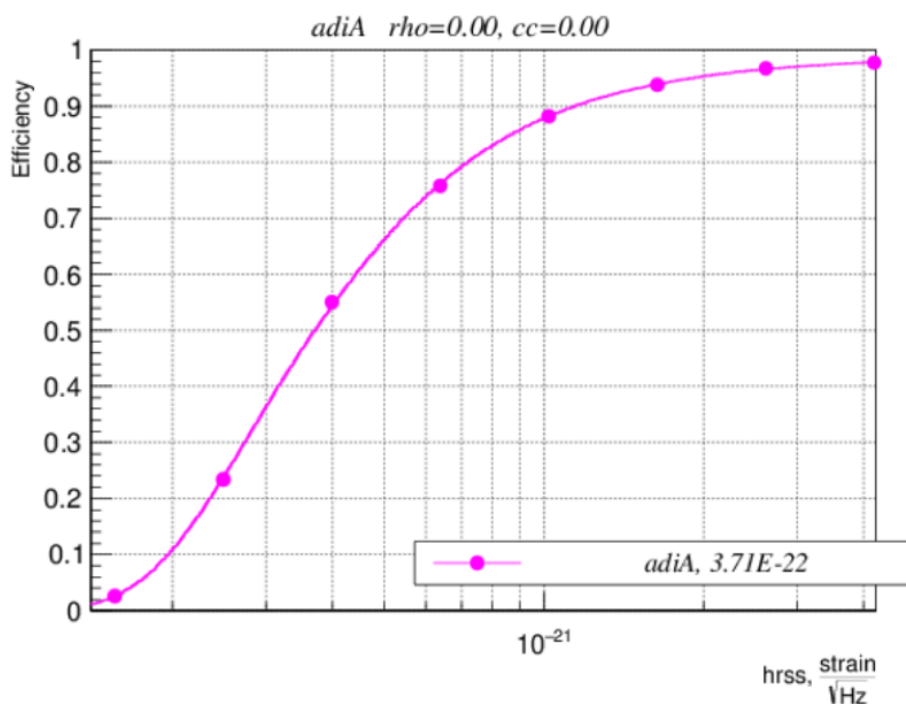


Figure 2.12: Example of a detection efficiency plot of an ADI A waveform injected into cWB. The caption reports the value of the hrss value for a detection probability of the 50 %. $3.71e^{-22}$ value displayed in the capture corresponds to the hrss value.

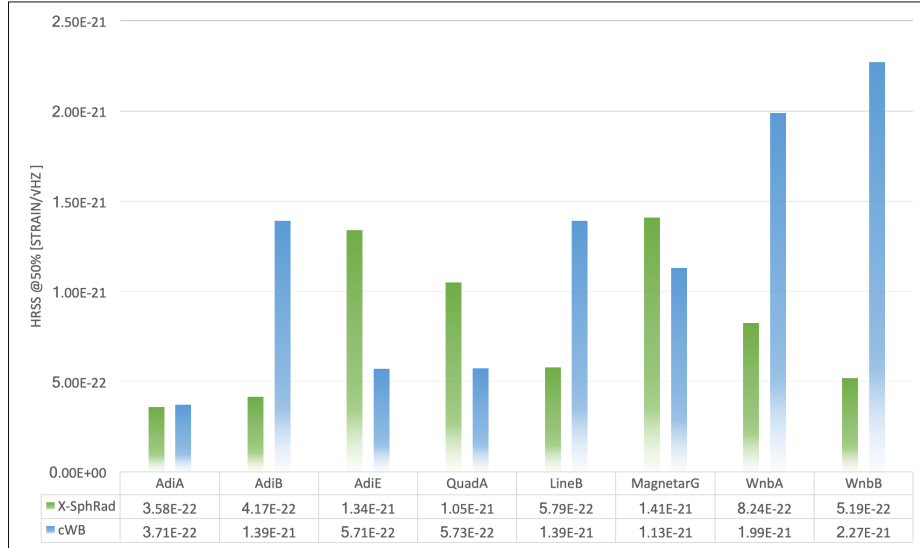


Figure 2.13: HrSS values, corresponding to the 50 % detection probability, produced by X-SphRad and cWB for eight waveforms. The smaller hrss value the better the detection efficiency will be.

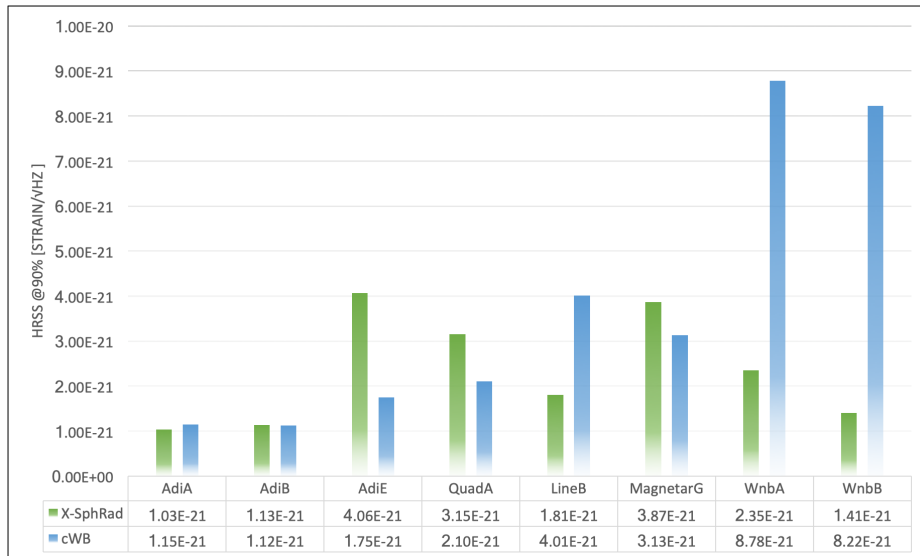


Figure 2.14: HrSS values, corresponding to the 90 % detection probability, produced by X-SphRad and cWB for eight injected waveforms. The smaller hrss value the better the detection efficiency will be.

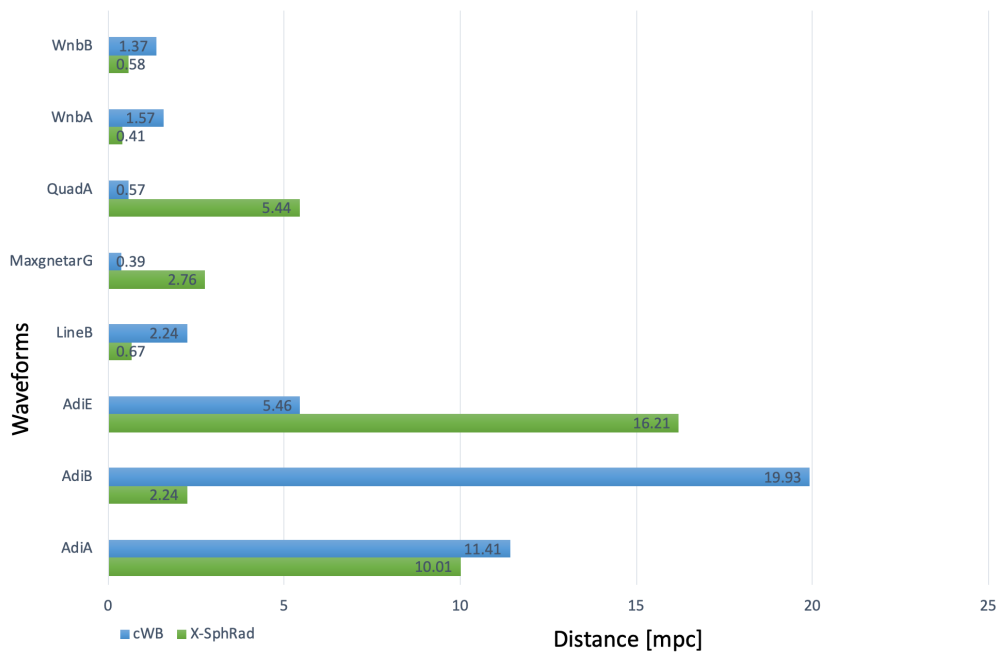


Figure 2.15: Effective distance reached by X-SphRad and cWB for each analysed waveform, with the 50 % detection probability.

tion distances. These distances represent the maximum distance at which the pipeline can detect this signal 50% of the time (i.e. hrss at 50%). This last information is crucial for evaluating the performance of a pipeline. Figure 2.15 shows a comparison between the effective distance reached by X-SphRad and cWB.

Finally, we can conclude that X-SphRad and cWB have different performances depending on the family of the injected waveforms. Since no dependency on a specific waveform feature has been found, this leads us to think that it would make no sense to limit the search to waveforms with precise characteristics. Rather, we can work on improving pipelines capability in noise identification and rejection. The more noise we reject, the better our performance will be.

In the next chapter, we describe and discuss a noise rejection method that could enhance pipeline performance and therefore their detection efficiency.

Chapter 3

SHaVeD: Spherical Harmonic Veto Definer

X-SphRad performs an all-sky search, but glitches [38] make this search harder because their presence compromises the pipeline’s efficiency. Due to a lack of a robust method for identifying glitches, we evaluated and implemented a tool for noise rejection. In particular, X-SphRad would benefit from a method where glitches are identified and discarded in the ‘pre-processing’, before doing the full analysis. Previous studies [38] show the potential of the Spherical Harmonics (SH) coefficients in discriminating glitches [53] from signals. X-SphRad uses spherical harmonics as a glitch rejection statistic already. Glitches are hindering the search at the selection step of potential candidate events; they are impacting the search before the pipeline performs the rejection/coherent tests. Therefore moving the glitch “identification and rejection” step earlier might improve the search. This rejection method aims to identify the GPS times corresponding with glitches present in data. In this section, we describe the main steps that led to the creation of SHaVeD.

3.1 Description of the method

Previous research [38] shows that glitch power mainly appears in the C_{00} component of the SH decomposition. C_{00} corresponds to the energy average

over the whole sphere, while the signal power will be present in most of the coefficients (C_{lm}). In other words, spherical harmonic decomposition is equivalent to a sky-walk where we account for the delay in detector arrival time of the signal. Glitches do not come from a particular position in the sky and so do not have a preferred delay, so they appear mainly in the $l=0$.

Figure 3.1 shows an example of short duration wide band glitch present in data. Figure 3.2 shows an example of short-duration GW alongside a short duration wide band glitch. Both time-frequency (TF) and time-spherical harmonic (TSH) maps are shown.

Starting from the above considerations, we use glitch preferences of localizing in the C_{00} of the TSH domain. We begin by launching the data analysis with X-SphRad. Values of C_{00} and C_{lm} of each frame (data segment) are saved.¹ The sum of $C_{lm} > C_{00}$ is then calculated on each time bin of the frame. We define C_{lm} as $C_{lm} = \sum_{l=1}^{l_{max}} \sum_{m=-l}^l |c_{lm}|$ (see Equation 2.13 and Appendix A). In this way, we have a value of C_{00} and a cumulative value C_{lm} for each bin of each data frame. Figure 3.3 shows a time-frequency map, a time-harmonic map and the corresponding skymap for a segment containing a glitch and an injection; a set of coefficients tell us something about the distribution of power over the sky for that time.

At this point, the ratio between C_{lm} and C_{00} is computed as $\mathcal{R} = \frac{C_{lm}}{C_{00}}$. In other words, \mathcal{R} is a function representing the ratio $\frac{C_{lm}}{C_{00}}$ over time. Since glitches are mainly localized in C_{00} , the function \mathcal{R} will have minimum points corresponding to the presence of glitches in the TF map.

Notice that, the goal of a veto is removing the highest possible amount of noise while discarding the least possible time. That is why, a threshold on \mathcal{R} is calculated to cut off the least possible contribution from the TF map. The threshold is obtained using a standard deviation distribution: the user performing the analysis can choose the percentage to discard. In this work, we considered three values: 5%, 2.5%, and 1%.

¹The number of C_{lm} present in each frame depends on the maximum degree value (l_{max}) set by the user.

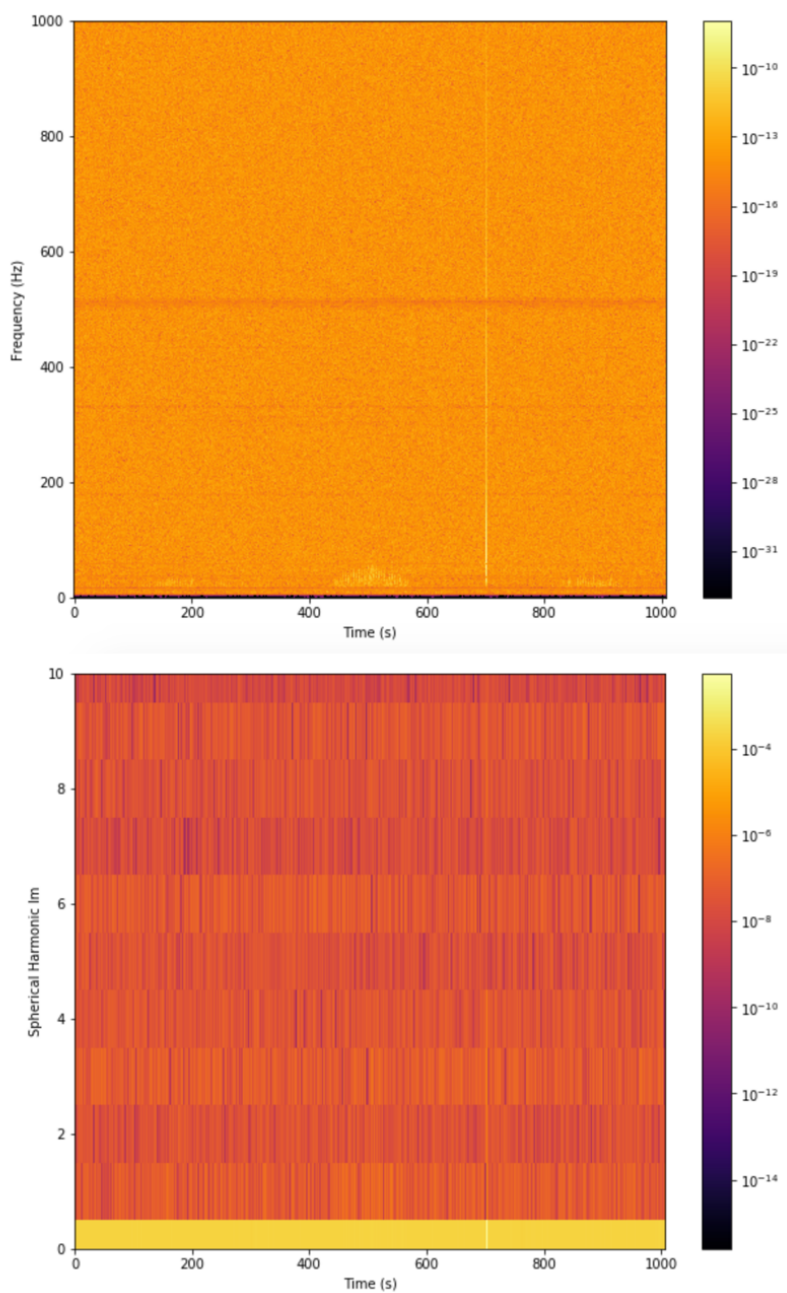


Figure 3.1: A dual-representation of the same data-frame. Frequency-time (TF) map top: A glitch can be clearly seen at about 700s. Spherical-harmonic-time (TSH) bottom: A glitch can be seen at about 700s just in the C_{00} component (light yellow line).

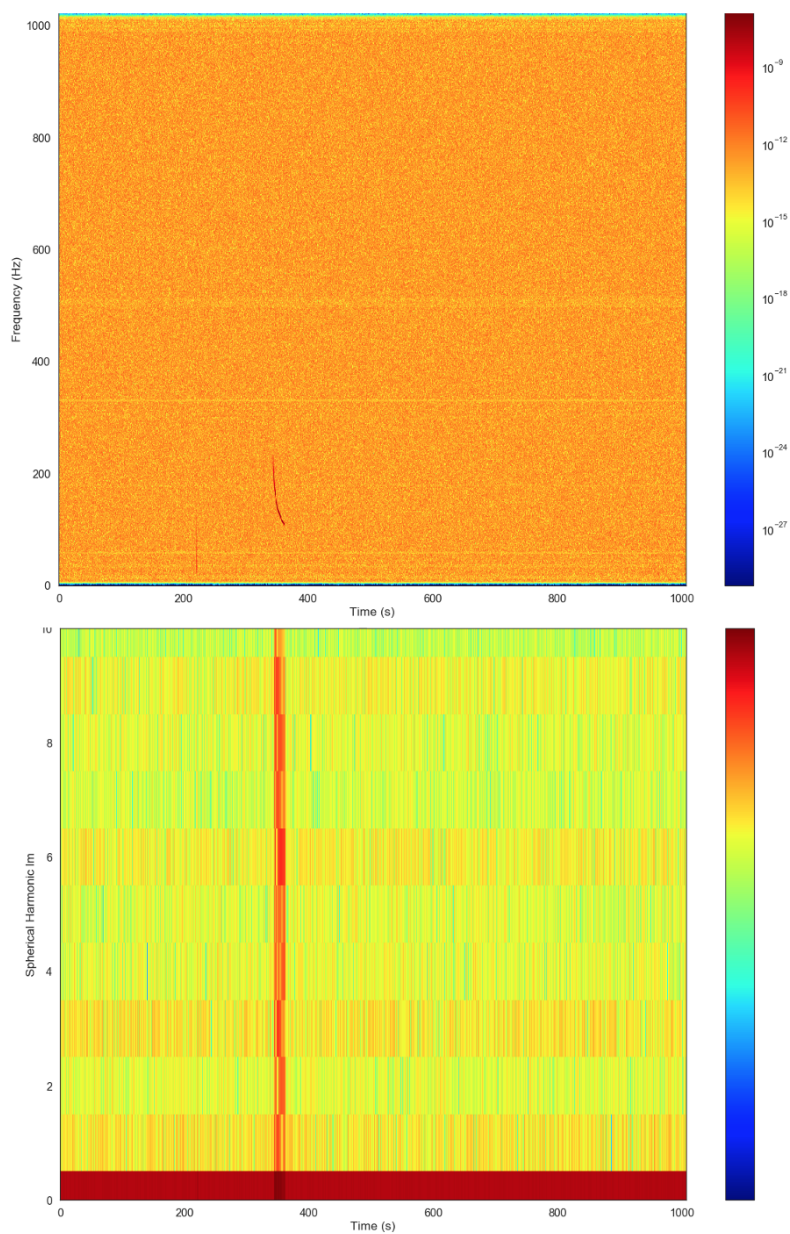


Figure 3.2: A dual-representation of the same data-frame. Frequency-time (TF) map top: A glitch can be seen at about 210s alongside an injection at about 380s. Spherical-harmonic-time (TSH) bottom: A glitch can be seen at about 210s just in the C_{00} component, while the injection can be seen spread on all coefficients.

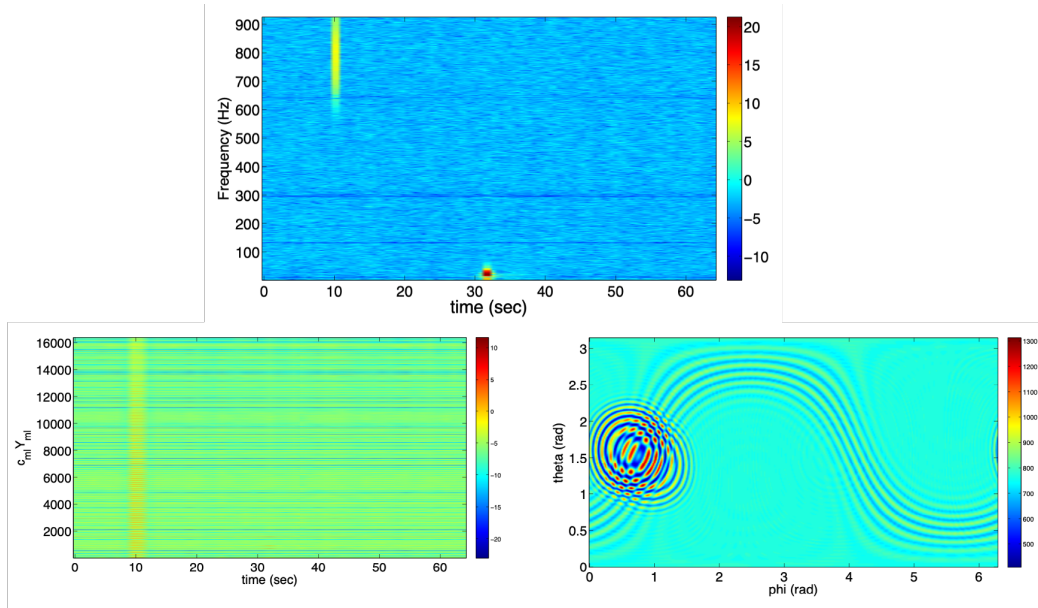


Figure 3.3: Top: A time-frequency map of whitened data; to the upper left we see a short-duration white noise burst (WNB) signal, to the lower middle a glitch. Bottom Left: Time-harmonic map for a segment containing a glitch and an injection. Only the injection is visible (the vertical line at 10s). Bottom Right: Skymap of the coefficients corresponding to the time bin containing the injection, see Figure 3 at 10s.[32]

Figure 3.4 shows an example of \mathcal{R} as a function of time and the relative threshold. Figure 3.5 shows the distribution of the ratio in Figure 3.4. The

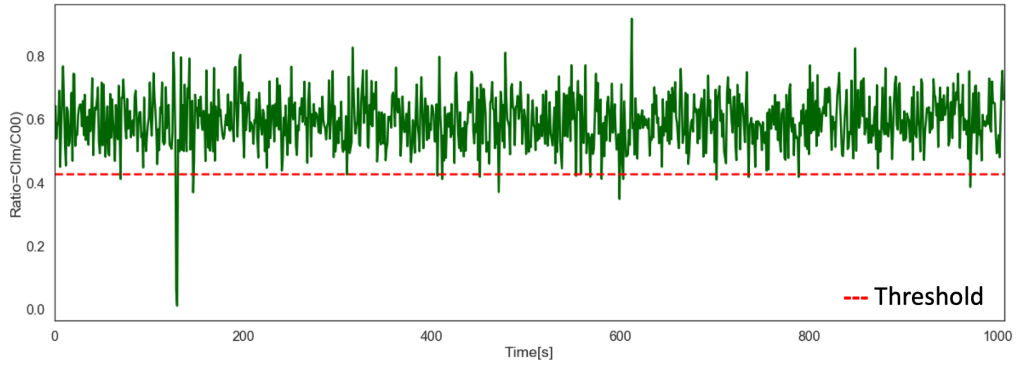


Figure 3.4: Example of the ratios between C_{lm} and C_{00} of a data frame with a threshold fixed at 1 %. The dashed red line is the threshold obtained by using the standard deviation distribution of ratios values.

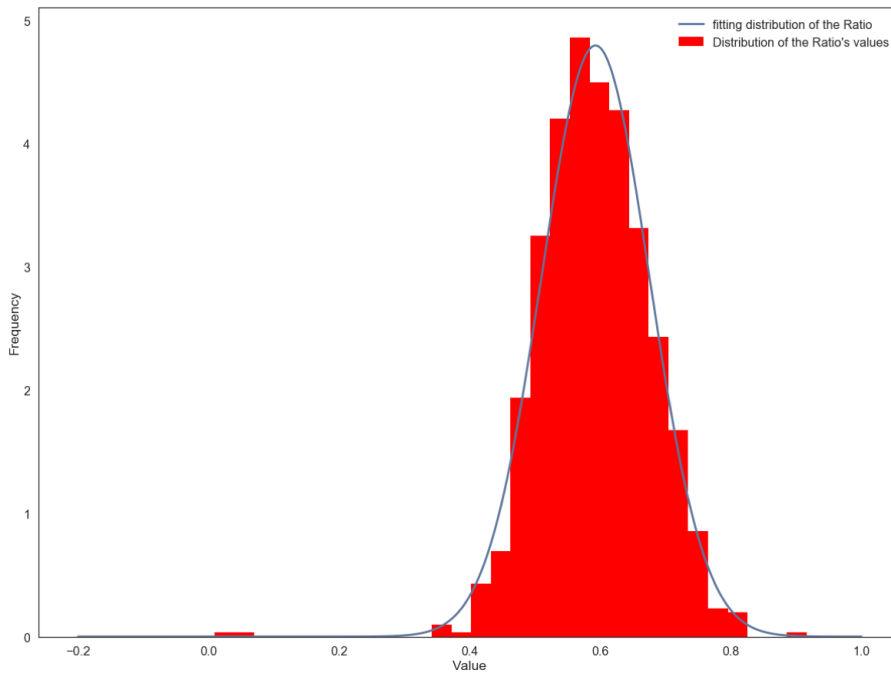


Figure 3.5: Distribution and Gaussian fit of ratios values.

ratio function, \mathcal{R} , has minimum points corresponding to the presence of

glitches in the TF map (Figure 3.6). These minimum peaks also correspond to certain GPS times. In other words, we save the GPS times corresponding to the TF map bins, which value of the ratio goes below the fixed threshold.

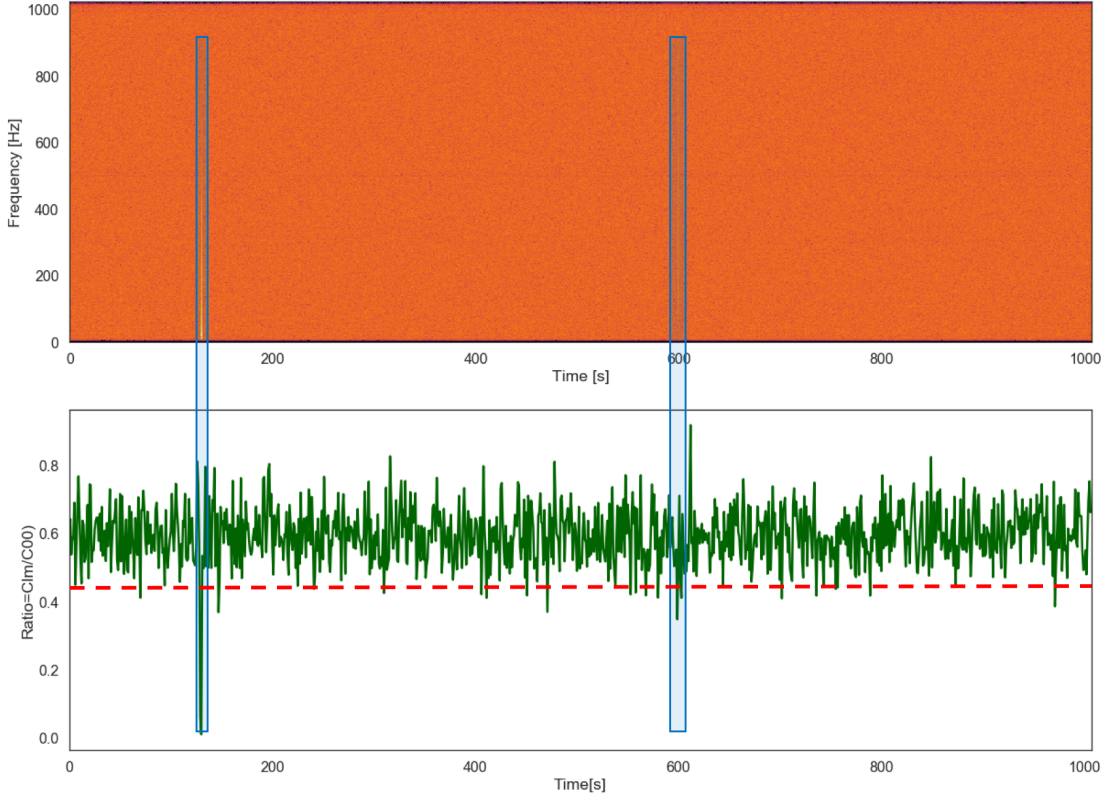
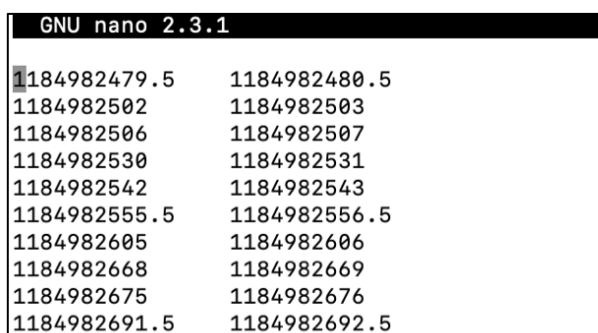


Figure 3.6: Blue boxes highlight where glitches in the TF domain (top plot) match minimum peaks of the ratio function (bottom plot).

With this information, we construct SHaVeD. It is a Matlab script (see Appendix C) that follows the method explained in Section 3.1. Firstly, it loads the spherical harmonic coefficients computed by X-SphRad. With this information, it computes the ratio \mathcal{R} . As explained above, using the distribution, SHaVeD computes a threshold to apply. Then, it takes all the \mathcal{R} elements that fall below that threshold and saves their corresponding GPS times. At this point, the script creates the cut: it considers each GPS time as a central time, and then, it creates a cut of 1 second around it. SHaVeD now saves this information in a two-columns file where the first column is the

GPS starting time of the cut, in the second the final time. This file is the veto file we include in our tests. Figure 3.7 shows an example of this output. Note that in SHaVeD the overlapping cuts are merged into one.

Recall that, SHaVeD is the result of this research aimed at improving the performance of X-SphRad using the coefficients of the spherical harmonics produced by the pipeline during the first stages of the analysis. cWB was the means to test its quality and evaluate its efficiency. In the next Section we discuss the application of SHaVeD into the cWB pipeline.



GNU nano 2.3.1	
1184982479.5	1184982480.5
1184982502	1184982503
1184982506	1184982507
1184982530	1184982531
1184982542	1184982543
1184982555.5	1184982556.5
1184982605	1184982606
1184982668	1184982669
1184982675	1184982676
1184982691.5	1184982692.5

Figure 3.7: File of rejected time segments generated by SHaVeD. The two columns denote the GPS seconds between the start and end of the segment to be excluded from the analysis.

3.2 Application and analysis of O2 data using cWB

To test the performance of the method described in Section 3.1, SHaVeD was applied, with different configurations, in O2 data analysis with cWB. In particular, we distinguish the analyses made with SHaVeD applied in pre-production (before selecting pixels to be analysed as possible candidates event) and in post-production, and with different threshold choices.

In this work, we use the “rate vs ρ ” plots to evaluate cWB’s performance. Rate is defined as the fraction N/T [Hz], where N is the number of triggers within a set of lags (see 2.3.6) with live time T [s]. ρ is the ‘effective correlate’

signal to noise ratio (SNR) defined as:

$$\rho = \sqrt{\frac{E_c}{K} \text{netCC}} \quad (3.1)$$

where E_c is the coherent energy, K is the number of detectors and netCC is a coefficient related to the network correlation. All details about these parameters can be found in [54]. In the next sections, we describe results obtained from different analysis.

Finally, it is necessary to specify that we set different background size. Specifically, we started with a 485-year background for the pre-production analysis (see 3.2.2) and then lowered to 130-year background for the post-production analysis (see 3.2.3). This choice was due to the need to reduce the computational cost and it does not have a significant impact in evaluating SHaVeD's performance at the current status of the project.

3.2.1 Threshold choice

The threshold choice is directly correlated with the discarded percentage in our TF map. Remember that the threshold chosen will determine the number of seconds not analysed.

The more we cut, the more glitches are discarded. However, a more stringent cut will also reduce the fraction of real time for which the network is live and sensitive to real gravitational wave signals.

So the threshold should be carefully chosen balancing these two effects. First, we studied the results obtained by choosing three different thresholds: 5%, 2.5%, and 1%. Data analysed here are the same in section 2.5: 20 days (480 hours) of coincident data. The 1%, 2.5% and 5% thresholds produce SHaVeD files which vetoed 7.23 hours, 17.8 hours and 42.45 hours respectively². It means that, compared to the 480 hours [40] of coincident

²The threshold value is calculated using the 'standard score', known as z-score, of the standard normal distribution: by choosing to cut the 1% from the R's distribution, we are "saving" data that has a cumulative probability of the 99% to stay above that threshold value. For this reason, a 1% threshold will not necessarily correspond to the 1% of time discarded by the veto.

data, SHaVeD cuts off the 1.5%, 3.7% and 8% respectively of coincident time associated with short duration wide band glitches.

Figure 3.8 shows the three thresholds by comparison. We recall that the

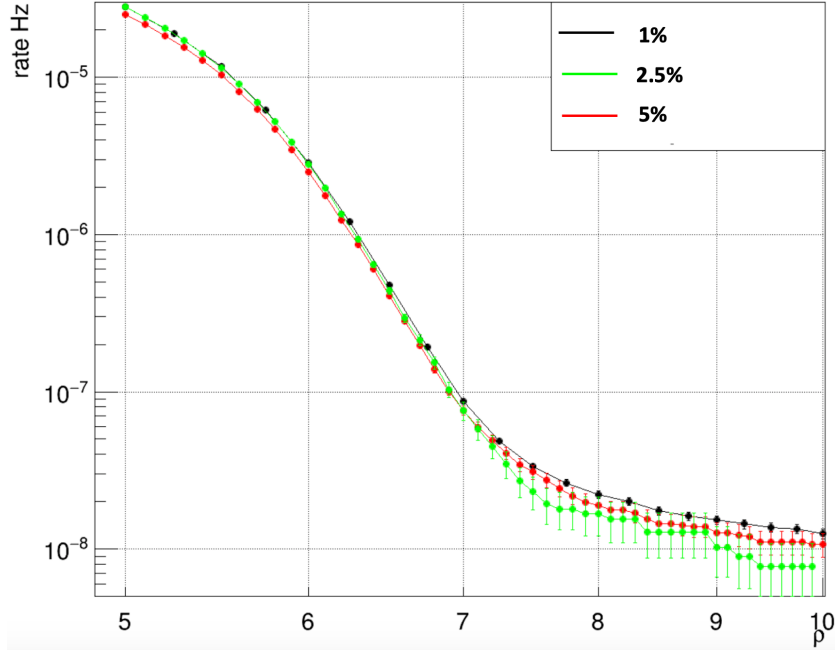


Figure 3.8: Cumulative curve of rate vs ρ of three analysis made with threshold on the C_{lm}/C_{00} ratio of 5 %, 2.5 %, and 1 %.

purpose of the method is removing the most possible amount of noise while discarding the smallest possible fraction of the data. Since Figure 3.8 shows how the three curves (i.e. three thresholds) have the same trend and they are comparable within the error bars, the threshold choice fell on the 1% cut to discard only a further 1.5% from the 20 days of analysed data. We note that for ρ greater than 7, the 5% cut removes fewer glitches than 2.5% cut. We would like to clarify that this behavior is justified by the fact that each analysis is independent from the others and therefore the events detected by each analysis are unique and not included in the previous one. however, most of the glitches identified in the three analysis are the same but with different SNRs.

3.2.2 SHaVeD in pre-production

We report in this section the comparison between the cWB gating [43] and SHaVeD, applying alternatively one of the two in the pre-production stage.

Like the SHaVeD cut, the cWB gating plugin [43] is a pre-production analysis step, consisting of a set of cuts designed to eliminate close vicinities of loud interferometer glitches, so that the very loud events they result in do not reduce the limit-generating power of the analysis.

This plugin is used to exclude from the analysis the pixels in a time interval where there is a huge glitch. For each time slice we compute the sum of the pixel energy over all frequency layers. All pixels in the layers which time slice is marked as cutted are filled with a negative energy. These pixels do not participate to the computation of the pixel's selection threshold [40].

Applying SHaVeD in pre-production means adding a set of GPS times that will be cut out of the analysis before pixels selection (see section 2.4.2).

In addition to the CATs supplied and described in section 2.5.1, the cWB pipeline includes the gating in pre-production. It is done to cut portions of data in which very loud glitches are detected, which would compromise the final result of the whole analysis.

This section looks at what happens to the analysis if we include SHaVeD in pre-production, excluding cWB gating, meaning that we have not carried out the cWB gating routine, but have used SHaVeD as a replacement. We use also for this test the same 20 days of coincidence data considered in the previous sections. We did this test by compute the threshold as 1% of 485 years. Figure 3.9 shows the direct comparison of the same analysis performed with the cWB gating and with SHaVeD, respectively. Figure 3.9 reveals that SHaVeD matches the gating until ρ (see Equation 3.1) is about 7. Beyond that value SHaVeD works well even if the gating has a preferable rate. We can say that SHaVeD presents useful aspects. It seems to be effective at reducing the rate of loud glitches (at large ρ). Since the loudest glitches set the level at which we can make a limit in a loudest event analysis, we finish up with a better limit.

Everything depends on the type of analysis we conduct. Firstly, we know

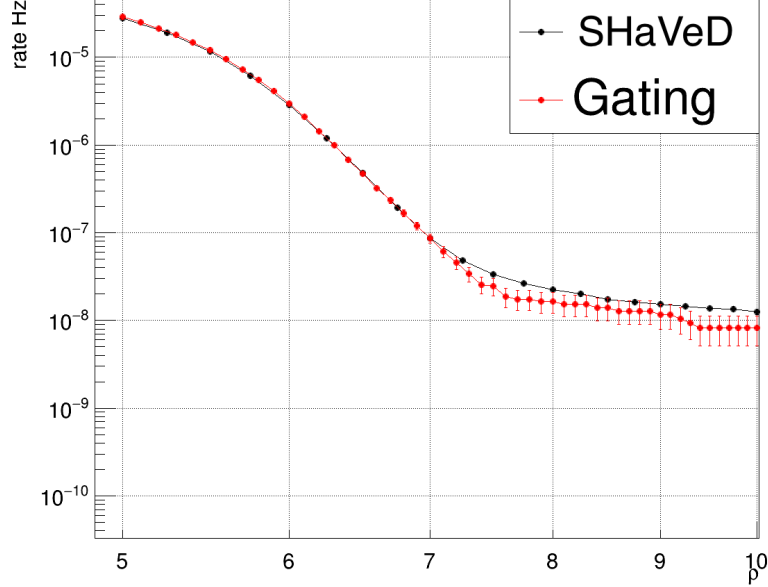


Figure 3.9: Cumulative curve of rate vs ρ obtained using the Gating and SHaVeD. Both curves have the same trend and for various ρ values they are comparable within the error bars.

that for this specific analysis, the gating cuts out almost 5 minutes of data, while SHaVeD 7 hours. Even if the gating plugin is less harmful in terms of information loss, SHaVeD achieves a worthy outcome: it rejects 7 hours of a 20 day run, which is about 1.5% of the data. The existing cWB pre-production gating only rejects 0.02%. On the other hand, our rejection results in a lower threshold (how much lower depends on which run), with only a very small reduction in percentage up-time, 2%. It is still a significant difference, but it depends on the target of our research.

First, we keep in mind that gating is a veto used exclusively by cWB. So for X-SphRad, it is expected that the autonomous generation of an efficient veto file such as the cWB gating, albeit with a more extensive cut, would lead to an improvement in its performance.

We next tested the case when SHaVeD is applied together with cWB gating. We have done this to understand if SHaVeD could bring benefits to

pipelines like cWB that use the gating veto. The comparison (Figure 3.10) shows how SHaVeD can improve the analysis up to ρ of about 5.5, while it has a trend comparable to that of the gating algorithm up to ρ of about 6.8. This result makes us understand how the addition of a cut should be

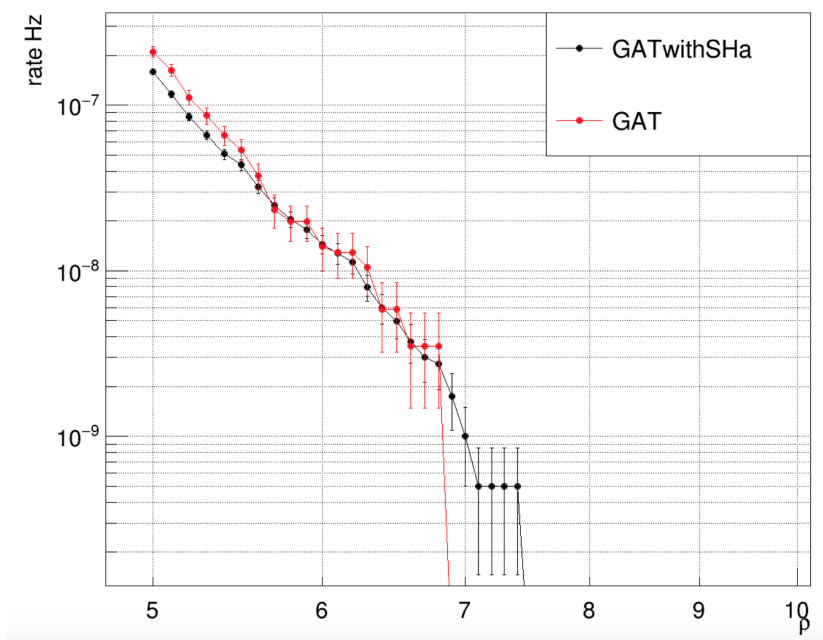


Figure 3.10: Cumulative curve of rate vs ρ obtained using the Gating alone and SHaVeD added to the Gating. SHaVeD can improve the analysis up to ρ of about 5.5, while it has a trend comparable to the Gating up to ρ of about 6.8.

well-calibrated according to the performance obtained independently from the pipeline. For cWB, this would mean excluding 7 hours more from the analysis.

If the loss of 7 hours out of a 20 day run causes the elimination of the loudest interferometer glitches from the analysis, then it can be argued that this pre-processing stem is worth the price in terms of lost up-time.

3.2.3 SHaVeD in post-production

Both X-SphRad and cWB apply cuts in the post-production stage, meaning after trigger reconstruction. In this section, we show the results obtained by applying SHaVeD in different scenarios. We report for each case analysed, the corresponding table of 'events' detected in the background.

Recall that, because of the inserted non-physical time lags to one of the detectors, 'events' are caused by noise as the candidates revealed in the background have no coincidence in the network of detectors. Each table shows eight features relating to the event found, including ρ , lags between the detectors and GPS times. The third column `cat3` indicates whether the post-production cut, in this case, SHaVeD, has identified and therefore vetoed the corresponding GW candidates. This information helps to reveal at a glance when SHaVeD has helped to clean up the selection of post-production 'candidate events'.

The first case study provides for the inclusion of the CWB gating in pre-production. A 130-year background is analysed, with SHaVeD in post-production with a threshold of 1%. Figure 3.11 shows both curves of rate vs ρ obtained with (red dots) and without (black dots) the application of SHaVeD. Figure 3.12 shows the loudest event list relative to that analysis.

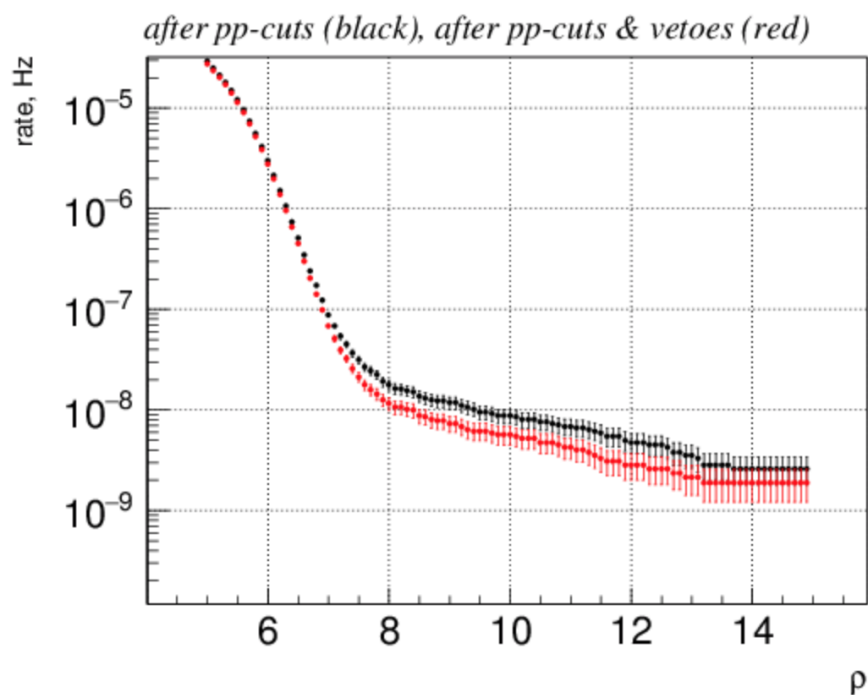


Figure 3.11: Cumulative curve of rate vs ρ with (red dots) and without (black dots) the application of SHaVeD. The comparison shows how SHaVeD improves the pipeline analysis in terms of glitches identification and rejection. This test analysed 130 years of background. Here no cWB long-duration cuts have been applied.

Loudest Event List

[\(full list of events at \$\rho > 0.00\$ \)](#)

ID	cat3	rho[0]	GPS L1	GPS H1	SNR L1	SNR H1
1	H	26.73	1185593081.71	1185591835.71	53.9	62.4
2		21.24	1187260234.05	1187258640.05	64.8	44.7
3		20.20	1186111126.77	1186108204.77	67.8	64.0
4	L	19.39	1186114280.33	1186114930.34	55.7	31.6
5		18.06	1185690806.91	1185691966.91	44.7	45.8
6		17.08	1185682091.71	1185679985.72	31.6	26.5
7	L	17.05	1185202672.85	1185200854.84	52.0	33.2
8		16.81	1187399910.91	1187402202.91	38.7	30.8
9		16.22	1185531352.56	1185533982.55	29.5	20.2
10		15.44	1185957122.54	1185957720.53	52.9	27.9

Figure 3.12: The cWB loudest event list: ID is the identification number. "cat3" column shows that SHaVeD removes three events among the top ten. This test analysed 130 years of background. Here no cWB long-duration cuts have been applied.

For completeness, we analysed the same scenario including the cWB cuts in transient long-duration search in post production. Figure 3.13 shows both curves of rate vs ρ obtained with (red dots) and without (black dots) the application of SHaVeD. Figure 3.14 shows the loudest event list related to this analysis.

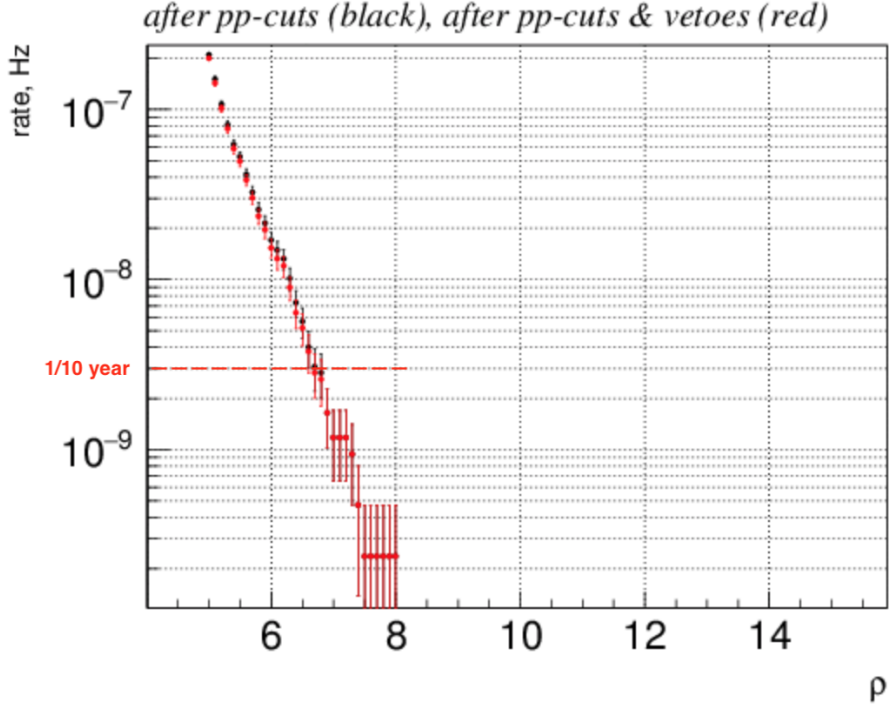


Figure 3.13: Cumulative curve of rate vs ρ with (red dots) and without (black dots) the application of SHaVeD. The comparison shows no substantial difference using SHaVeD (red dots) in addition to the cWB Long-duration veto (black dots). This test analysed 130 years of background. Here both cWB Gating and cWB long-duration cuts have been applied.

In order to understand the impact of SHaVeD in post-production by minimizing the influence of cWB parameters, we show below the results obtained, excluding both cWB gating in pre-production and cWB long-duration veto in post-production (Figure 3.15). The following analysis was carried out on a background of 485 years with a SHaVeD threshold of 1%. Figure 3.16 shows the loudest event list related to this analysis. Results obtained demonstrate the capability of SHaVeD to veto seven 'fake' events among the top ten.

Loudest Event List

(full list of events at $\rho > 0.00$)

ID	cat3	rho[0]	GPS L1	GPS H1	SNR L1	SNR H1
1		8.02	1185004814.76	1185007790.76	7.4	8.8
2		7.47	1184985296.17	1184983914.18	6.2	10.5
3		7.35	1185363009.44	1185365743.45	12.2	7.3
4		7.34	1185373195.58	1185373653.58	10.5	6.8
5		7.21	1186765446.64	1186767454.64	7.9	6.4
6		6.98	1185004815.62	1185004425.62	6.8	7.4
7		6.90	1185274573.22	1185275335.23	8.4	5.8
8	L	6.88	1186761955.70	1186762265.71	6.9	11.8
9		6.87	1185289925.41	1185287749.41	8.4	5.3
10		6.85	1185004816.42	1185004422.41	6.6	8.8

Figure 3.14: The cWB loudest event list: ID is the identification number. "cat3" column shows that SHaVeD removes one event among the top ten, so no significant effect beyond what the cWB cuts have already achieved. This test analysed 130 years of background. Here both cWB Gating and cWB long-duration cuts have been applied.

A second analysis was carried out on a background of 130 years and with a SHaVeD threshold of 5%. Figure 3.17 shows both curves of rate vs ρ obtained with (red dots) and without (black dots) the application of SHaVeD. Figure 3.18 shows the related loudest event list.

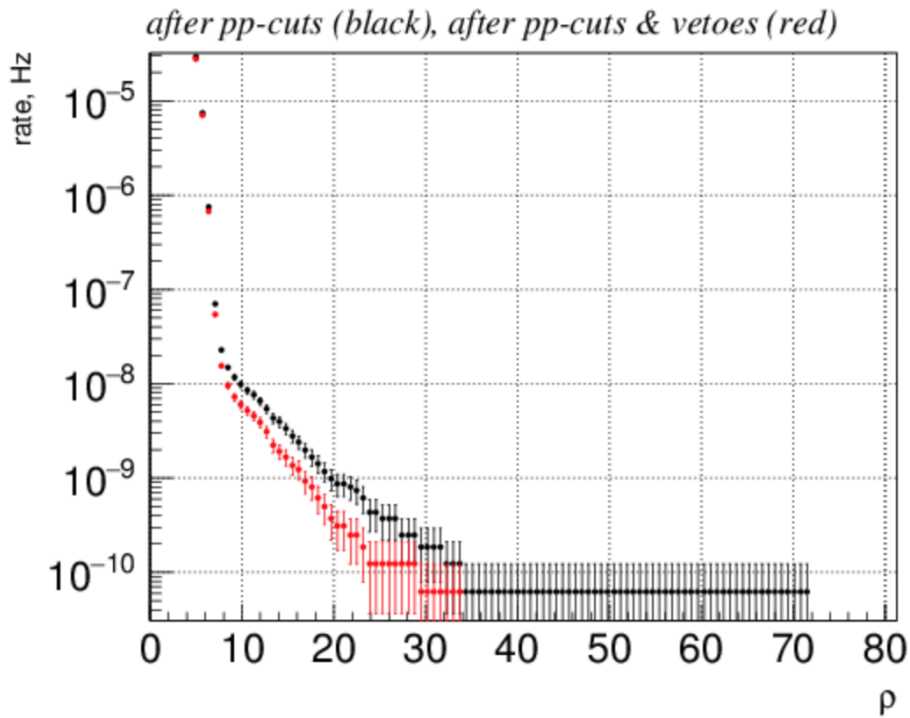


Figure 3.15: Cumulative curve of rate vs ρ with (red dots) and without (black dots) the application of SHaVeD. Here no cWB Gating and no cWB long-duration cuts have been applied in the pre-production stage. The comparison shows how SHaVeD significantly improves the pipeline performance. This test analysed 485 years of background. Here no cWB Gating and no cWB long-duration cuts have been applied.

Loudest Event List

(full list of events at $\rho > 0.00$)

ID	cat3	rho[0]	GPS L1	GPS H1	SNR L1	SNR H1
1	H	71.94	1186576436.14	1186572480.13	114.0	134.2
2		33.95	1185146483.04	1185151073.03	114.0	54.8
3	L	32.01	1186748441.37	1186760097.38	52.0	41.2
4		29.25	1187340670.01	1187330442.01	60.0	43.6
5	L	26.99	1187624330.73	1187614196.74	59.2	34.6
6	H	26.73	1185593081.71	1185591835.71	53.9	62.4
7	H	24.61	1186007890.81	1186012384.80	63.2	72.8
8		23.61	1185338101.19	1185349197.19	51.0	44.7
9	LH	23.58	1185509077.96	1185515011.95	40.0	38.7
10	LH	23.34	1185293463.85	1185300529.86	79.4	70.0

Figure 3.16: The cWB loudest event list: ID is the identification number. "cat3" column shows that SHaVeD removes seven events among the top ten. This test analysed 485 years of background. Here no cWB Gating and no cWB long-duration cuts have been applied.

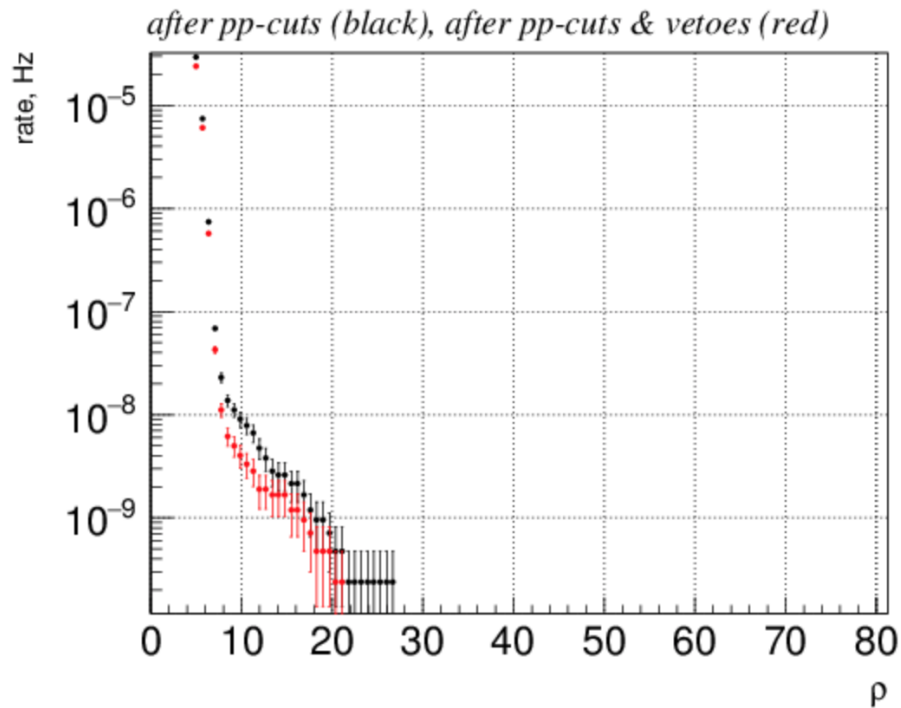


Figure 3.17: Cumulative curve of rate vs ρ with (red dots) and without (black dots) the application of SHaVeD. Here no cWB Gating is applied in the pre-production stage. The comparison shows how SHaVeD significantly improves the pipeline performance. This test analysed 130 years of background. Here no cWB Gating and no cWB long-duration cuts have been applied.

Loudest Event List

(full list of events at $\rho > 0.00$)

ID	cat3	rho[0]	GPS L1	GPS H1	SNR L1	SNR H1
1	H	26.73	1185593081.71	1185591835.71	53.9	62.4
2		21.24	1187260234.05	1187258640.05	64.8	44.7
3		20.20	1186111126.77	1186108204.77	67.8	64.0
4	L	19.39	1186114280.33	1186114930.34	55.7	31.6
5		18.06	1185690806.91	1185691966.91	44.7	45.8
6		17.08	1185682091.71	1185679985.72	31.6	26.5
7	L	17.05	1185202672.85	1185200854.84	52.0	33.2
8	LH	16.81	1187399910.91	1187402202.91	38.7	30.8
9		16.22	1185531352.56	1185533982.55	29.5	20.2
10		15.44	1185957122.54	1185957720.53	52.9	27.9

Figure 3.18: The cWB loudest event list: ID is the identification number. "cat3" refers to SHaVeD and it shows that SHaVeD removes four events among the top ten. This test analysed 130 years of background. Here no cWB Gating and no cWB long-duration cuts have been applied.

3.2.4 Tests of SHaVeD using ad-hoc waveform injections

For completeness we estimate the effect of SHaVeD on the detection efficiency of a GW signal. It has been done analysing simulated signals. Specifically, we analysed the ADI A waveform (see Section 2.2). The background distribution, related to this analysis, is that shown in Figure 3.9. Figures 3.19 and 3.20 show the detection efficiency plots generated by using cWB without and with SHaVeD in the pre-production respectively with signal amplitude corresponding to a false alarm rate (FAR) of 1/10 years.

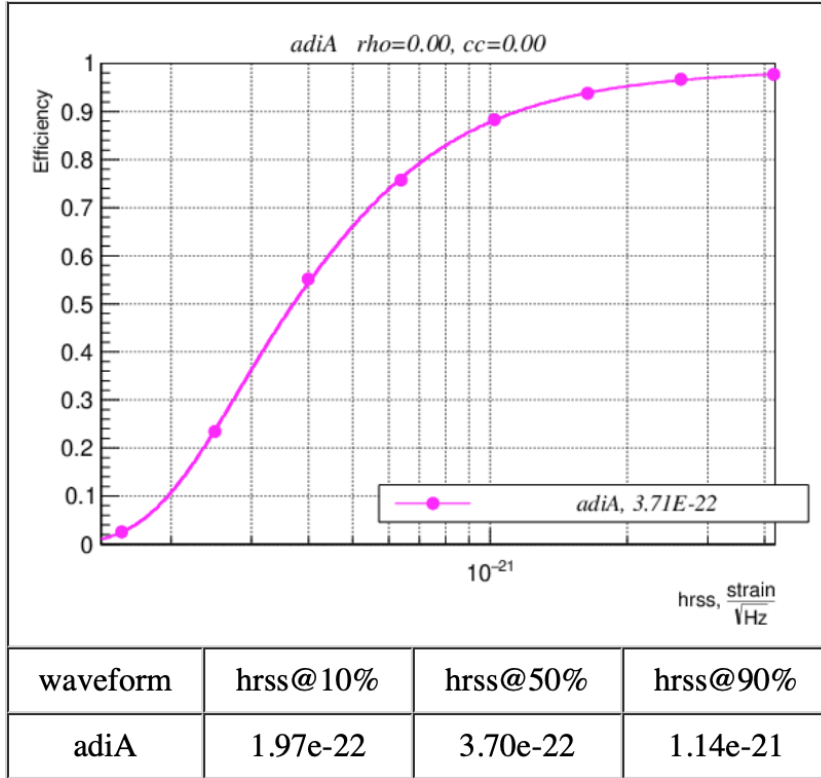


Figure 3.19: Detection efficiency of cWB as a function of the injection amplitude of the ADI A signal. The value of the signal amplitude where the efficiency is 50 % is $3.7e^{-22}$. The threshold is set such that the false alarm rate is 1 event every 10 years, as determined by parallel analysis of timeshifted data.

Comparing the hrss values, we see how the application of shaved does not

show an increase in the detection efficiency. The hrss at 50% is unaltered because the efficiency is estimated at a FAR of 1/10 years while the SHaVeD algorithm is effective at lower rate, i.e. higher FAR (Figure 3.15). This result also implies that the SHaVeD algorithm does not incorrectly reject GW signal.

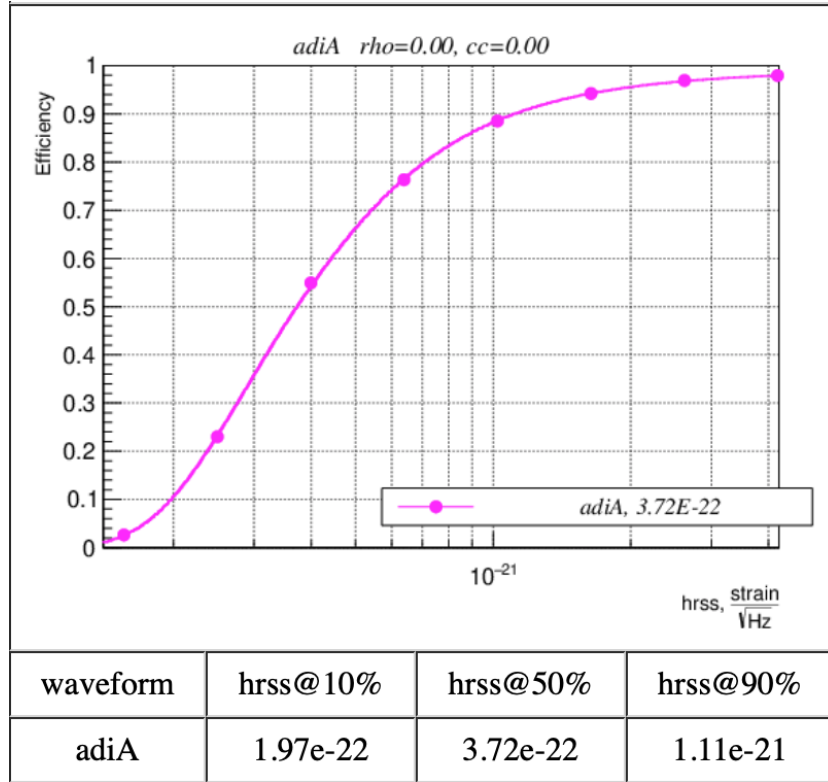


Figure 3.20: Detection efficiency of cWB as a function of the injection amplitude of the ADI A signal, with SHaVeD applied in the pre-production stage. The value of the signal amplitude where the efficiency is 50 % is $3.72e^{-22}$. The threshold is set such that the false alarm rate is 1 event every 10 years, as determined by parallel analysis of timeshifted data.

3.3 GW170817 event

One of the milestones reached during the O2 run was the detection of the first event generated by the merger of two neutron stars. Occurring on August 17th 2017 (GW170817) [55], this detection represents the beginning of the new “multi-messenger era”[56], since electromagnetic radiation was detected in association with the production of a gravitational wave. The gravitational wave signal was visible in the interferometer data for the last 100 seconds before the merging time at 12.41.04 UTC (GPS: 1187008882.4).

The signal arrived first at the Italian interferometer Virgo, 22 milliseconds later to the LIGO observatory in Livingston, Louisiana, and 3 milliseconds later to the LIGO observatory in Hanford, Washington. Since all the three interferometers were active at that time, it was possible to locate the source in an area of 28 square degrees in the southern sky³(Figure 3.21).

A short gamma-ray burst was observed by the Fermi telescope and by the INTEGRAL space telescope (GRB 170817A) 1.74 seconds after the GW signal was received on Earth presumably. The first optical radiation (SSS17a) [65] associated with the collision of the two neutron stars was detected 10 hours and 52 minutes later. This detection was made using the Swope telescope and which operates in the near-infrared that is located at the Las Campanas Observatory, in Chile. Nine days later, the source was observed in X-rays by to the Chandra X-ray Observatory orbital telescope, while sixteen days later, it was observed in radio waves by to the grouping of Very Large Array radio telescopes [6]. In total, over 70 observatories, working with the electromagnetic spectrum, saw the event thanks to the GW170817 detection [58].

Figure 3.22 shows the time-frequency representations of the GW170817 event, observed by the LIGO- Hanford (top), LIGO-Livingston (middle), and Virgo (bottom) detectors. All information regarding the gravitational-wave GW170817 event can be found in [55]. As shown in Figure 3.22, the GW signal is not visible in the Virgo TF map. The explanation is to be found in

³The skymap probability of GW triggers given to electromagnetic partners usually refer to the 90% probability that the signal is inside that region.

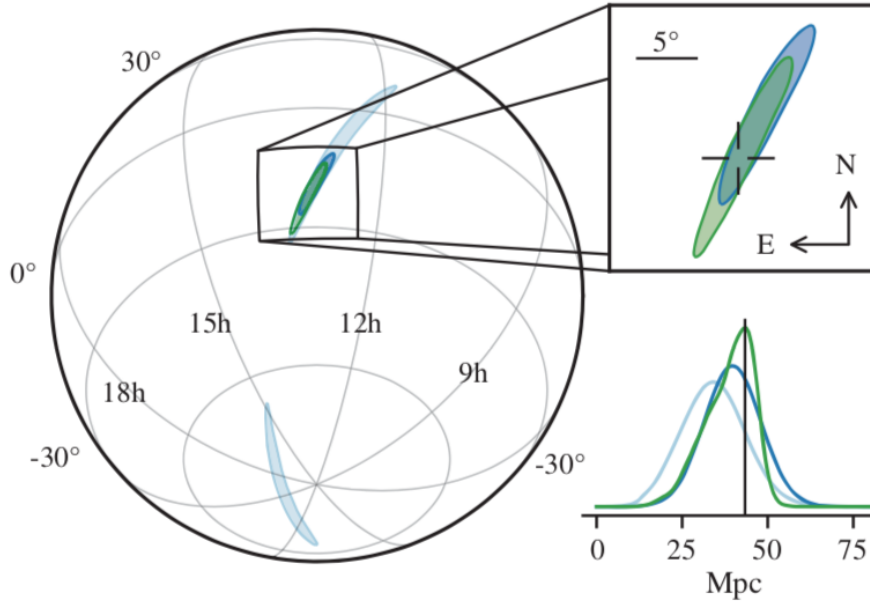


Figure 3.21: Sky location reconstructed for GW170817 by a rapid localization algorithm from a Hanford-Livingston (190deg^2 , light blue contours) and Hanford-Livingston-Virgo (31deg^2 , dark blue contours) analysis. A higher latency Hanford-Livingston-Virgo analysis improved the localization (28deg^2 , green contours)(90 % probability)[58].

the non-stationary nature of the Virgo data above 150 Hz due to scattered light from the output optics modulated by alignment fluctuations and below 30 Hz due to seismic noise [55].

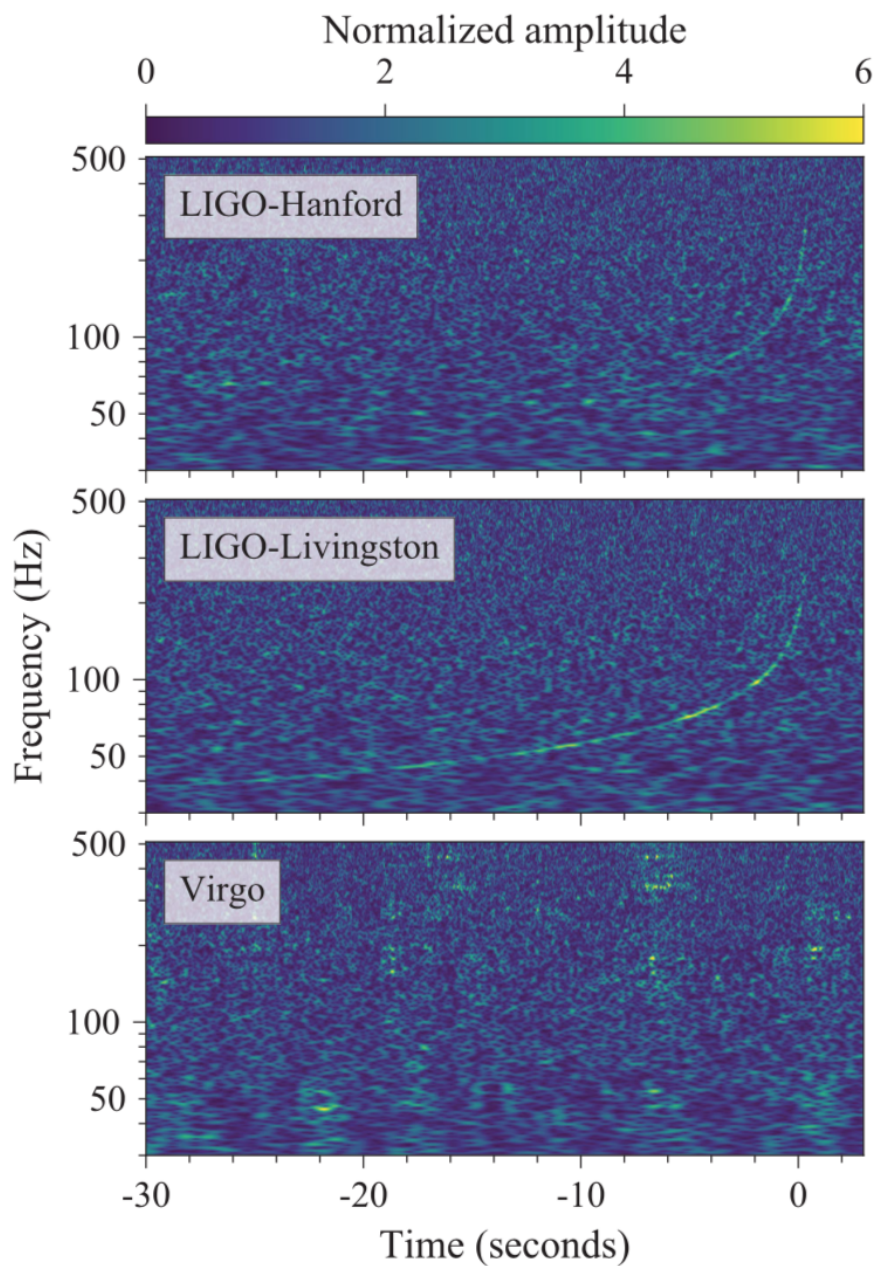


Figure 3.22: Time-frequency representations of GW170817 event, before the merging time at GPS 1187008882.4, observed by the LIGO-Hanford (top), LIGO-Livingston (middle), and Virgo (bottom) detectors [58].

3.3.1 An issue: a glitch in the LIGO-Livingston data

As is known, the presence of glitches is frequent in the data analysed in this work. The event GW170817 was also affected, specifically the data from the LIGO-Livingston detector. This glitch was a high-amplitude, short-duration transient signal caused an overflow in the digital-to-analog converter of the optic drive signal and prevented the searches from detecting an event trigger for the GW170817 in the LIGO-Livingston detector.

The glitch was subtracted from the data using an appropriate technique of denoising (Figure 3.23). The analyses applied a window function to zero out the data around the glitch to mitigate the its effect on signal reconstruction [55].

We, therefore, considered it interesting to analyse the data around the glitch with cWB and to study the impact of SHaVeD on these data. We worked on a 1200 seconds long segment containing the glitch in the GW170817 (GPS: from 1187008687.000 to 1187009927.000). This analysis, in which no cWB gating and no cWB long-duration cuts have been applied, identifies the glitch as a GW candidate event, with an SNR of 18.4 and a GPS central time at 1187008881.390. Figure 3.24 shows the time-frequency map of the LIGO-Livingston detector; the glitch is visible at the GPS time mentioned above.

In Figure 3.25, we show the likelihood TF map where just the glitch is visible. Both time-frequency and likelihood time-frequency maps show how the glitch compromises the signal detection. This analysis helps to understand how important is noise rejection in signal searches. Excluding all vetoes and cuts in the pre-processing stage allowed glitches to contaminate data preventing GW signal detection.

3.3.2 A challenge: applying SHaVeD in the pre-whitening stage

The presence of a loud glitch, in conjunction with an event like the GW170817, is the perfect opportunity to test SHaVeD's ability to identify and therefore reject glitches that pollute the data. To evaluate its performance, we de-

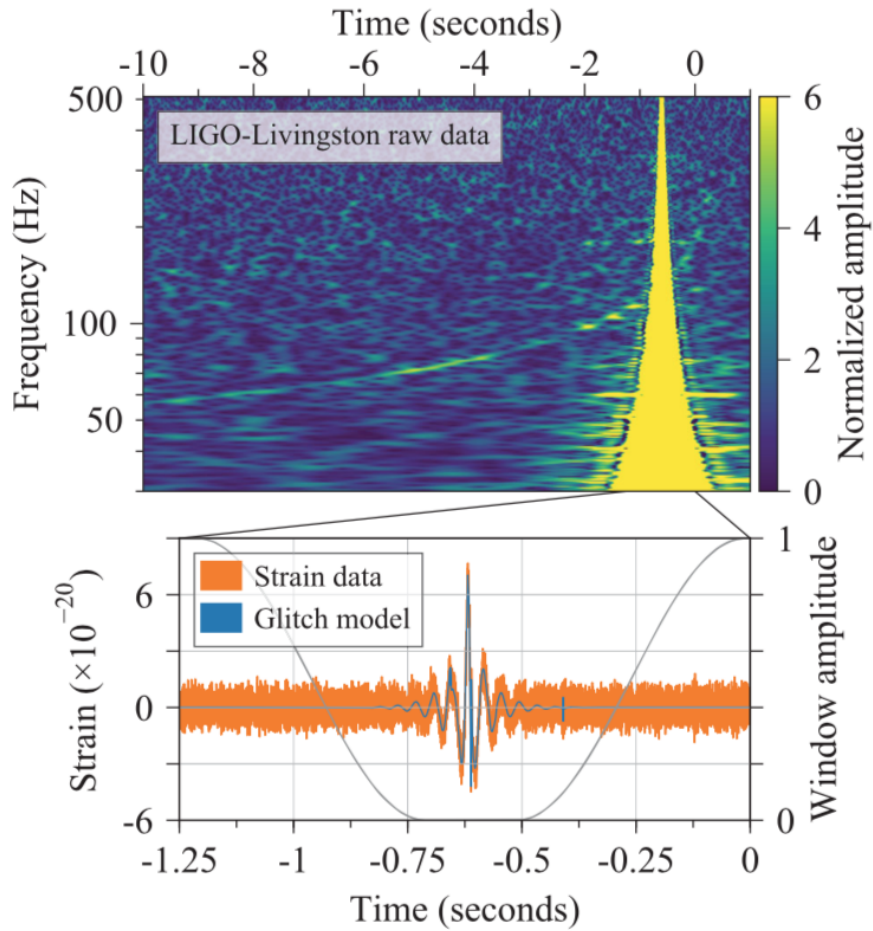


Figure 3.23: Top panel: A time-frequency representation of the raw LIGO-Livingston data used in the initial identification of GW170817 [76]. The coalescence time reported by the search is at time 0.4 s in this figure and the glitch occurs 1.1 s before this time. Bottom panel: The raw LIGO-Livingston strain data (orange curve) showing the glitch in the time domain [58].

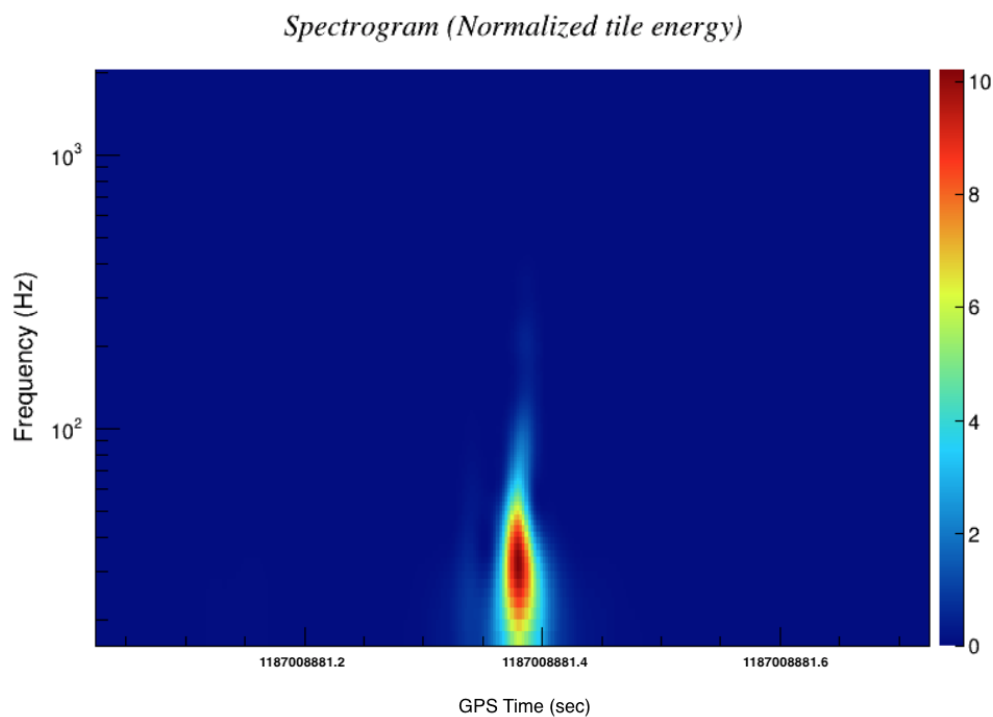


Figure 3.24: Time-frequency map of the whitened zoom data around the glitch, provided by LIGO-Livingston detector for the data segment from 1187008687.000 to 1187009927.000 GPS time [43].

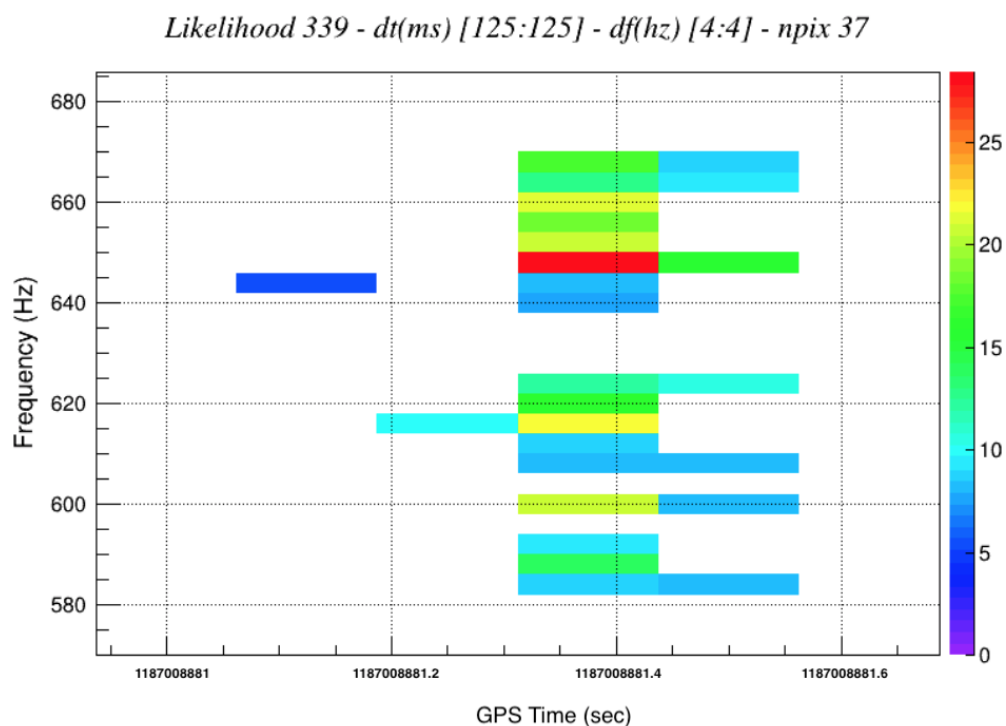


Figure 3.25: Likelihood time-frequency map of the whitened zoom data around the glitch, provided by the LIGO-Livingston detector for the data segment from 1187008687.000 to 1187009927.000 GPS time [43]. Pixels due to GW are not visible due to the glitch.

cided to apply the veto on the row data, which means in pre-production and even before whitening. The analysis with SHaVeD is performed on the 1200 seconds long segment from 1187008780.000 to 1187010020.000 GPS time.

First, an inverse Tukey window was applied in order to clean the data frame to be analysed. Figure 3.26 schematically shows how the window function works over the GPS time of the GW170817 event. The GPS time

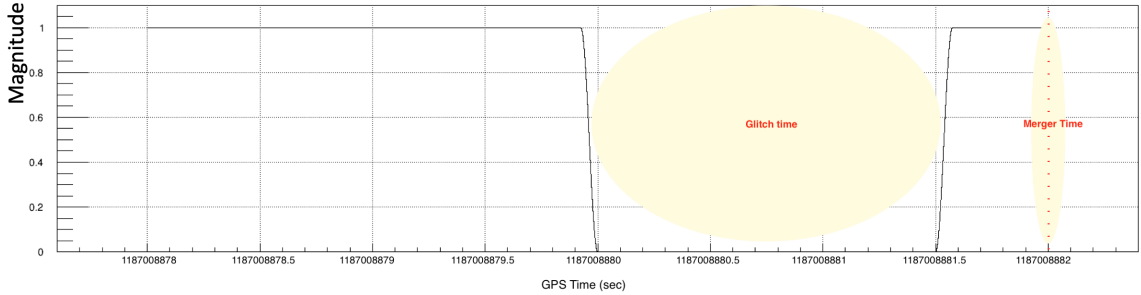


Figure 3.26: Example of the inverse Tukey Window function used to apply SHaVeD in the pre-production and pre-whitening analysis with cWB. Yellow circles highlight the GPS time when glitch and merger occurred respectively.

of the glitch was used to bring its contribution to zero and thus analyse the remaining detected signal.

Figure 3.27 shows the application of the inverse Tukey window on the analysed segment. The figure shows how windowing crushes the signal generated by the glitch to zero.

We then analysed the cleaned data frame with cWB, obtaining the time-frequency map (Figure 3.28) and the corresponding likelihood TF map (Figure 3.29). Figure 3.29 shows the 1-second long event reconstructed by cWB, with an SNR of 16.1 and a GPS central time at 1187008881.973.

This analysis aimed to test the ability of SHaVeD in identifying and rejecting glitches with a real GW event such as GW170817.

A preliminary analysis was performed without vetoes and cuts usually applied during the cWB standard analysis. In this was we were able to clearly see how the glitch has irremediably compromised the search for GW signals.

We made a second analysis, in which we included SHaVeD; It was used

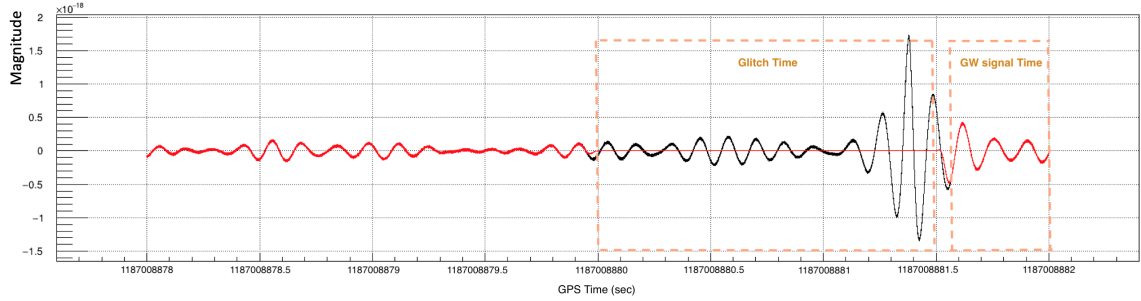


Figure 3.27: Example of how the inverse Tukey Window function works with SHaVeD to cut off the glitch: the black line is the original signal; the red line is the signal after the windowing, which leads glitch contribution to zero. Orange dashed boxes indicates where the glitch and the GW signal occurred respectively.

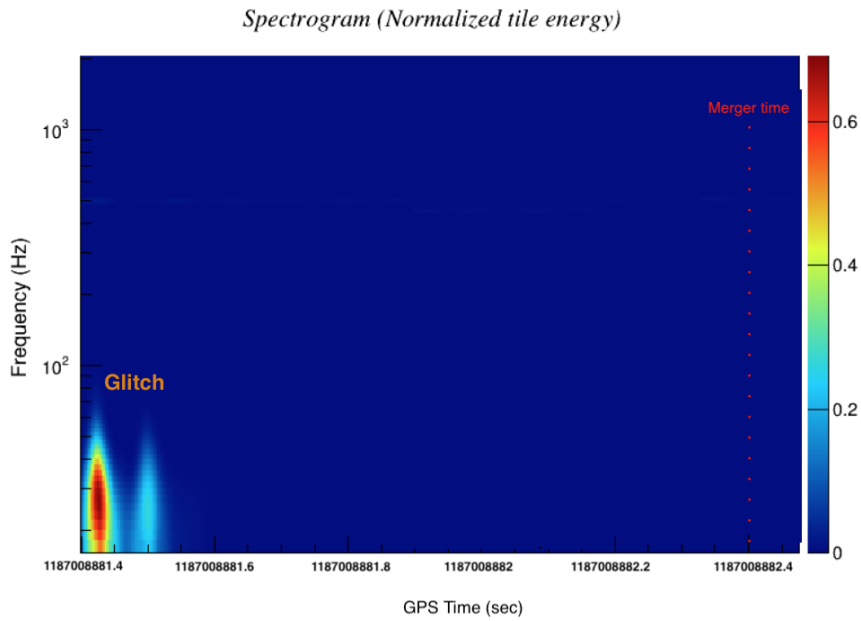


Figure 3.28: Time-frequency map of the whitened data around the glitch, provided by the LIGO-Livingston detector for the data segment from 1187008780.000 to 1187010020.000 GPS time [43].

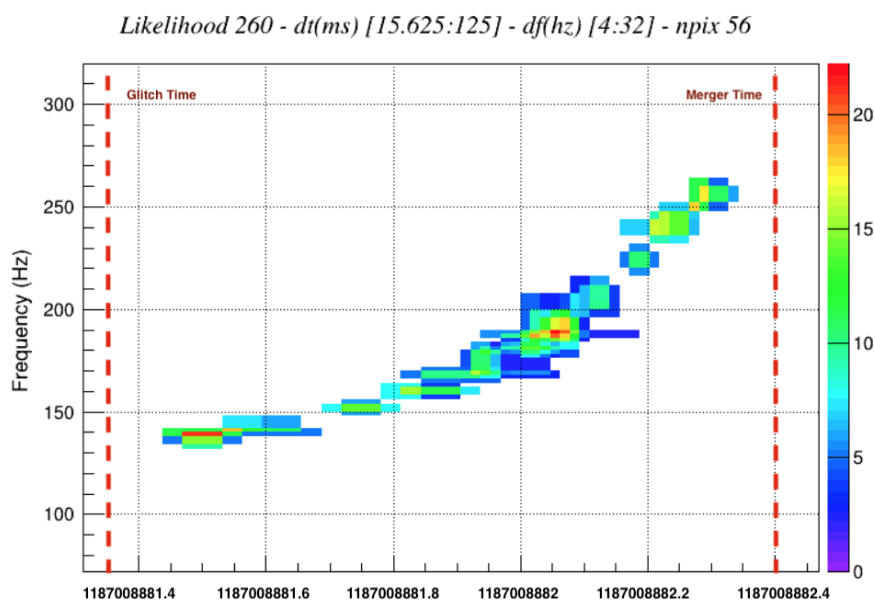


Figure 3.29: Likelihood time-frequency map of the whitened data around the glitch, provided by the LIGO-Livingston detector for the data segment from 1187008780.000 to 1187010020.000 GPS time [43].

to identify GPS time of glitches that occurred in the 1200 seconds containing GW170817 event. A window function was applied around GPS times vetoed by SHaVeD.

In conclusion, comparing the Likelihood Time-frequency maps obtained before (Figure 3.25) and after (Figure 3.29) the application of SHaVeD, we were able to see how the glitch, that contaminated the GW searches at first, was vetoed by SHaVeD.

SHaVeD has worked as we expected, ensuring the success of the analysis and making sure that cWB was then able to reconstruct the last second of the GW signal, which otherwise would have been lost ⁴.

3.4 Raw Analysis of O3 data

For completeness, we have also tested SHaVeD of the O3 run currently still in progress. Figures 3.30 and 3.31 show the observing time and observing segments respectively, both starting from April 4th, 2019, and showing the following 16 weeks [60]. Specifically, we have analysed with cWB the segments from April 16th, 2019 (1239494417 GPS time) to May 22nd, 2019 (1242604817 GPS time), considering the data provided by the LH network. This period corresponds to approximately 19 days of coincident data. The period considered by this work is highlighted in both figures.

We emphasize that this raw analysis of O3 data aims to provide an idea about the results that would be obtained using SHaVeD in post-production. We say this because, at the time of the analysis, the 'data quality' (see section 2.5.1) needed for a full cWB analysis had not yet been released.

Due to the lack of revised and approved 'data quality' at the time of analysis, the application of SHaVeD was just performed in the post-production stage of cWB. The background is around 130 years and the threshold chosen for SHaVeD is 1%.

We recall that X-SphRad would relish considerable benefits if it were

⁴This consideration is exclusively related to the independent analysis carried out for this work. The standard analysis, carried out by cWB for the GW170817, included the gating plugin.

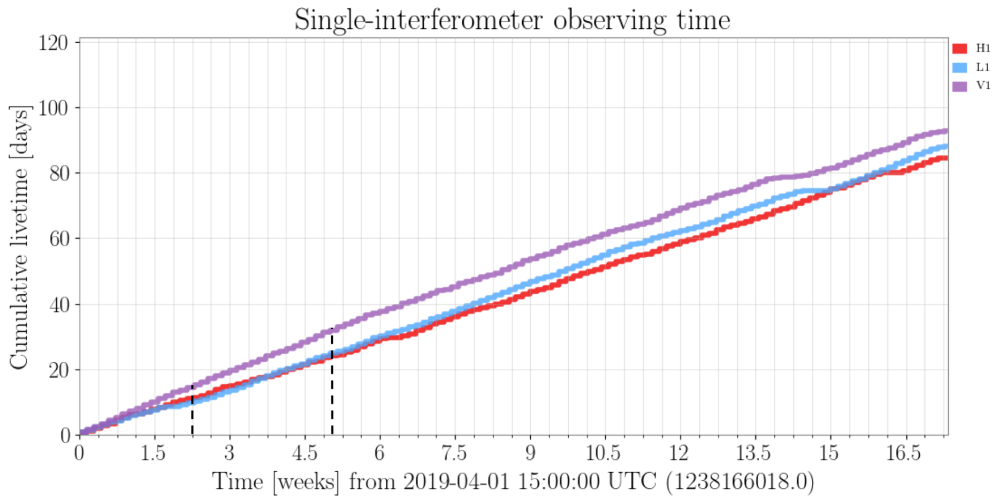


Figure 3.30: LIGO observing time for the O3 scientific run. Black dashed lines highlight the coincident time analysed in this work [63].

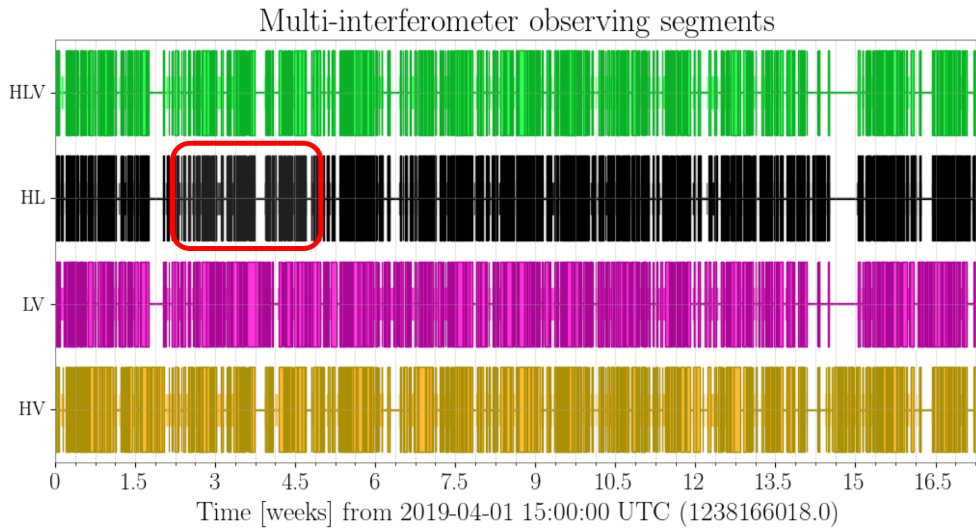


Figure 3.31: Multi-interferometer observing segments for the O3 scientific run. The red box highlights the coincident time analysed in this work [63].

able to autonomously generate an effective veto similar to the gating used by cWB. The development and verification of the effectiveness of SHaVeD

would show this opportunity.

Then, given the ultimate goal of including SHaVeD in X-SphRad, we excluded cWB gating and all cWB post-production cuts of short and long burst signal searches.

As we did for the O2 analysis (see section 3.2), we use the “rate vs ρ ” distribution to evaluate the impact of SHaVeD on the cWB analysis (Figure 3.32). Looking at the ρ values (fourth column) in Figure 3.33, SHaVeD has reduced the amplitude of the loudest event by a factor of 3.

Recall that, ρ (see Equation 3.1) is comparable with the SNR, especially for real signals, where the netCC parameter tends to 1.

Then, SHaVeD would provide us a factor of 3 in the value of hrss where we set the limit, which means we have eliminated all events in a volume 9 times bigger as a consequence of this veto. It is also important to underline the need to repeat this analysis with updated ‘data quality’ in order to quantify the impact of SHaVeD. Moreover, it would be useful, in these conditions, to study its application in pre-production and to be compared to the standard cWB cuts.

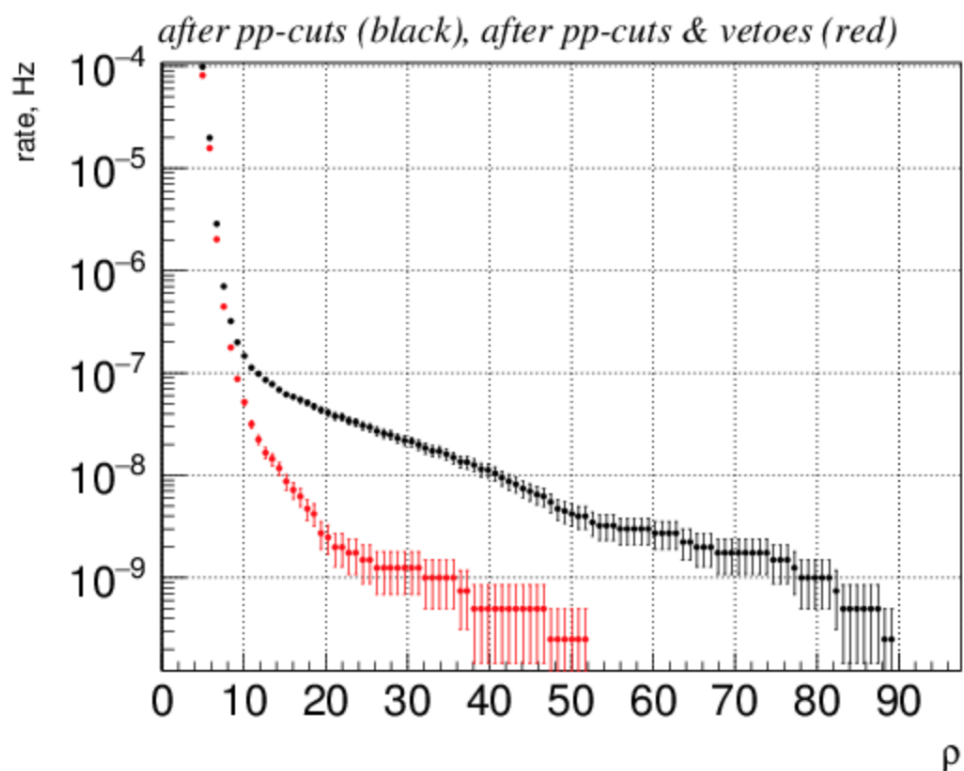


Figure 3.32: Cumulative curve of rate vs ρ with (red dots) and without (black dots) the application of SHaVeD. The comparison shows how SHaVeD significantly improves the pipeline analysis. This test analysed 130 years of background. Here no cWB Gating and no cWB long-duration cuts have been applied.

Loudest Event List

(full list of events at $\rho > 0.00$)

ID	cat3	rho[0]	GPS L1	GPS H1	SNR L1	SNR H1
1	LH	158.36	1240851509.47	1240852011.48	2236.1	4123.1
2	LH	87.65	1240563004.21	1240565772.20	989.9	748.3
3	LH	83.18	1241673642.62	1241675666.63	2097.6	1183.2
4	LH	81.73	1239898602.94	1239895828.94	374.2	387.3
5	LH	77.63	1240977104.19	1240979318.19	266.5	284.6
6	H	76.77	1240278554.70	1240280620.71	469.0	266.5
7	LH	74.12	1241433025.75	1241430321.76	1048.8	479.6
8	LH	67.59	1241248787.27	1241246771.26	412.3	275.7
9	LH	65.34	1241669289.64	1241666497.64	469.0	412.3
10	LH	63.35	1239961686.84	1239962050.85	2190.9	616.4
11	LH	63.15	1239673244.02	1239675972.03	1949.4	3146.4
12	LH	59.75	1241425506.98	1241427450.98	1048.8	781.0
13	LH	55.18	1242369415.61	1242370911.61	189.7	192.4
14	LH	53.12	1239674171.59	1239675819.59	916.5	714.1
15		52.39	1241611878.56	1241614670.57	94.9	130.4
16	LH	52.07	1241521148.95	1241517880.95	700.0	624.5
17	LH	50.14	1242145969.59	1242148623.58	346.4	251.0
18	LH	49.27	1240638303.69	1240641553.68	721.1	565.7
19	LH	48.85	1242253065.40	1242254841.40	435.9	313.0
20	LH	47.90	1241712030.85	1241710794.85	692.8	519.6

Figure 3.33: Loudest event list: "cat3" column shows that SHaVeD removes almost all events among the top twenty. This test analysed 130 years of background. Here no cWB Gating and no cWB long-duration cuts have been applied.

3.5 Potential and limits: a SWOT analysis

In this section, we have described SHaVeD as a tool for identifying and eliminating glitches that contaminate the data provided by ground-based gravitational-wave detectors. A SWOT (Strengths Weakness Opportunities Threats) analysis is presented here to illustrate its potential, limits, and possible future investigations (Figure 3.34).

Strengths:

- Use of a simple and short algorithm based on variables already generated by the X-SphRad pipeline;
- Provides X-SphRad with a veto applicable both in 'pre' and 'post' production to enhance the performance of the pipeline itself;
- Successfully rejects a large class of loud glitches at minimal cost in terms of reduction in livetime.

Weakness:

- Dependency on glitch features: the longer the glitch duration, the longer the cut that will be made and therefore, the longer the time excluded from the analysis.

Opportunities:

- Application of the veto in pre-production before whitening occurs. This upgrade would allow the pipeline to calculate cut thresholds (see section 2.4.2) after removing glitches: By mitigating these noise sources before whitening, we would have lower cut thresholds, boosting sensitivity at a negligible computing cost.

Threats:

- Tests performed in this thesis are limited to the off-line analysis;
- Need for further tests and therefore people (manpower needed);

- Analysis work in LIGO/Virgo is person-power limited, and approval of a new glitch rejection veto to be used as a part of an established analysis pipeline would require a time and person-hours intensive analysis review.

Chapter 4

Testing phenomenological waveforms with X-SphRad

In this chapter we describe our study of the response of the X-SphRad pipeline to injections intended to model the gravitational waves emitted when material accretes onto a neutron star (NS) in the so-called fallback accretion model. For simplicity, from here, we will refer to the waveforms described in [61] as PT12. A general overview of the scenario is presented in subsection 4.1, followed in 4.2 by the characteristics of the waveforms built following this semi-analytical model. Finally, we report the observations and results obtained from an analysis of PT12 conducted with X-SphRad. Six different waveforms were injected into the pipeline and analysed as simulated signals. The collapsar scenario is studied as a promising source of GWs, and several analyses have already been carried out [73, 74, 75, 72]. Analysing PT12 with X-SphRad was a way to evaluate the performance of the pipeline in a higher frequency range and on astrophysics waveforms different from the current ones. More details on the data analysis are provided in section 4.3.

4.1 Scenario

Massive stars end their life cycle as neutron stars or black holes. Many factors affect the final state: the mass of the star, the angular momentum,

the variation of the explosion energy to which the accretion rate is sensitive, and the type of progenitor [61]. From the electromagnetic point of view, there is not enough information on the final state, since neither class of compact object emits a strong electromagnetic signal once it approaches the final state. The detection of gravitational-wave signals with these waveforms would permit us to verify or reject the fallback accretion model of the late stage evolution of compact stars.. For this reason, studying the different scenarios associated with these events provides new points of view. In this chapter, we illustrate the waveforms for the fallback mechanism for creating BHs [61].

The model scenario refers to core-collapse supernovae that releases its stellar mantle with a weak collapse [62]. This condition means that a young NS will be subject to a fallback accretion, a process that will increase the mass up to its limit leading to BHs. For PT12, Piro and Thrane consider a fallback accretion rate of $\dot{M} \sim (10^{-4} - 10^{-2})M_{\odot}s^{-1}$ [63][64].

Imagine that the fallback material forms a disk before being absorbed by the neutron star itself. The presence of this disk increases the angular momentum to such a point that the spin parameter $\beta = \frac{T}{|W|}$ reaches its critical value β_c ; The critical value depends on the model assumed for the data. For this scenario is $\beta_c = 0.14$ [61]. Here T is the rotational energy, and W is the gravitational energy. When β exceeds its critical value, the system has instability and produces gravitational waves [66][67]. Note that the star torques down when $\beta > \beta_c$ and spins up when $\beta < \beta_c$; therefore, the NS reaches a sort of unstable equilibrium for here $\beta \sim \beta_c$, and the mass increases continuously. The GWs are produced until the mass of the NS increases to such a point that it collapses.

4.2 PT12 waveforms: a semi-analytical model

In this section we present a theoretical treatment of a particular model of mass accretion and gravitational wave emission by a compact object subject to accretion, as described in detail by reference [61]. This model, which is an attempt to describe the physics underlying the astronomically observed

phenomenon known as a collapsar¹, takes into account several factors, such as the accretion rate of the mass of the star, the variations in angular momentum, and the shape of the massive disk formed around the NS and how instabilities lead to the production of gravitational waves. We reiterate here, that the ability to detect gravitational waves described by waveforms such as PT12, would represent experimental evidence of still purely theoretical stellar processes. The first consideration made in [61] is that neutron stars have progenitors with a ZAMS (Zero Age Main Sequence) mass of about $25M_{\odot}$ and with an inefficient semi-convective mixing. Under these conditions, there is a mass loss of up to $14.6M_{\odot}$ at the time of the core-collapse, with an explosion energy of between $(2.6 \times 10^{50} - 1.3 \times 10^{51})\text{erg}$ [63]. At this point, we study the increasing NS mass through the accretion rate estimated as in Equation 4.1:

$$\dot{M} = \eta 10^{-3} t^{1/2} M_{\odot} s^{-1} \quad (4.1)$$

where the η factor depends on the energy of the explosion, which is equivalent to saying that the accretion rate is sensitive to changes in energy. In the PT12 model, Equation 4.2 estimates the gravitational mass of the remnant:

$$M_{grav} = M_{baryon} \left(1 + \frac{3}{5} \frac{GM_{baryon}}{R_{grav}c^2}\right)^{-1} \quad (4.2)$$

where M_{baryon} is the baryonic mass. This adjustment between the baryonic and gravitational mass corresponds to a correction of 5% -30%.

A second aspect addressed is how the NS gains angular momentum. It is assumed that the infalling material circularizes before reaching the stellar surface. If we define the angular momentum as $j \gtrsim (GM_0R_0)^{1/2} \approx 2 \times 10^{16} cm^2 s^{-1}$ (M_0, R_0 are the non-rotating mass and radius), we will have an NS torque [68][69] of about

$$N_{acc} \approx \dot{M}(GM_0R_e)^{1/2} \quad (4.3)$$

where R_e is the equatorial radius. N_{acc} corresponds to the mass rate

¹Collapsed star.

transferred through the disk [61].

We define the rotation rate through the spin parameter β ($\beta = \frac{T}{|W|}$). If no mechanism of energy loss occurs, we will have an asymmetrical spheroid as an equilibrium shape. The equation that links the spin parameter and the eccentricity of the spheroid [70][71] is

$$\beta = \frac{3}{2e^2} \left[1 - \frac{e(1-e^2)^{1/2}}{\sin^{-1}e} \right] - 1 \quad (4.4)$$

where $e^2 = 1 - (R_z/R_e)^2$, and R_z is the vertical radius.

When the spin parameter exceeds its critical value ($\beta > \beta_c$), instability is created, which leads to the production of gravitational waves. In the case where $\beta \sim \beta_c$, we expect the emission of GW when the accretion torque (Equation 4.3) is balanced by the removal of the angular momentum at a rate equal to:

$$N_{gw} = \dot{E}_{gw}/\Omega, \quad (4.5)$$

where E_{gw} is the energy loss associated with the emission of GWs and Ω is the spin frequency. Then, for $\beta \sim \beta_c$ we want $N_{gw} + N_{acc} \sim 0$.

The corresponding strain from these gravitational waves is:

$$h_0 = \frac{2GQ\Omega^2}{c^4D}$$

where D is the distance to the source and Q is the quadrupole moment.

The equations for the two polarizations are:

$$h_+(t) = h_0(1 + \cos^2 i) \cos(2\pi ft)$$

$$h_\times(t) = 2h_0 \cos i \sin(2\pi ft)$$

where $f = \Omega/\pi$ is the gravitational wave frequency and i is the inclination of the source.

4.3 PT12 analysis with X-SPhRad

The investigation into the collapsar scenario and the detectability of the waveforms that describe it, represents a current challenge. PT12 waveforms are the result of a continuation of a collaborative effort between Anthony Piro (Associate Professor at the University of Southern California) and Kiranjyot Gill (Ph.D. student at the Harvard University). She provided me, with Piro approval, files with time, strains h_x and h_y and, frequency of PT12 waveforms ready to be analysed. We report results obtained from the data analysis performed by X-SphRad by injecting the waveforms described by the PT12 model as simulated signals. This analysis aims to test the performance of the pipeline with waveforms of astrophysical origin different from those studied in the previous chapters.

4.3.1 Analysis Parameters

We analysed data given by LIGO detectors Hanford and Livingston sites, from Jul 25, 2017, 00:00:00 UTC to Aug 25, 2017, 00:00:00 UTC, corresponding to 20 days of coincident data [50]. The segment length is 512s. The frequency range is [24, 4000]Hz, with a sampling frequency of 8192 Hz. We injected into X-SphRad eight waveforms among astrophysical and ad-hoc types commonly used in long-burst signal searches (see section 2.5), plus six PT12 waveforms. From here on, we will refer to the individual PT12s as PT A, PT B, PT C, PT D, PT E, and PT F.

We briefly report some parameters that characterise the PT12 waveforms [124]. The code (owned by Piro), that generates the waveforms, first calculates the secular properties of the evolution as a function of time. The options are:

- Initial mass (M_{\odot}) : something between 1.2 – 2.5;
- Radius (Km): A typical value is 12, but you might want to choose higher values depending on rotational effects;
- Critical β : 0.14 for secular instabilities;
- Accretion variable η : from 0.1–10, which is proportional to the early accretion rate and inversely related to the energy of the supernova;

For our part, the PT12 provided by Jasmine Gill for this analysis have the following physical parameters [123]:

Waveforms	Radius (Km)	η	M (M_{\odot})
PT12 a	12	0.1	2
PT12 b	12	1	2
PT12 c	12	5	2
PT12 d	14.5	0.1	2.2
PT12 e	14.5	1	2.2
PT12 f	14.5	5	2.2

Table 4.1: Radius, Accretion variable and Initial Mass of PT12 waveforms.

Figures 4.1, 4.2, and 4.3 show the corresponding time-frequency maps, while Figure 4.4 contains information on duration and frequency for each waveform. We have also included, as simulated signals, eight commonly used waveforms to ensure that the pipeline work was done correctly. This chapter will not mention the results related to these simulations, as already described in Chapter 2. In any case, we report all the efficiency curves and the results obtained in Appendix D. We keep in mind that X-Sphrad, in papers published for the LV Collaboration, has presented results working on a frequency range between 24 and 2000 Hz. Analysing waveforms such as PT12, with minimum frequencies of 2400 Hz, pushes the maximum frequency of X-Sphrad to 4000 Hz. We will discuss in the next paragraph how this may have influenced the performance of the pipeline.

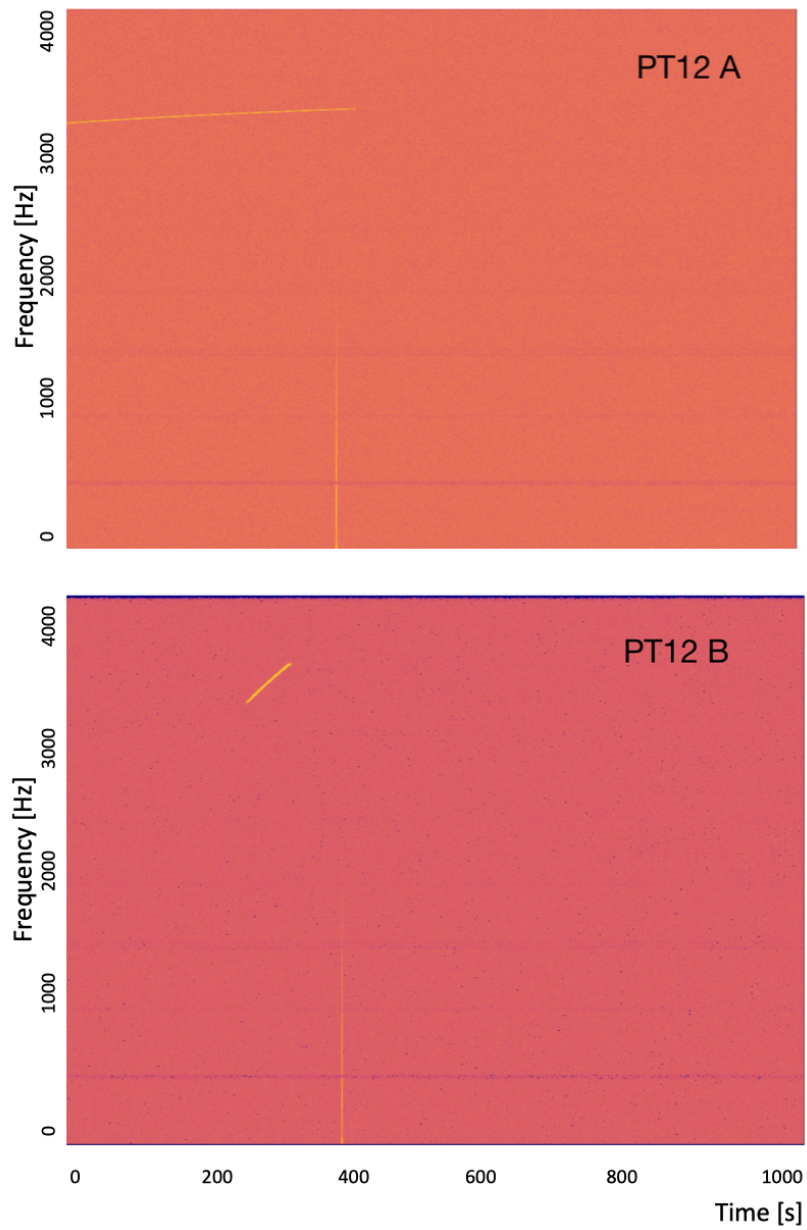


Figure 4.1: A representation of the PT-A and the PT-B waveforms in the time-frequency domain.

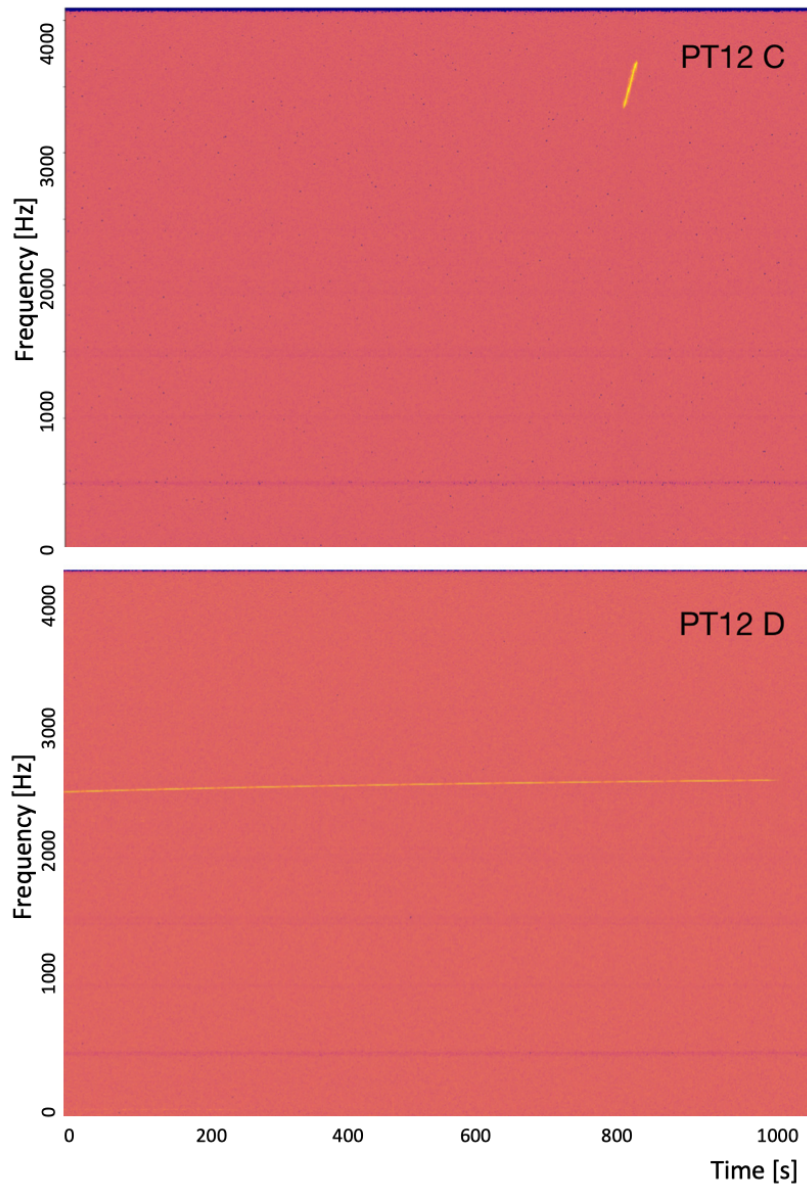


Figure 4.2: A representation of the PT-C and the PT-D waveforms in the time-frequency domain.

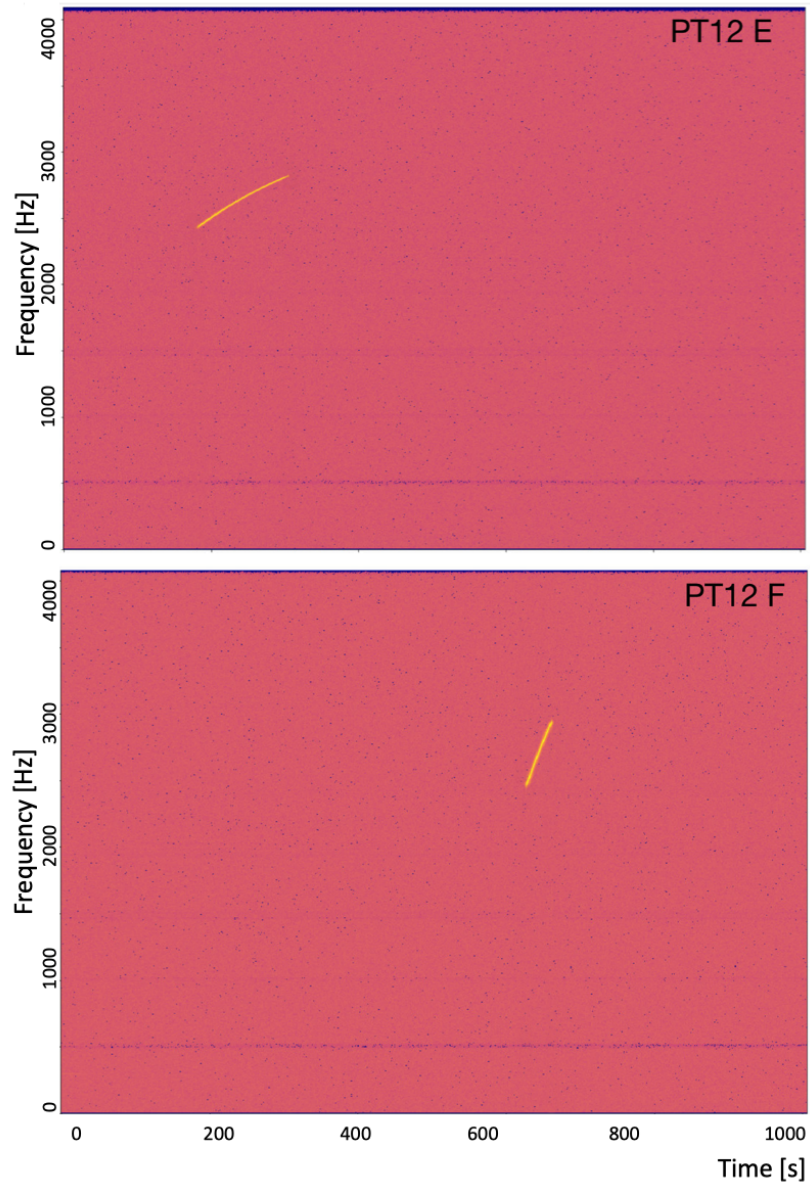


Figure 4.3: A representation of the PT-E and the PT-F waveforms in the time-frequency domain.

Waveform	Duration [s]	Frequency Min [Hz]	Frequency Max [Hz]
PT A	410	3194	3299
PT B	60	3280	3595
PT C	20	3308	3650
PT D	935	2430	2508
PT E	120	2448	2843
PT F	35	2448	2922

Figure 4.4: Duration and frequency range for each PT12 waveform.

4.3.2 Results and considerations

We present here the results of the analysis carried out, including the PT12 waveforms presented in 4.3. We start by showing the efficiency curves obtained from X-SphRad (see Figure 4.5, 4.6, 4.7). Here, we notice that for the

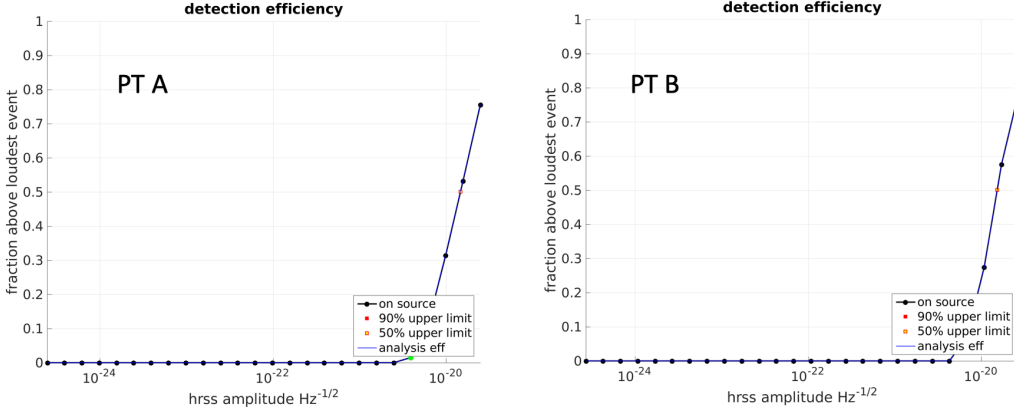


Figure 4.5: Detection efficiency curves of the PT12 waveforms given by the X-SphRad analysis. Fraction of injections recovered with significance greater than loudest event in (dummy) on-source. Black dots are sampled values, red and yellow dot is respectively the 90 % and 50 % efficiency obtained from interpolation. Green dots mark sampled values with $0 < \text{efficiency} < 5\%$. The blue curve shows the efficiency when DQ flags are not applied to injections. We obtain the 90 % upper limit from fit. Image and caption are taken from our webpage provides results from the analysis made using X-SphRad.

PT A, B, and C models, the fraction of injections recovered with a greater significance than the loudest event does not reach 100%. The false alarm rate is 1 event every 10 years.

Looking at the characteristics of the waveforms (see Figure 4.4), it is clear that the first three (PT A, B, C) have average frequencies above 3 kHz, contrary to the PT D, E, and F. We stress that the range of frequencies for the X-SphRad’s O1 and O2 analysis is between 24 and 2000 Hz [76, 77]. It leads to think that doubling the maximum frequency value, and consequently, the sampling frequency, may have produced problems in the detection efficiency. This observation is supported by the results obtained in the same analysis for the waveform models commonly used by X-SphRad for the long-signal

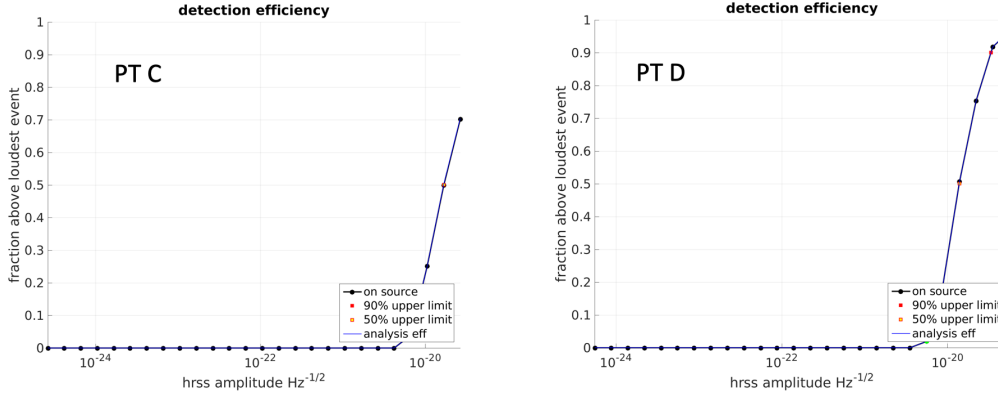


Figure 4.6: Detection efficiency curves of the PT12 waveforms given by the X-SphRad analysis. Fraction of injections recovered with significance greater than loudest event in (dummy) on-source. Black dots are sampled values, red and yellow dot is respectively the 90 % and 50 % efficiency obtained from interpolation. Green dots mark sampled valued with $0 < \text{efficiency} < 5\%$. The blue curve shows the efficiency when DQ flags are not applied to injections. We obtain the 90 % upper limit from fit. Image and caption are taken from our webpage provides results from the analysis made using X-SphRad.

burst searches in O1 and O2. The average frequency of these models is less than 1 kHz. Figure 4.9 shows an example of how the fraction of injections recovered with a significance greater than the loudest event reaches 100% for the waveform Line-B. All efficiency curves are shown in Appendix D.

A further observation is made for injection scales at 50% (see Figure 4.8). We can see how the PT12 waveforms have higher values in at least one order of magnitude than the waveforms commonly used. This means that PT12 waveforms must be very loud to be detected by the pipeline. The detector noise spectrum is directly proportional to the frequency for $f \geq 1\text{kHz}$. Consequently, the high values achieved by the corresponding SNR and the poor detection efficiency are not surprising. In conclusion, this preliminary work carried out with X-SphRad, which involves such waveforms describing a fallback accretion onto a NS, shows some interesting results. First of all, the difficulty of the pipeline to build a complete detection efficiency curve, which causes a lack of information on the 90% probability hrss. The reason could lie in the frequency range in which these waveforms are placed. In this analysis,

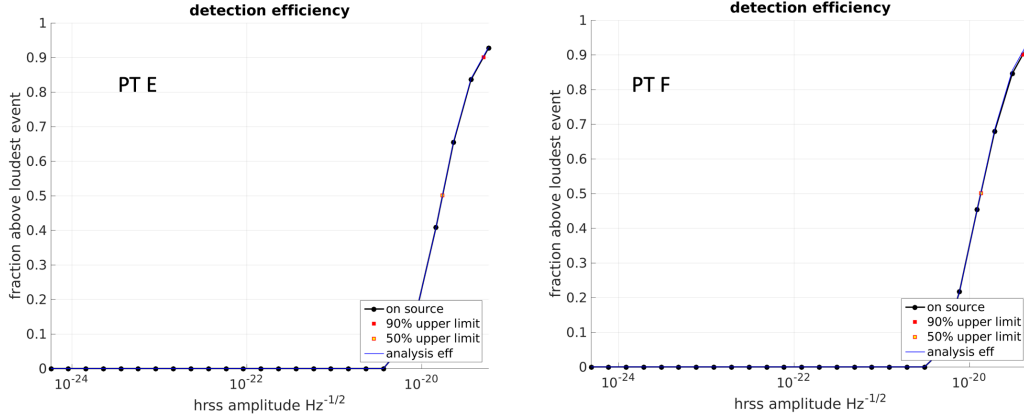


Figure 4.7: Detection efficiency curves of the PT12 waveforms given by the X-SphRad analysis. Fraction of injections recovered with significance greater than loudest event in (dummy) on-source. Black dots are sampled values, red and yellow dot is respectively the 90 % and 50 % efficiency obtained from interpolation. Green dots mark sampled values with $0 < \text{efficiency} < 5\%$. The blue curve shows the efficiency when DQ flags are not applied to injections. We obtain the 90 % upper limit from fit. Image and caption are taken from our webpage provides results from the analysis made using X-SphRad.

the minimum average frequency of the PT12 waveforms is about 2400 Hz, when typically X-SphRad works with a maximum frequency of 2000 Hz. Furthermore, X-SphRad can detect those with an injection scale in an order of magnitude higher than typical waveform models. This preliminary test on semi-analytical waveform models, describing astrophysical scenarios such as this collapsar ones, tells us why X-SphRad has better performance over frequency ranges of less than 3 kHz and that parameter affects the detection efficiency of the pipeline.

For completeness we have analysed an additional waveform, known as G19_LS220; LS220 indicates a different neutron star equations of state.

Jasmine Gill implemented and provided G19_LS220 waveform parameters (time, strain and frequency) to run a short analysis. G19_LS220 model is based on the PT12 one but has some changes on physical parameters. As the NS spins up, it becomes more oblate. This changes the radius at the equator, which changes the specific angular momentum of the accreted ma-

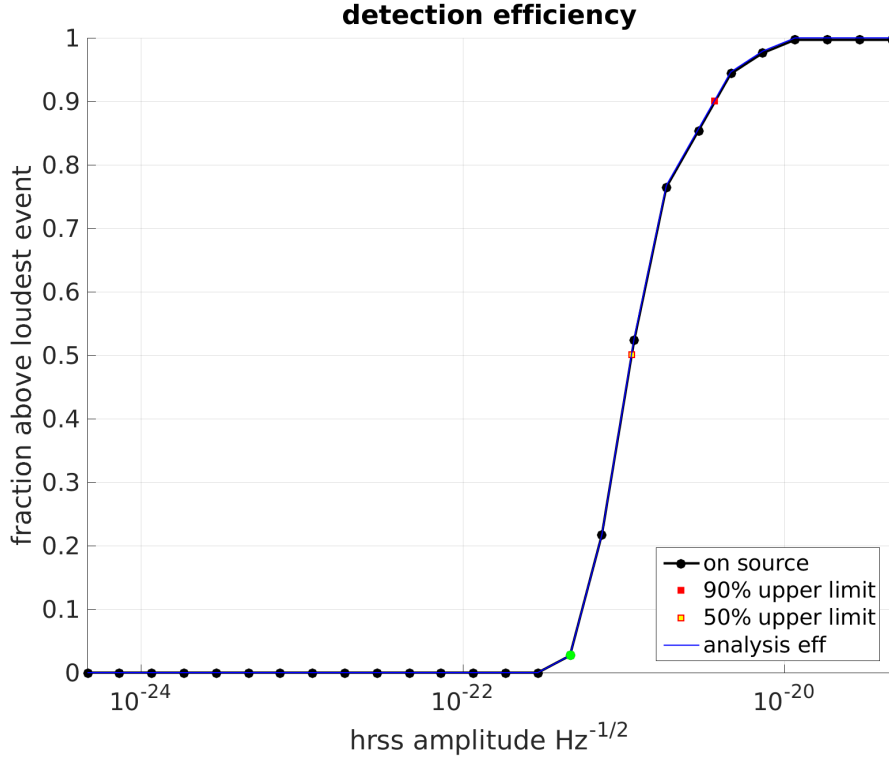


Figure 4.8: Detection efficiency curves of the Line B waveform given by the X-SphRad analysis. Fraction of injections recovered with significance greater than loudest event in (dummy) on-source. Black dots are sampled values, red and yellow dot is respectively the 90 % and 50 % efficiency obtained from interpolation. Green dots mark sampled values with $0 < \text{efficiency} < 5\%$. The blue curve shows the efficiency when DQ flags are not applied to injections. We obtain the 90 % upper limit from fit. Image and caption are taken from our webpage provides results from the analysis made using X-SphRad.

terial and the potential energy of the configuration [125]. Typical values of the quadrupole moment sufficient to balance the accretion torques are in the range $Q/MR^2 \sim [10^{-5}, 10^{-3}]$. Shape of the spun up NS becomes more bar-like (i.e. accretion is inhibited). The G19_LS220 waveform analysed here has an initial mass of $2 M_{\odot}$, $\beta_c = 0.14$, and a frequency range $\sim [2700, 3500] Hz$ with a duration of about 30 seconds.

The background is the same of the PT12 analysis, with a FAR of 1/10 years.

Figure 4.9 shows the detection efficiency curve of G19_LS220 produced by X-SphRad. The fraction of injections recovered with a greater significance than the loudest event does reach 100%, contrarily to what happens with PT12s. We want to note how the pipeline managed to complete the analysis despite the fact that we are in a range of frequencies still to be explored, without forgetting that G19_LS220 is an analysis made on a single waveform, corresponding to a theoretical model different from the previous one.

Figure 4.10 shows the effective distance reached by X-SphRad analysing PT12 waveforms. A paper on long-lived gravitational-wave transients reports long GRBs distance lower limits of 1.9-33 Mpc [126] while, the paper on the collapsar scenario and the production of GWs stated that LIGO may be able to detect such sources within 100 Mpc [72]. We also show the hrss (50%) values against the noise power spectral density in Figure 4.11.

Understanding the way to improve the pipeline settings, in order to increase the frequency range, needs further investigations. Future work to explore the performance of X-SphRad at higher frequency should consider the TF volume of the signal and examine whenever the pipeline is recovering all of the injection or just a part. It would be, in fact, interesting to repeat the analysis including louder injections and see if X-SphRad is able to reconstruct the detection efficiency curves in full for the PT12 waveforms.

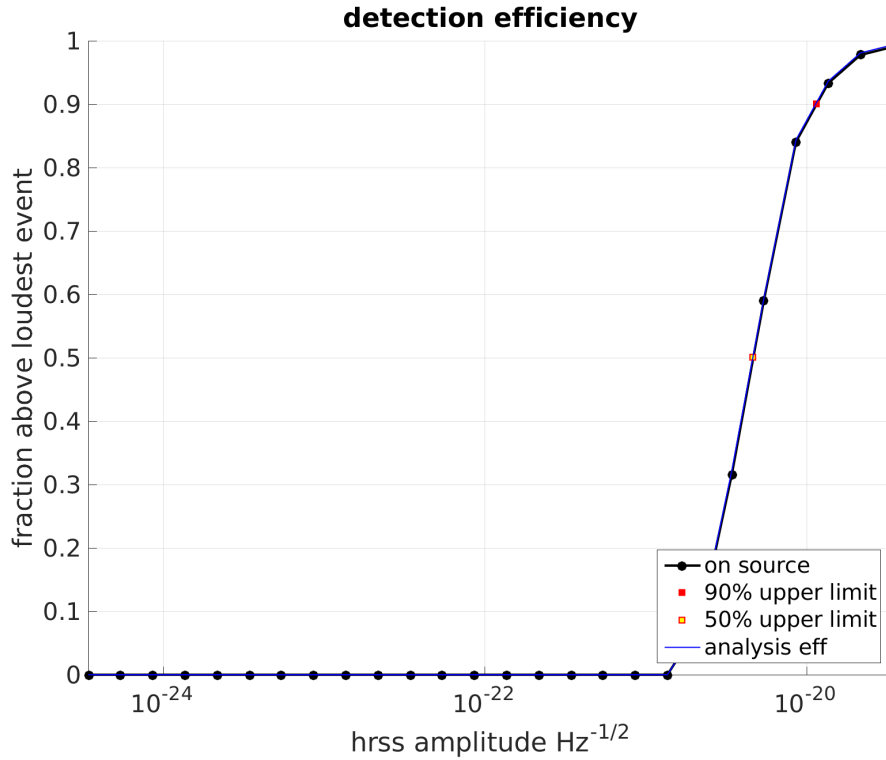


Figure 4.9: Detection efficiency curves of the G19LS220 waveform given by X-SphRad analysis. Fraction of injections recovered with significance greater than loudest event in (dummy) on-source. Black dots are sampled values, red and yellow dot is respectively the 90 % and 50 % efficiency obtained from interpolation. Green dots mark sampled valued with $0 < \text{efficiency} < 5$ %. The blue curve shows the efficiency when DQ flags are not applied to injections. We obtain the 90 % upper limit from fit. Image and caption are taken from our webpage provides results from the analysis made using X-SphRad.

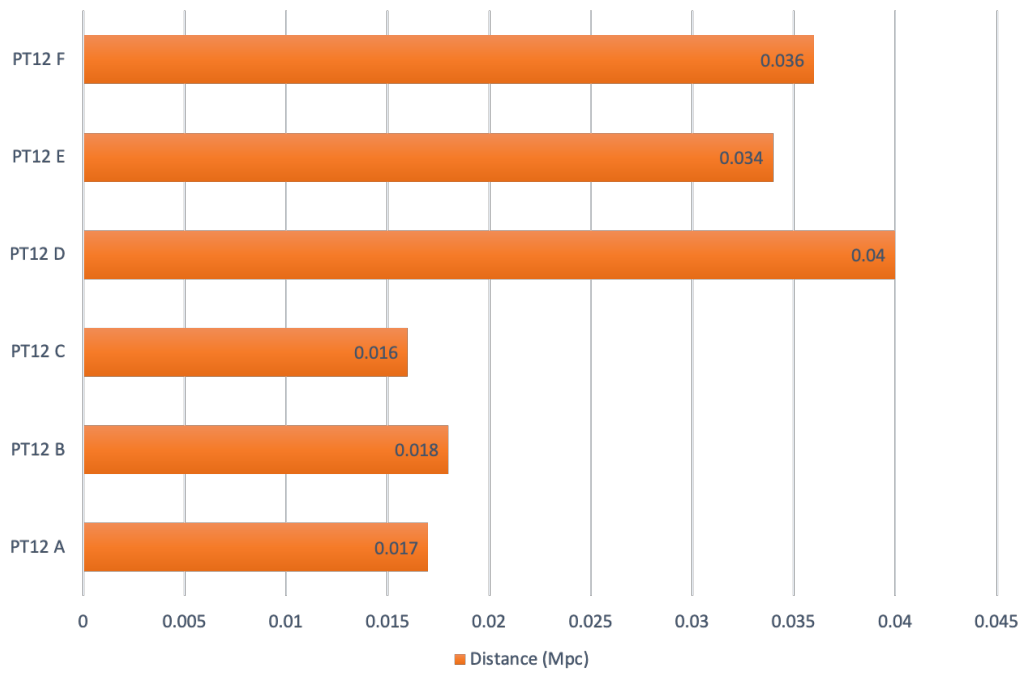


Figure 4.10: Effective distance reached by the X-SphRad for PT12 waveforms, with the 50 % of detection probability.

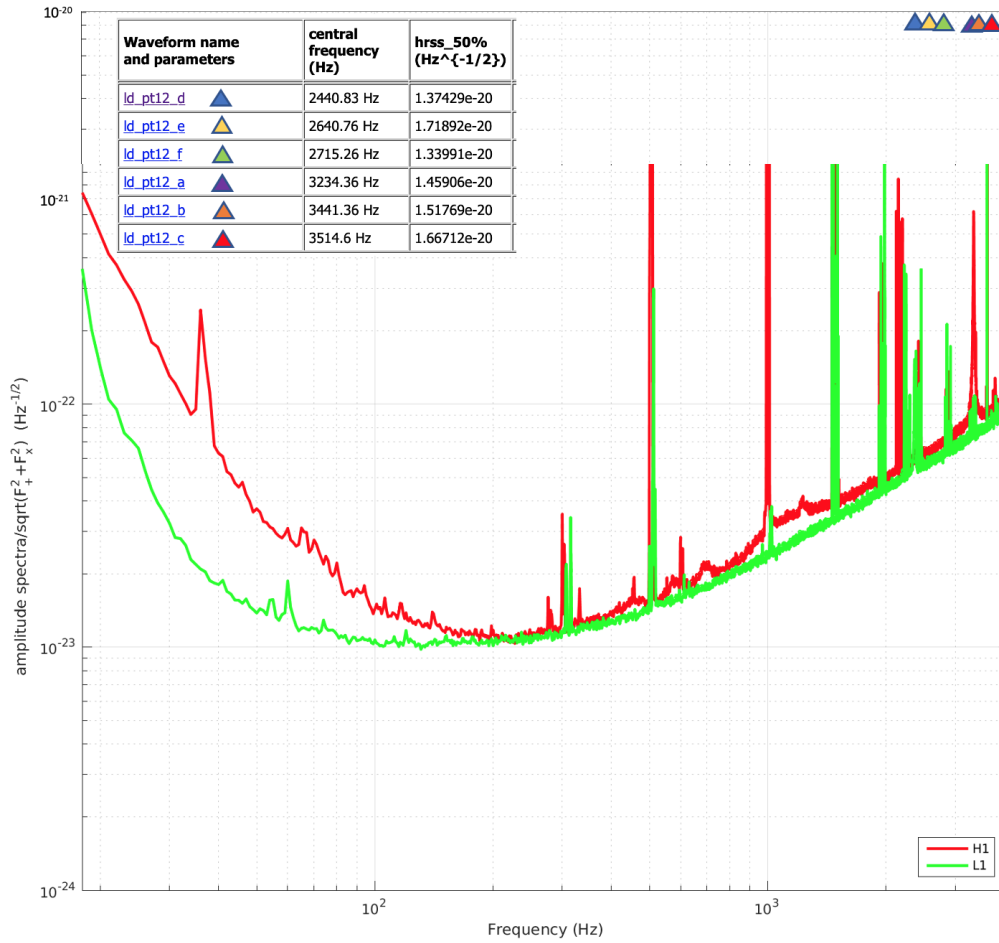


Figure 4.11: The noise amplitude spectra curves for both Hanford and Livingston are shown alongside with gravitational-wave strain versus frequency for PT12 waveforms detected with 50 % efficiency and a false alarm rate of 1 event in 10 years.

Chapter 5

Conclusion

Non-Gaussian, non-stationary noise ‘glitches’ in LIGO interferometers have several detrimental effects on experiments. From an analysis perspective, loud interferometer glitches can mimic gravitational wave signals. Our experience is that these glitches can be the loudest events in analysed data. They therefore influence, firstly, the threshold placed on signals to be considered events, and, secondly, the upper limits resulting from loudest event analyses of searches deemed not to have identified any coincident physical signals. Thus, efficient removal of interferometer glitches is a key goal in LIGO analysis. This thesis has addressed this through the development of the SHaVeD algorithm as a glitch rejection tool.

Long-duration bursts, signals with a duration of between 10 seconds to a few minutes, are one of the research targets impacted by these limitations. Several tools, in gravitational wave analysis, perform long-duration burst-like signal searches. In this Ph.D. thesis we compared different analyses carried out by The X-Pipeline Spherical Radiometer (X-SphRad) and the coherent WaveBursts (cWB) pipeline, on data provided by LIGO detectors during the O2 observing run. cWB uses maximum-likelihood to identify excess power in coincident events in the time-frequency space, while X-SphRad uses coherent sky energy. X-SphRad aims to perform a fast all-sky search working in the spherical harmonic domain. Previous studies investigated the capabilities of the spherical harmonic coefficients in discriminating glitches from signals.

In this work we developed and tested a method that exploits this potential. Identification and rejection of glitches, that contaminate data, aims to improve the detection efficiency of gravitational-wave signals. The Spherical Harmonic Veto Definer (SHaVeD) can be described as a tool for identifying interferometer glitches, and for differentiating between these glitches and genuine whole-network detections of physical signals through their different responses in a spherical harmonic decomposition of the detector data.

Glitches do not come from a particular position in the sky and so do not have a preferred delay, then they appear mainly in the zero-th order (C_{00}). We used that information to identify glitches within a frame (data segment). We started considering the sum of coefficients with higher orders ($C_{lm} > C_{00}$) calculated over each bin on the time axis. We created a function, named ‘Ratio’, representing the ratio between C_{lm} coefficients and C_{00} . We expect minimum peaks when glitches occur, since their most significant contribution is in the zero-th order.

We developed a script able to study statistically the Ratio function to calculate thresholds, which allowed rejection of bins affected by glitches. Each frame is characterised by a GPS starting time, and each bin has a size of 0.5 second. With this knowledge, it is possible to lead back to the GPS time of each glitch. After identification of the corresponding GPS times, the algorithm creates a 1 second-long cut around the glitch GPS time. The script then saves times to cut in a file, that can be used by pipelines as data quality.

In this Ph.D. thesis we produced SHaVeD files for the last month (July-August 2017) of the O2 observing run. SHaVeD has been included as data quality in cWB and we evaluated its impact with several analyses. Specifically, we performed two different studies. At first, SHaVeD is applied in the pre-processing stage of the analysis, where clusters of pixels for analysis have not yet been selected. Notice that, cWB has its own veto file, called gating, which has been compared with SHaVeD. The results show how the addition of a cut such as SHaVeD, in the pre-processing stages should be well-calibrated according to the performance obtained independently from the pipeline. For cWB, this would mean excluding 7 hours more from the analysis. The benefit of excluding further data needs to be carefully evaluated and proportionate

to the goals to be achieved.

However, SHaVeD shows promise because it has been seen to eliminate the loudest events resulting from the cWB analysis. Should further studies indicate that this is borne out by analysis of larger data sets, it would indicate that the SHaVeD veto could profitably be added to the pre-production selection of data segments, with a commensurate increase in sensitivity.

In the second phase of the study, we analysed SHaVeD as data quality in the post-processing stage, that is when the GW candidate event list has already been generated. We performed several tests to compare SHaVeD with cWB data quality. The results obtained demonstrate the capability of SHaVeD to veto background events that would otherwise contaminate the analysis.

The analysis with SHaVeD was also performed on the event generated by the merger of two neutron stars (GW170817), which was affected by a glitch, specifically the data from the LIGO-Livingston detector. In this case, the test involved the application of SHaVeD in the pre-processing stage and before the cWB whitening stage. Results show how SHaVeD was able to mitigate the loud glitch and make cWB reconstruct the last second of the BNS inspiral phase.

For completeness, we tested SHaVeD for part of the O3 observing run, currently still in progress. Specifically, we analysed 19 days of coincident data with cWB. The results indicates that SHaVeD was highly effective in identifying and therefore vetoing the glitches present in the analysed data. It is important to note that at the time of the analysis, approved data quality were not available and further analyses are ongoing.

Finally, as an additional analysis carried out in this project, six different waveforms, named PT12, were injected into X-SphRad and analysed as simulated signals. The analysis aimed to evaluate the performance of the pipeline in a higher frequency range and on astrophysics waveforms. This preliminary analysis showed that X-SphRad performed better over frequency ranges of less than 3 kHz and that this parameter affected the detection efficiency of the pipeline.

Appendix A

Spherical harmonic coefficients order

m value of row	coefficients stored as (l, m) pairs
$m=0$	$(0, 0), (1, 0), (2, 0), (3, 0), \dots, (l_{\max}, 0)$
$m=1$	$(1,+1), (2,+1), (3,+1), \dots, (l_{\max},+1)$
$m=2$	$(2,+2), (3,+2), \dots, (l_{\max},+2)$
$m=3$	$(3,+3), \dots, (l_{\max},+3)$
\vdots	\vdots
$m=l_{\max}$	$(l_{\max},+l_{\max})$
$m=-l_{\max}$	$(l_{\max},-l_{\max})$
\vdots	\vdots
$m=-3$	$(3,-3), \dots, (l_{\max},-3)$
$m=-2$	$(2,-2), (3,-2), \dots, (l_{\max},-2)$
$m=-1$	$(1,-1), (2,-1), (3, -1), \dots, (l_{\max},-1)$

Figure A.1: Spherical harmonic coefficients order, expressed as (l, m) pairs, read left to right and top to bottom[32].

This ordering is the same as used in the S2Kit [55].

Appendix B

cWB and X-SphRad detection efficiency curves

All the eight waveform types we injected into the cWB and X-SphRad pipelines are shown below. As explained in Section 2.5, both pipelines injected the same waveforms at different scales. It is done to assess the probability of detection as a function of the energy of gravitational waves. At the end of each analysis, both pipelines provided the values of the signal amplitude, $hrss$, (see Equation 2.14) corresponding to the signal detection probability of 50% and 90% respectively.

APPENDIX B. CWB AND X-SPHRAD DETECTION EFFICIENCY CURVES

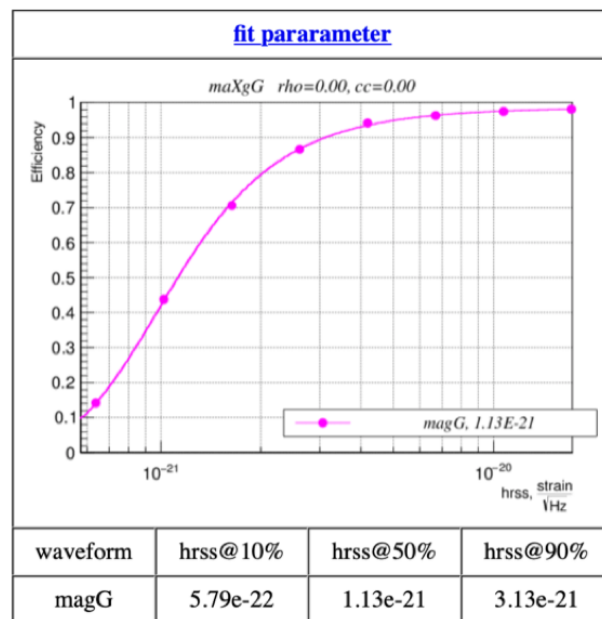


Figure B.1: Example of a detection efficiency plot of a waveform injected into cWB. The caption reports the waveform type, the value of the hrss value for a detection probability of the 10, 50 and 90 %.

APPENDIX B. CWB AND X-SPHRAD DETECTION EFFICIENCY CURVES

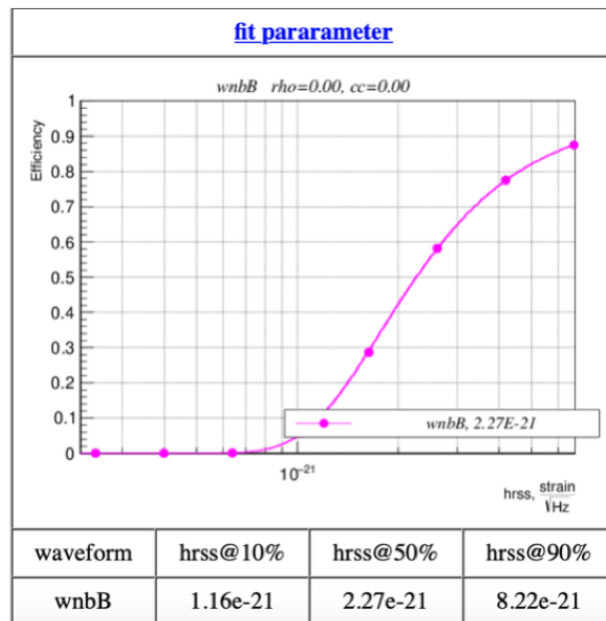


Figure B.2: Example of a detection efficiency plot of a waveform injected into cWB. The caption reports the waveform type, the value of the hrss value for a detection probability of the 10, 50 and 90 %.

APPENDIX B. CWB AND X-SPHRAD DETECTION EFFICIENCY CURVES

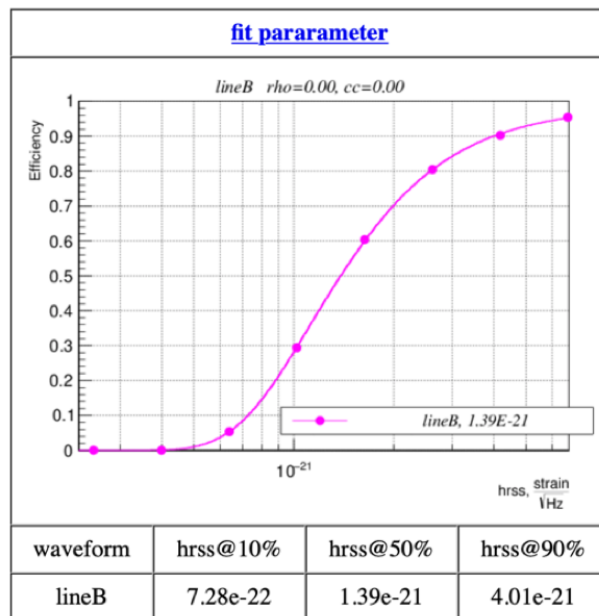
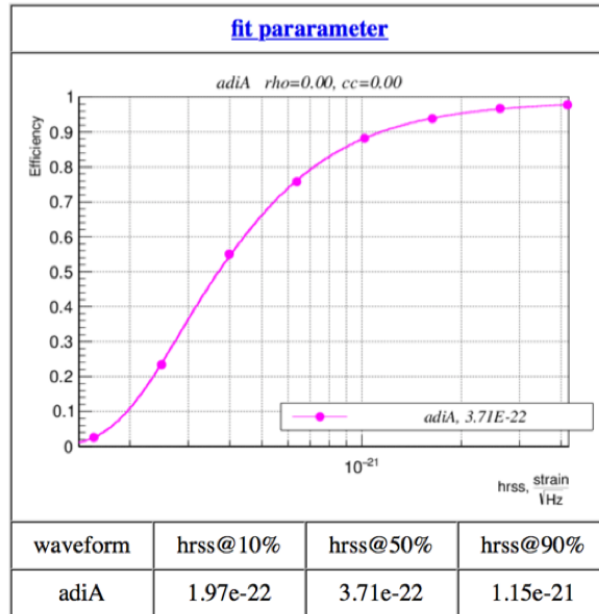


Figure B.3: Example of a detection efficiency plot of a waveform injected into cWB. The caption reports the waveform type, the value of the hrss value for a detection probability of the 10, 50 and 90 %.

APPENDIX B. CWB AND X-SPHRAD DETECTION EFFICIENCY CURVES

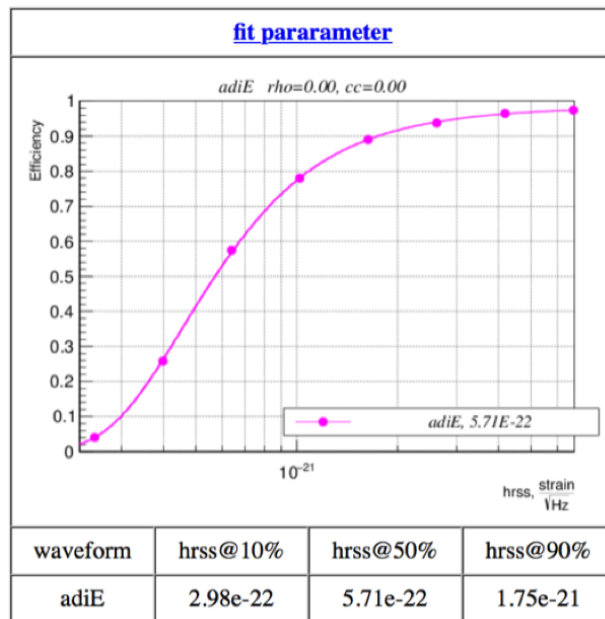
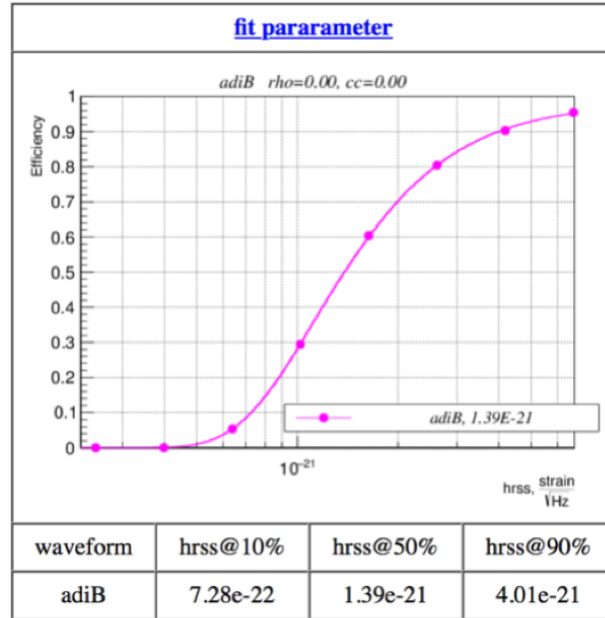


Figure B.4: Example of a detection efficiency plot of a waveform injected into cWB. The caption reports the waveform type, the value of the hrss value for a detection probability of the 10, 50 and 90 %.

APPENDIX B. CWB AND X-SPHRAD DETECTION EFFICIENCY CURVES

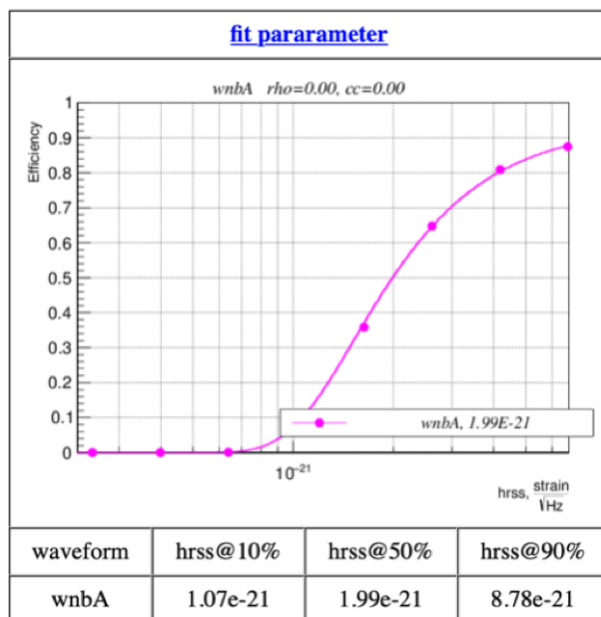
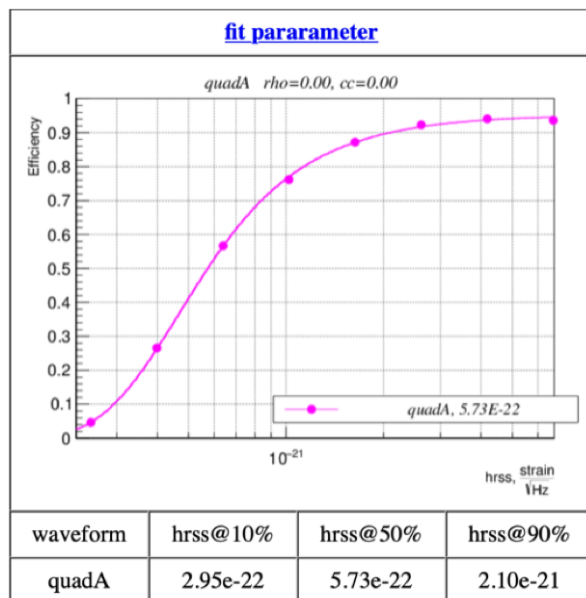


Figure B.5: Example of a detection efficiency plot of a waveform injected into cWB. The caption reports the waveform type, the value of the hrss value for a detection probability of the 10, 50 and 90 %.

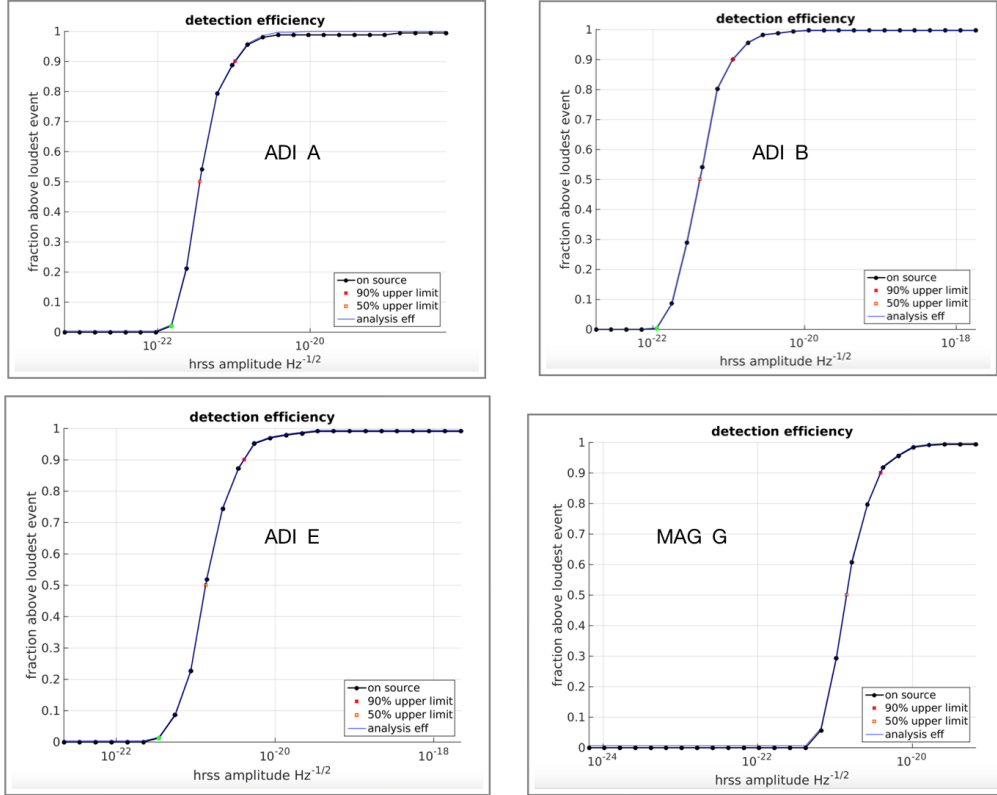


Figure B.6: Example of a detection efficiency plot of a waveform injected into X-SphRad. Fraction of injections recovered with significance greater than loudest event in (dummy) on-source. Black dots are sampled values, red and yellow dots are respectively the 90 % and 50 % efficiency obtained from interpolation. Green dots mark sampled values with $0 < \text{efficiency} < 5\%$. The blue curve shows the efficiency when DQ flags are not applied to injections. Image and caption are taken from our webpage to provide results from the analysis made using X-SphRad.

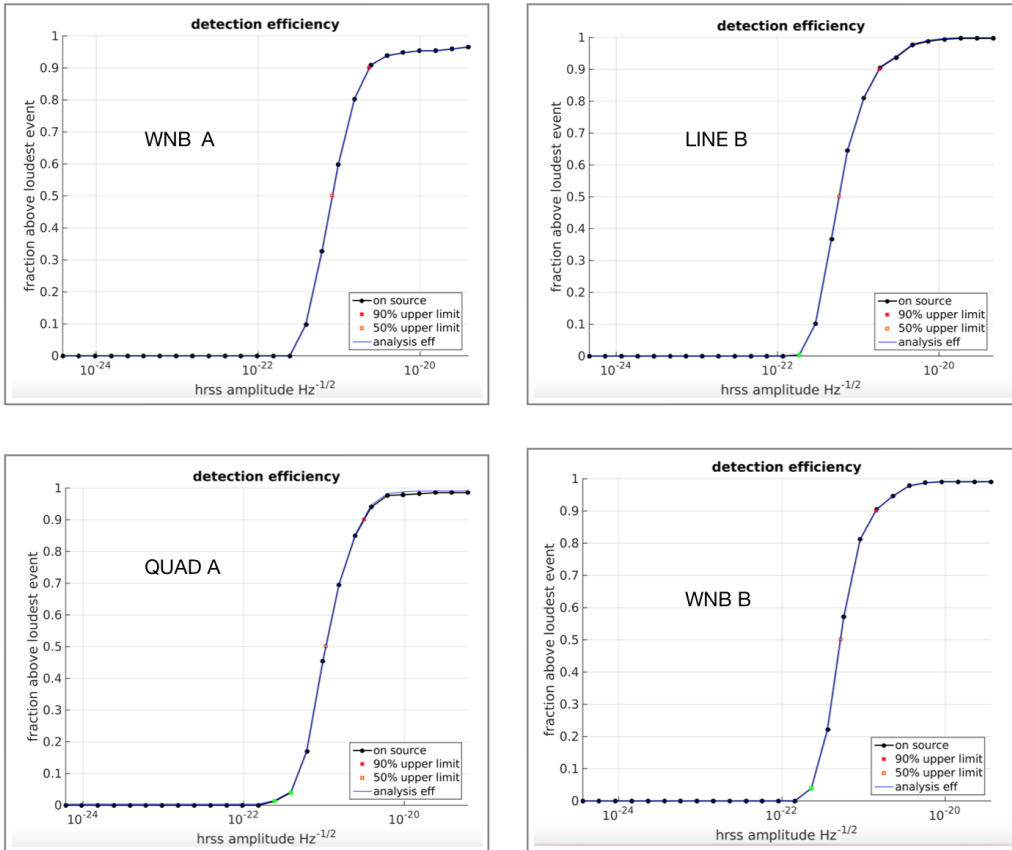


Figure B.7: Example of a detection efficiency plot of a waveform injected into X-SphRad. Fraction of injections recovered with significance greater than loudest event in (dummy) on-source. Black dots are sampled values, red and yellow dots are respectively the 90 % and 50 % efficiency obtained from interpolation. Green dots mark sampled valued with $0 < \text{efficiency} < 5$ %. The blue curve shows the efficiency when DQ flags are not applied to injections. Image and caption are taken from our webpage to provide results from the analysis made using X-SphRad.

Appendix C

Matlab SHaVeD script

```
%Path to the files (DUMP) to recover C00 and Clm
file_list=dir([dir_name file_name_root '*DUMP*.mat'])
n_files=length(file_list);
%Procedure is done every 500 frames due to computational costs
for i=1:500;
load([dir_name file_list(i).name]);
gps_char=char(file_list(i).name);
gps_str=convertCharsToStrings(gps_char);
gps_num= extractBetween(gps_str,"-","-");
%gps starting time of each data frame
gps_start = str2double(gps_num);
% Time-Frequency map
tfmap=fast_tfmap;
% Time-Spherical Harmonic map
tsmap=full_tsmap;
%Zero-th component of the SH coefficients
pippo00= abs(tsmap(1,:));
%Non-zero component of the SH coefficients
pippolm=abs(tsmap);
%Sum Clm over each bin
E_bin=sum(pippolm,1);
```

```
%Function R=Clm/C00
ratio=E_bin'./pippo00';
%Mean of the ratio value
m=mean(ratio);
%Standard deviation of the ratio value
s=std(ratio);
%Threshold depends on the percentage we want to discard
T=m-(2.32)*s;
%Identification of indexes corresponding to
%bins positions that fall below the threshold
idx=find(ratio<T);
idx_0=idx-1.;
%Identification of the GPS times corresponding to these indexes
veto=gps_start+4+(idx_0./2);
veto_full=[veto_full;veto];
veto_start=veto_full-0.5;
veto_end=veto_full+0.5;
%Range of values to veto
C=[veto_start,veto_end];
end
start=unique(veto_start,'rows');
End=unique(veto_end,'rows');
for k=1:length(start)-1
if start(k+1) <= End(k);
End(k) = End(k) + 0.5;
end
%File of SHaVeD generated
v_file=[start,End];
end
dlmwrite('v_file_O3_500.txt',v_file)
```

Appendix D

PT12 waveforms detection efficiency curves

During the PT12 analysis, discussed in Chapter 4, we also included several ad-hoc waveforms. The corresponding detection efficiency curves are shown below.

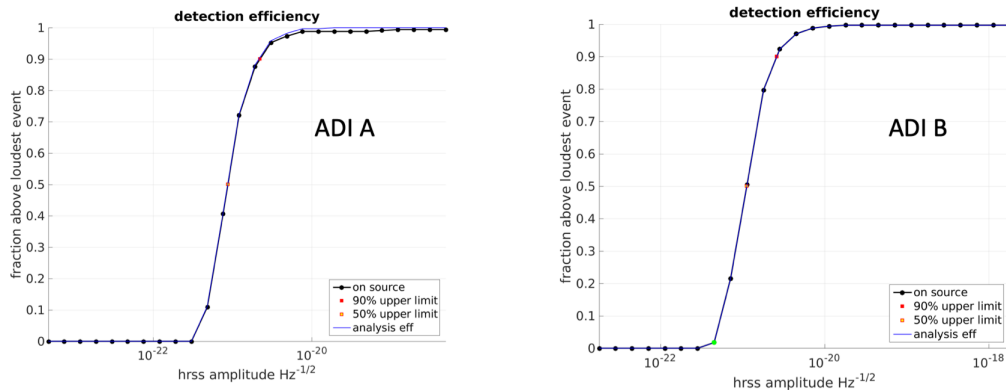


Figure D.1: Detection efficiency curves of ad-hoc waveforms included in the PT12 waveforms X-SphRad analysis. Fraction of injections recovered with significance greater than loudest event in (dummy) on-source. Black dots are sampled values, red and yellow dots are respectively the 90 % and 50 % efficiency obtained from interpolation. Green dots mark sampled values with $0 < \text{efficiency} < 5\%$. The blue curve shows the efficiency when DQ flags are not applied to injections. Image and caption are taken from our webpage to provide results from the analysis made using X-SphRad.

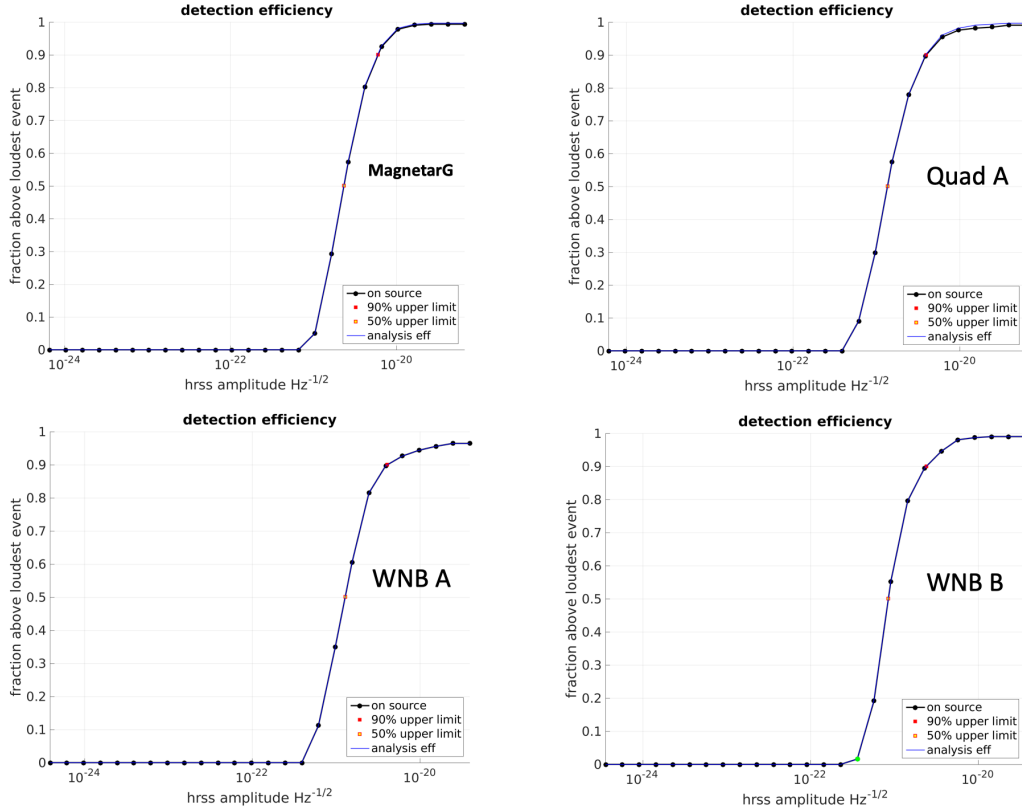


Figure D.2: Detection efficiency curves of ad-hoc waveforms included in the PT12 waveforms X-SphRad analysis. Fraction of injections recovered with significance greater than loudest event in (dummy) on-source. Black dots are sampled values, red and yellow dots are respectively the 90 % and 50 % efficiency obtained from interpolation. Green dots mark sampled valued with $0 < \text{efficiency} < 5\%$. The blue curve shows the efficiency when DQ flags are not applied to injections. Image and caption are taken from our webpage to provide results from the analysis made using X-SphRad.

APPENDIX D. PT12 WAVEFORMS DETECTION EFFICIENCY CURVES

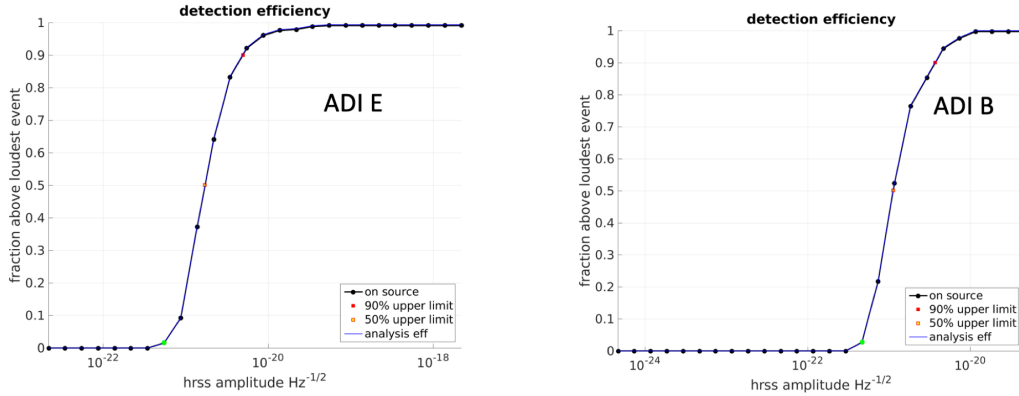


Figure D.3: Detection efficiency curves of ad-hoc waveforms included in the PT12 waveforms X-SphRad analysis. Fraction of injections recovered with significance greater than loudest event in (dummy) on-source. Black dots are sampled values, red and yellow dots are respectively the 90 % and 50 % efficiency obtained from interpolation. Green dots mark sampled valued with $0 < \text{efficiency} < 5\%$. The blue curve shows the efficiency when DQ flags are not applied to injections. Image and caption are taken from our webpage to provide results from the analysis made using X-SphRad.

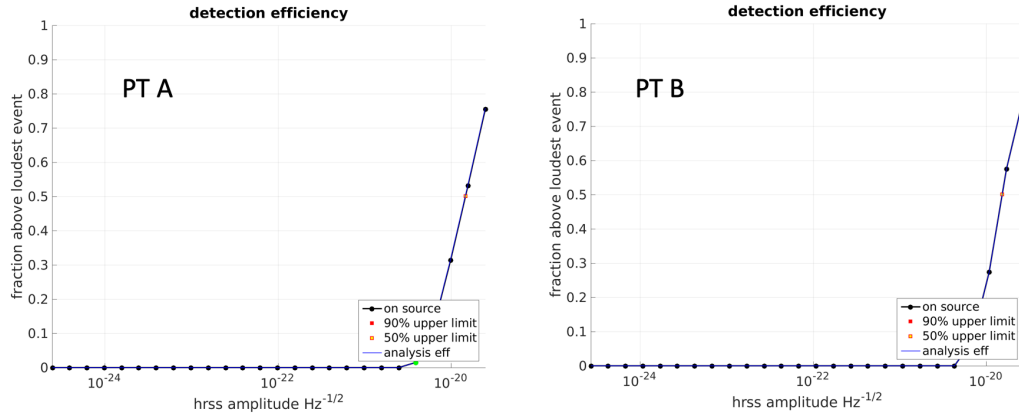


Figure D.4: Detection efficiency curves of ad-hoc waveforms included in the PT12 waveforms X-SphRad analysis. Fraction of injections recovered with significance greater than loudest event in (dummy) on-source. Black dots are sampled values, red and yellow dots are respectively the 90 % and 50 % efficiency obtained from interpolation. Green dots mark sampled valued with $0 < \text{efficiency} < 5\%$. The blue curve shows the efficiency when DQ flags are not applied to injections. Image and caption are taken from our webpage to provide results from the analysis made using X-SphRad.

APPENDIX D. PT12 WAVEFORMS DETECTION EFFICIENCY CURVES

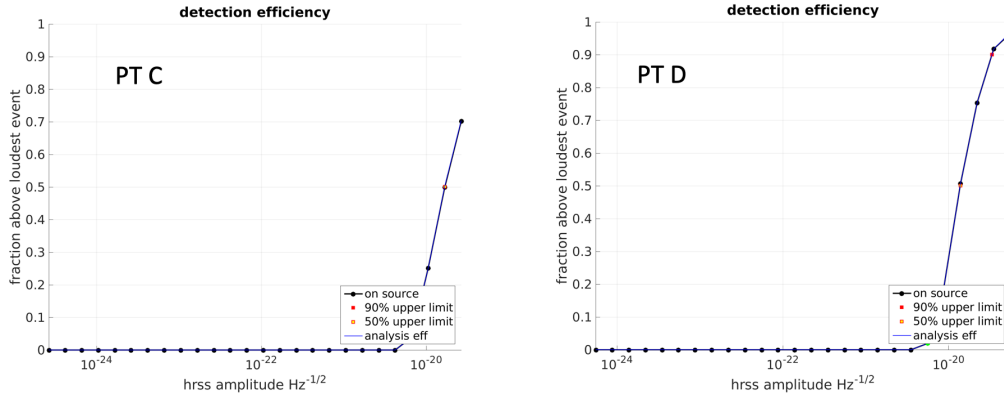


Figure D.5: Detection efficiency curves of ad-hoc waveforms included in the PT12 waveforms X-SphRad analysis. Fraction of injections recovered with significance greater than loudest event in (dummy) on-source. Black dots are sampled values, red and yellow dots are respectively the 90 % and 50 % efficiency obtained from interpolation. Green dots mark sampled values with $0 < \text{efficiency} < 5\%$. The blue curve shows the efficiency when DQ flags are not applied to injections. Image and caption are taken from our webpage to provide results from the analysis made using X-SphRad.

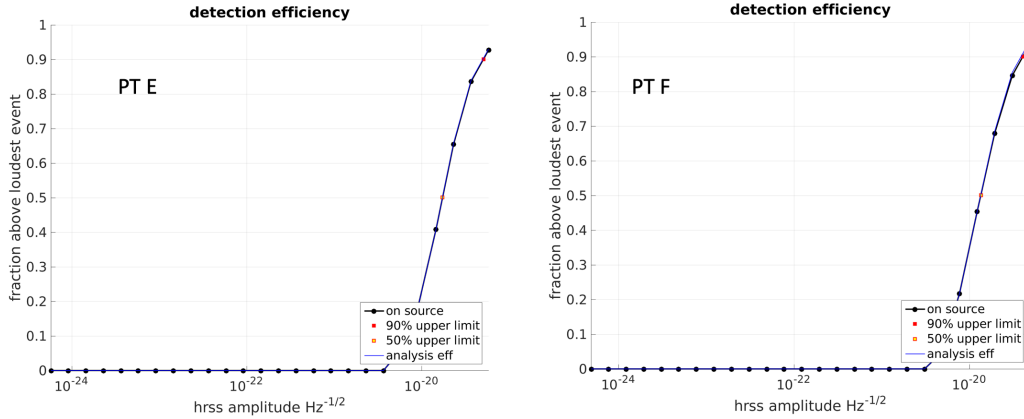


Figure D.6: Detection efficiency curves of ad-hoc waveforms included in the PT12 waveforms X-SphRad analysis. Fraction of injections recovered with significance greater than loudest event in (dummy) on-source. Black dots are sampled values, red and yellow dots are respectively the 90 % and 50 % efficiency obtained from interpolation. Green dots mark sampled values with $0 < \text{efficiency} < 5\%$. The blue curve shows the efficiency when DQ flags are not applied to injections. Image and caption are taken from our webpage to provide results from the analysis made using X-SphRad.

Bibliography

- [1] Einstein, A. (1923). Die grundlage der allgemeinen relativitätstheorie. In *Das Relativitätsprinzip* (pp. 81-124). Vieweg+ Teubner Verlag, Wiesbaden.
- [2] Schutz, B. (2009). *A first course in general relativity*. Cambridge university press.
- [3] Ferrari, V. (2013). *Notes on General Relativity*. Univerisity of Rome “Sapienza” press.
- [4] Blanchet, L. (2014). Gravitational radiation from post-Newtonian sources and inspiralling compact binaries. *Living Reviews in Relativity*, 17(1), 2
- [5] Abbott, B. P., Abbott, R., Abbott, T. D., Abernathy, M. R., Acernese, F., Ackley, K., ... & Adya, V. B. (2016). Observation of gravitational waves from a binary black hole merger. *Physical review letters*, 116(6), 061102.
- [6] Lasky, P. D. (2015). *Gravitational waves from neutron stars: a review*. Publications of the Astronomical Society of Australia, 32.
- [7] Pierro, V., Pinto, I. M., Principe, M., & LVC Collaboration. (2014). Gravitational waves from known pulsars: results from the initial detector era.
- [8] Hulse, R. A., & Taylor, J. H. (1975). Discovery of a pulsar in a binary system. *The Astrophysical Journal*, 195, L51-L53.

- [9] Sigg D. (2009). Gravitational waves. LIGO-P980007-00-D.
- [10] Costa, E., & Frontera, F. (2011). Gamma-Ray Bursts origin and their afterglow: Story of a discovery and more. *La Rivista del Nuovo Cimento*, 34, 585-615.
- [11] Ryden B. (2003). *An introduction to cosmology*. Addison Wesley.
- [12] Barish, B. C., & Weiss, R. (1999). LIGO and the detection of gravitational waves. *Physics Today*, 52, 44-50.
- [13] Accadia, T., Acernese, F., Alshourbagy, M., Amico, P., Antonucci, F., Aoudia, S., ... & Avino, S. (2012). Virgo: a laser interferometer to detect gravitational waves. *Journal of Instrumentation*, 7(03), P03012.
- [14] Willke, B., Aufmuth, P., Aulbert, C., Babak, S., Balasubramanian, R., Barr, B. W., ... & Churches, D. (2002). The GEO 600 gravitational wave detector. *Classical and Quantum Gravity*, 19(7), 1377.
- [15] Harry, G. M. (2010). GM Harry and the LIGO Scientific Collaboration, *Classical Quantum Gravity* 27, 084006 (2010). *Classical Quantum Gravity*, 27, 084006.
- [16] Corsi, A., & Mészáros, P. (2009). Gamma-ray burst afterglow plateaus and gravitational waves: Multi-messenger signature of a millisecond magnetar?. *The Astrophysical Journal*, 702(2), 1171.
- [17] Gualtieri, L., Ciolfi, R., & Ferrari, V. (2011). Structure, deformations and gravitational wave emission of magnetars. *Classical and Quantum Gravity*, 28(11), 114014.
- [18] Metzger, B. D., Giannios, D., Thompson, T. A., Bucciantini, N., & Quataert, E. (2011). The protomagnetar model for gamma-ray bursts. *Monthly Notices of the Royal Astronomical Society*, 413(3), 2031-2056.
- [19] Rowlinson, A. (2013). O, Brien, PT, Metzger, BD, Tanvir, NR, & Levan.

- [20] van Putten, M. H. (2001). Proposed source of gravitational radiation from a torus around a black hole. *Physical review letters*, 87(9), 091101.
- [21] Ott, C. D., Ou, S., Tohline, J. E., & Burrows, A. (2005). One-armed spiral instability in a low- $T/|W|$ postbounce supernova core. *The Astrophysical Journal Letters*, 625(2), L119.
- [22] Piro, A. L., & Thrane, E. (2012). Gravitational waves from fallback accretion onto neutron stars. *The Astrophysical Journal*, 761(1), 63.
- [23] Coughlin, S. B., Dooley, K., Fairhurst, S., Fays, M., Grote, H., Hannam, M., ... & Pannarale Greco, F. (2016). All-sky search for long-duration gravitational wave transients with initial LIGO. *Physical Review D*, 93(4).
- [24] Klimentenko, S., Vedovato, G., Drago, M., Salemi, F., Tiwari, V., Prodi, G. A., ... & Mitselmakher, G. (2016). Method for detection and reconstruction of gravitational wave transients with networks of advanced detectors. *Physical Review D*, 93(4), 042004.
- [25] Cannon, K. C. (2007). Efficient algorithm for computing the time-resolved full-sky cross power in an interferometer with omnidirectional elements. *Physical Review D*, 75(12), 123003.
- [26] Sutton, P. J., Jones, G., Chatterji, S., Kalmus, P., Leonor, I., Poprocki, S., ... & Was, M. (2010). X-pipeline: an analysis package for autonomous gravitational-wave burst searches. *New Journal of Physics*, 12(5), 053034.
- [27] Edwards, M. (2013). On the search for intermediate duration gravitational waves using the spherical harmonic basis (Doctoral dissertation, Cardiff University).
- [28] Chatterji, S., Lazzarini, A., Stein, L., Sutton, P. J., Searle, A., & Tinto, M. (2006). Coherent network analysis technique for discriminating gravitational-wave bursts from instrumental noise. *Physical Review D*, 74(8), 082005.

- [29] Gürsel, Y., & Tinto, M. (1989). Near optimal solution to the inverse problem for gravitational-wave bursts. *Physical Review D*, 40(12), 3884.
- [30] Fays, M. (2017). Exploring long duration gravitational-wave transients with second generation detectors (Doctoral dissertation, Cardiff University).
- [31] Chatterji, S., Blackburn, L., Martin, G., & Katsavounidis, E. (2004). *Classical Quantum Gravity* 21. S1809, 48.
- [32] Kennedy, R. (2018). Line tracking applications for Gravitational Wave data and searching for long-duration burst signals (Doctoral dissertation, University of Sheffield).
- [33] Press, W. H., Teukolsky, S. A., Vetterling, W. T., & Flannery, B. P. (1986). *Numerical recipes in Fortran* 77.
- [34] Sutton, P., Daw E., Mark Edwards, Was, M. (2015). X-Pipeline All-Sky Burst Search: Optimisation. LIGO-T1500033-v1
- [35] Sylvestre, J. (2002). Time-frequency detection algorithm for gravitational wave bursts. *Physical Review D*, 66(10), 102004.
- [36] Arabie, P., & De Soete, G. (1996). *Clustering and classification*. World Scientific.
- [37] Abbott, B., Abbott, R., Adhikari, R., Ageev, A., Allen, B., Amin, R., ... & Asiri, F. (2004). First upper limits from LIGO on gravitational wave bursts. *Physical Review D*, 69(10), 102001.
- [38] Edwards, M., & Sutton, P. J. (2012). A new glitch-rejection algorithm forged in the spherical harmonic basis. In *Journal of Physics: Conference Series* (Vol. 363, No. 1, p. 012025). IOP Publishing.
- [39] Chow, J., Chua, S., Inta, R., Lam, P. K., McClelland, D., Miller, J., ... & Zhao, C. (2012). Search for gravitational waves associated with

- gamma-ray bursts during Ligo science run 6 and Virgo science runs 2 and 3.
- [40] Coherent Wave Burst homepage. URL: <https://www.atlas.aei.uni-hannover.de/wave-burst/LSC/doc/cwb/man>.
- [41] Klimenko, S., Yakushin, I., Mercer, A., & Mitselmakher, G. (2008). A coherent method for detection of gravitational wave bursts. *Classical and Quantum Gravity*, 25(11), 114029.
- [42] ROOT homepage. URL: <https://root.cern.ch/>.
- [43] Tiwari, V., Drago, M., Frolov, V., Klimenko, S., Mitselmakher, G., Necula, V., ... & Yakushin, I. (2015). Regression of environmental noise in LIGO data. *Classical and Quantum Gravity*, 32(16), 165014.
- [44] Mallat, S. G. (1998). *VA Wavelet Tour of Signal Processing*V.
- [45] Tringali, M. C. (2017). Analysis methods for gravitational wave from binary neutron star coalescences: investigation on the post-merger phase (Doctoral dissertation, University of Trento).
- [46] Necula, V., Klimenko, S., & Mitselmakher, G. (2012). Transient analysis with fast Wilson-Daubechies time-frequency transform. In *Journal of Physics: Conference Series* (Vol. 363, No. 1, p. 012032). IOP Publishing.
- [47] Drago, M. (2010). Search for transient gravitational wave signals with unknown waveform in the ligo-virgo network of interferometric detectors using a fully coherent algorithm.
- [48] Klimenko, S., Mohanty, S., Rakhmanov, M., & Mitselmakher, G. (2005). Constraint likelihood analysis for a network of gravitational wave detectors. *Physical Review D*, 72(12), 122002. ISO 690
- [49] URL: <https://wiki.ligo.org/Main/O2Injections>

- [50] URL: <https://ldas-jobs.ligo.caltech.edu/~detchar/summary/1164556817-1187733618/segments/>
- [51] URL: <https://wiki.ligo.org/DetChar/O2CleanedFrames>
- [52] URL: www.cs.dartmouth.edu/~geelong/sphere (2008)
- [53] Cabero, M., Lundgren, A., Nitz, A. H., Dent, T., Barker, D., Goetz, E., ... & Davis, D. (2019). Blip glitches in Advanced LIGO data. *Classical and Quantum Gravity*, 36(15), 155010.
- [54] URL: <https://gwburst.gitlab.io/documentation/latest/html/running.html#waveburst-tree>
- [55] Abbott, B. P. (2016). Virgo, LIGO scientific. *Phys. Rev. Lett*, 116, 061102.
- [56] URL: <https://www.csmonitor.com/Science/2017/1016/Neutron-star-collision-heralds-arrival-of-a-new-era-of-astronomy>
- [57] Cho, A. (2017). Merging Neutron Stars Generate Gravitational Waves and a Celestial Light Show. *Science*, 16.
- [58] Abbott, B. P., Bloemen, S., Canizares, P., Falcke, H., Fender, R. P., Ghosh, S., ... & Kostrzewa-Rutkowska, Z. (2017). Multi-messenger observations of a binary neutron star merger.
- [59] Tukey, J. W. (1967). An introduction to the calculation of numerical spectrum analysis. *Spectra Analysis of Time Series*, 25-46.
- [60] URL: <https://ldas-jobs.ligo.caltech.edu/~detchar/summary/1238166018-1248652818/segments/>
- [61] Piro, A. L., & Thrane, E. (2012). Gravitational waves from fallback accretion onto neutron stars. *The Astrophysical Journal*, 761(1), 63.
- [62] O'Connor, E., & Ott, C. D. (2011). Black hole formation in failing core-collapse supernovae. *The Astrophysical Journal*, 730(2), 70.

- [63] MacFadyen, A. I., Woosley, S. E., & Heger, A. (2001). Supernovae, jets, and collapsars. *The Astrophysical Journal*, 550(1), 410.
- [64] Zhang, W., Woosley, S. E., & Heger, A. (2008). Fallback and black hole production in massive stars. *The Astrophysical Journal*, 679(1), 639.
- [65] Fryer, C. L., Holz, D. E., & Hughes, S. A. (2002). Gravitational wave emission from core collapse of massive stars. *The Astrophysical Journal*, 565(1), 430.
- [66] Ott, C. D., Burrows, A., Livne, E., & Walder, R. (2004). Gravitational waves from axisymmetric, rotating stellar core collapse. *The Astrophysical Journal*, 600(2), 834. ISO 690
- [67] Kotake, K. (2013). Multiple physical elements to determine the gravitational-wave signatures of core-collapse supernovae. *Comptes Rendus Physique*, 14(4), 318-351.
- [68] Metzger, B. D., Piro, A. L., & Quataert, E. (2008). Time-dependent models of accretion discs formed from compact object mergers. *Monthly Notices of the Royal Astronomical Society*, 390(2), 781-797.
- [69] Woosley, S. E., & Heger, A. (2006). The progenitor stars of gamma-ray bursts. *The Astrophysical Journal*, 637(2), 914.
- [70] Chandrasekhar, S. (1969). Ellipsoidal figures of equilibrium.
- [71] Lai, D., Rasio, F. A., & Shapiro, S. L. (1993). Ellipsoidal figures of equilibrium-Compressible models. *The Astrophysical Journal Supplement Series*, 88, 205-252.
- [72] Piro, A. L., & Pfahl, E. (2007). Fragmentation of collapsar disks and the production of gravitational waves. *The Astrophysical Journal*, 658(2), 1173.
- [73] Fryer, C. L., Mazzali, P. A., Prochaska, J., Cappellaro, E., Panaitescu, A., Berger, E., ... & Rockefeller, G. (2007). Constraints on Type Ib/c

- Supernovae and Gamma-Ray Burst Progenitors. Publications of the Astronomical Society of the Pacific, 119(861), 1211. ISO 690
- [74] Moriya, T., Tominaga, N., Tanaka, M., Nomoto, K. I., Sauer, D. N., Mazzali, P. A., ... & Suzuki, T. (2010). Fallback supernovae: a possible origin of peculiar supernovae with extremely low explosion energies. *The Astrophysical Journal*, 719(2), 1445.
- [75] Woosley, S. E., & MacFadyen, A. I. (1999). Central engines for gamma-ray bursts. *Astronomy and Astrophysics Supplement Series*, 138(3), 499-502.
- [76] Abbott, B. P., Abbott, R., Abbott, T. D., Abraham, S., Acernese, F., Ackley, K., ... & Agathos, M. (2019). All-sky search for short gravitational-wave bursts in the second Advanced LIGO and Advanced Virgo run. *Physical Review D*, 100(2), 024017.
- [77] Abbott, B. P., Abbott, R., Abbott, T. D., Abernathy, M. R., Acernese, F., Ackley, K., ... & Adya, V. B. (2018). All-sky search for long-duration gravitational wave transients in the first Advanced LIGO observing run. *Classical and quantum gravity*, 35(6), 065009.
- [78] Collaboration, V. (2009). Advanced Virgo baseline design. Tech. Rep., VIR-0027A-09, <https://tds.ego-gw.it/ql>.
- [79] Hannam, M. (2014). Modelling gravitational waves from precessing black-hole binaries: progress, challenges and prospects. *General Relativity and Gravitation*, 46(9), 1767.
- [80] Andersson, N., Ferrari, V., Jones, D. I., Kokkotas, K. D., Krishnan, B., Read, J. S., ... & Zink, B. (2011). Gravitational waves from neutron stars: promises and challenges. *General Relativity and Gravitation*, 43(2), 409-436.
- [81] URL: <https://www.gw-openscience.org/events/GW150914>
- [82] Fishman, G. J. (1995). Gamma-ray bursts: An overview. Publications of the Astronomical Society of the Pacific, 107(718), 1145. ISO 690

- [83] Nissanke, S., Holz, D. E., Hughes, S. A., Dalal, N., & Sievers, J. L. (2010). Exploring short gamma-ray bursts as gravitational-wave standard sirens. *The Astrophysical Journal*, 725(1), 496.
- [84] Chevalier, R. A., & Li, Z. Y. (1999). Gamma-ray burst environments and progenitors. *The Astrophysical Journal Letters*, 520(1), L29.
- [85] Perna, R., Sari, R. E., & Frail, D. (2003). Jets in gamma-ray bursts: tests and predictions for the structured jet model. *The Astrophysical Journal*, 594(1), 379. ISO 690
- [86] Kouveliotou, C., Meegan, C. A., Fishman, G. J., Bhat, N. P., Briggs, M. S., Koshut, T. M., ... & Pendleton, G. N. (1993). Identification of two classes of gamma-ray bursts. *The Astrophysical Journal*, 413, L101-L104.
- [87] Virgo, F. G., & INTEGRAL, L. Scientific collaborations, BP Abbott et al., 2017 Gravitational Waves and Gamma-rays from a Binary Neutron Star Merger: GW170817 and GRB 170817A.
- [88] Metzger, B. D., Giannios, D., Thompson, T. A., Bucciantini, N., & Quataert, E. (2011). The protomagnetar model for gamma-ray bursts. *Monthly Notices of the Royal Astronomical Society*, 413(3), 2031-2056.
- [89] Abbott, B., Abbott, R., Adhikari, R., Agresti, J., Ajith, P., Allen, B., ... & Armandula, H. (2007). Searching for a stochastic background of gravitational waves with the laser interferometer gravitational-wave observatory. *The Astrophysical Journal*, 659(2), 918.
- [90] URL: <http://inspirehep.net/record/1184320/plots>
- [91] Bond, J. R. (1998). Cosmic microwave background overview. *Classical and Quantum Gravity*, 15(9), 2573.
- [92] Gossan, S. E., Sutton, P., Stuver, A., Zanolin, M., Gill, K., & Ott, C. D. (2016). Observing gravitational waves from core-collapse supernovae in the advanced detector era. *Physical Review D*, 93(4), 042002.

- [93] LIGO Scientific Collaboration. (2019). Gravitational wave astronomy with LIGO and similar detectors in the next decade. arXiv preprint arXiv:1904.03187.
- [94] Aasi, J., Abbott, B. P., Abbott, R., Abbott, T., Abernathy, M. R., Ackley, K., ... & Adya, V. (2015). Advanced ligo. *Classical and quantum gravity*, 32(7), 074001.
- [95] I.S. Kondrashov et al. "Optimizing the regimes of the Advanced LIGO gravitational wave detector for multiple source types"
- [96] Saulson, P. R. (1994). *Fundamentals of interferometric gravitational wave detectors*.
- [97] Abbott, B. P., Abbott, R., Abbott, T. D., Abraham, S., Acernese, F., Ackley, K., ... & Agathos, M. (2019). GWTC-1: a gravitational-wave transient catalog of compact binary mergers observed by LIGO and Virgo during the first and second observing runs. *Physical Review X*, 9(3), 031040.
- [98] URL: <http://inspirehep.net/record/1409068/plots>
- [99] URL: https://pages.uoregon.edu/jimbrou/BrauImNew/Chap21/FG21_08.jpg
- [100] URL: <http://inspirehep.net/record/818927/plots>
- [101] Abbott, B. P., Abbott, R., Abbott, T. D., Abraham, S., Acernese, F., Ackley, K., ... & Agathos, M. (2019). GWTC-1: a gravitational-wave transient catalog of compact binary mergers observed by LIGO and Virgo during the first and second observing runs. *Physical Review X*, 9(3), 031040. ISO 690
- [102] Nuttall, L. K. (2018). Characterizing transient noise in the LIGO detectors. *Philosophical Transactions of the Royal Society A: Mathematical, Physical and Engineering Sciences*, 376(2120), 20170286.
- [103] Abbott, B. P., Abbott, R., Abbott, T. D., Abernathy, M. R., Acernese, F., Ackley, K., ... & Adya, V. B. (2017). First search for gravitational

- waves from known pulsars with Advanced LIGO. *The Astrophysical Journal*, 839(1), 12. ISO 690
- [104] Srivastava, V., Ballmer, S., Brown, D. A., Afle, C., Burrows, A., Radice, D., & Vartanyan, D. (2019). Detection prospects of core-collapse supernovae with supernova-optimized third-generation gravitational-wave detectors. *Physical Review D*, 100(4), 043026.
- [105] Thorne, K. S., Hawking, S., & Israel, W. (1987). 300 years of gravitation.
- [106] Abbott, B. P., Abbott, R., Abbott, T. D., Abernathy, M. R., Acernese, F., Ackley, K., ... & Adya, V. B. (2016). First targeted search for gravitational-wave bursts from core-collapse supernovae in data of first-generation laser interferometer detectors. *Physical Review D*, 94(10), 102001.
- [107] URL: <https://apod.nasa.gov/htmltest/jbonnell/www/grbhist.html>
- [108] Mandhai, S., Tanvir, N., Lamb, G., Levan, A., & Tsang, D. (2018). The rate of short-duration gamma-ray bursts in the local universe. *Galaxies*, 6(4), 130
- [109] Stratta, G., Dainotti, M. G., Dall'Osso, S., Hernandez, X., & De Cesare, G. (2018). On the magnetar origin of the GRBs presenting X-ray afterglow plateaus. *The Astrophysical Journal*, 869(2), 155.
- [110] Lim, Y., Holt, J. W., & Stahulak, R. J. (2019). Predicting the moment of inertia of pulsar J0737-3039A from Bayesian modeling of the nuclear equation of state. *Physical Review C*, 100(3), 035802.
- [111] URL: <https://link.springer.com/content/pdf/10.1140/epjc/s10052-017-4925-3.pdf>
- [112] URL: <https://core.ac.uk/download/pdf/82501031.pdf>
- [113] Christensen, N. (2018). Stochastic gravitational wave backgrounds. *Reports on Progress in Physics*, 82(1), 016903.

- [114] URL: <https://www.ligo.caltech.edu/news>
- [115] URL: <https://www.sciencedirect.com/science/article/pii/S0927650510000253?via%3Dihub>
- [116] Abbott, B. P., Abbott, R., Abbott, T. D., Abraham, S., Acernese, F., Ackley, K., ... & Agathos, M. (2020). GW190425: Observation of a compact binary coalescence with total mass $\sim 3.4 M_{\odot}$. *The Astrophysical Journal Letters*, 892(1), L3.
- [117] LIGO Scientific Collaboration, & Virgo Collaboration. (2020). GW190412: Observation of a Binary-Black-Hole Coalescence with Asymmetric Masses. arXiv preprint arXiv:2004.08342.
- [118] Tai, K. S., McWilliams, S. T., & Pretorius, F. (2014). Detecting gravitational waves from highly eccentric compact binaries. *Physical Review D*, 90(10), 103001.
- [119] Bucciantini, N. (2011). Magnetars and gamma ray bursts. *Proceedings of the International Astronomical Union*, 7(S279), 289-296.
- [120] <https://core.ac.uk/download/pdf/82501031.pdf>
- [121] Anderson, W. G., Brady, P. R., Creighton, J. D., & Flanagan, E. E. (2001). Excess power statistic for detection of burst sources of gravitational radiation. *Physical Review D*, 63(4), 042003. ISO 690
- [122] Was, M. (2011). Searching for gravitational waves associated with gamma-ray bursts int 2009-2010 ligo-virgo data (No. FRNC-TH--8260). Universite Paris XI.
- [123] Gill, K., Massera, E. Gravitational Waves from Fallback Accretion and Black Hole Formation in Long Gamma-Ray Bursts (2019)
- [124] Gill, K. and S. E. Gossan Gravitational Waves from Fallback Accretion and Black Hole Formation in Long GRBs
- [125] Pan, K. C., Liebendörfer, M., Couch, S. M., & Thielemann, F. K. (2018). Equation of State Dependent Dynamics and Multi-messenger

Signals from Stellar-mass Black Hole Formation. *The Astrophysical Journal*, 857(1), 13.

- [126] Aasi, J., Abadie, J., Abbott, B. P., Abbott, R., Abbott, T., Abernathy, M. R., ... & Adhikari, R. X. (2013). Search for long-lived gravitational-wave transients coincident with long gamma-ray bursts. *Physical Review D*, 88(12), 122004.

Acknowledgements

Here we are, in the middle of a pandemic, I'm finally completing my Ph.D.

It would be reductive to say that it was the most arduous path I have ever faced. My colleague Tega said it best: "It's up to you. You can swim or sink ". I would be lying by saying that I only swam, because I risked sinking many times. But I did it, and I feel that all challenges made me a better and stronger person.

First of all, I thank Max, Marco and Claudia. I don't really know what I would have done without you all. You have been a mentor and above all you have become special friends.

I am thankful to Ed, who put my wellbeing first, by let me choosing what was best for me.

Special thanks also go to all Italian colleagues who have become an irreplaceable group of friends. Above all, thanks to Marica for supporting me.

Thanks to all those who with small and silent gestures believed in me, helping me to reach this goal!